Thermoacoustic Instabilities in Heating Appliances with Premixed Burner and Heat Exchanger
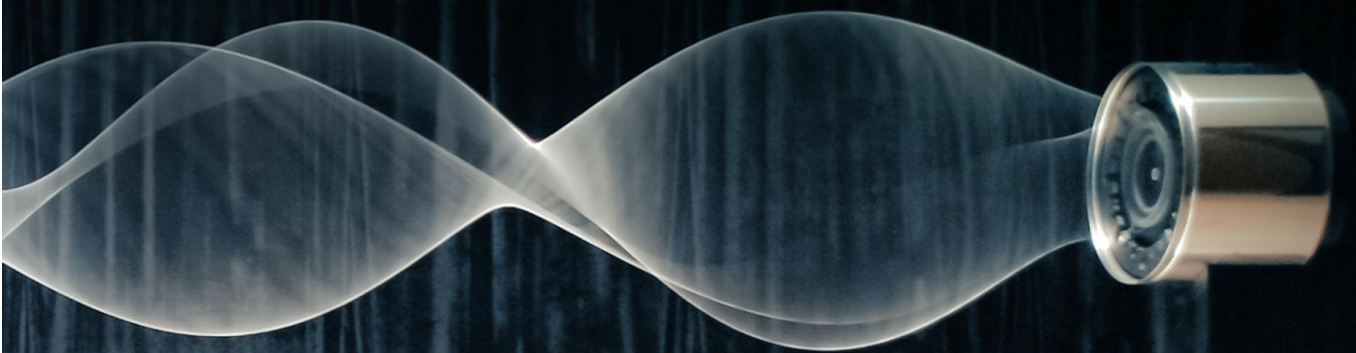
Naseh Hosseini

Thermoacoustic Instabilities in Heating Appliances with Premixed Burner and Heat Exchanger

To the love of my life…

Thermoacoustic Instabilities
in Heating Appliances
with Premixed Burner and Heat Exchanger

PROEFSCHRIFT

ter verkrijging van de graad van doctor aan de Technische Universiteit Eindhoven,
op gezag van de rector magnificus prof.dr.ir. F.P.T. Baaijens,
voor een commissie aangewezen door het College voor Promoties, in het openbaar
te verdedigen op woensdag 9 januari 2019 om 11:00 uur

door

Naseh Hosseini

geboren te Mashhad, Iran

Dit proefschrift is goedgekeurd door de promotoren en de samenstelling van de promotiecommissie is als volgt:

voorzitter:	prof.dr.ir. A.A. van Steenhoven
1e promotor:	prof.dr. L.P.H. de Goey
2e promotor:	prof.dr.ir. I. Lopez Arteaga
copromotor:	dr. V.N. Kornilov
leden:	prof. W. Polifke PhD (TU München)
	dr.ir. J.B.W. Kok (UT)
	prof.dr.ir. G.J.F. van Heijst
adviseur:	dr.ir. O.J. Teerling (Bekaert Combustion Technology B.V.)

Contents

Contents

Figures

Figures

Tables

CHAPTER 1

Introduction

1.1 Motivation

Most combustion systems are designed to operate in stable regimes. However, oscillations sometimes occur in practical combustion systems such as gas turbines, furnaces and heating systems. One major group of combustion instabilities are thermoacoustic (TA) instabilities, which are excited by a feedback loop between an oscillatory combustion process and, in general, one or more of the natural acoustic modes of the system. They occur more frequently in lean premixed combustion, which have been favored in the past decades in order to reduce nitrogen oxides (NO_x) emissions. Thermoacoustic instabilities may occur in almost any combustion system in which acoustic waves (partially) reflect and cause pressure fluctuations in the order of audible noise up to mean operating pressure of the system. This may lead to severe consequences such as flame quenching, blowoff and/or flashback, but may also result in severe physical damage to the installation [1]. On the one hand, not all branches of industry that are dealing with combustion recognize thermoacoustics as a design problem. They usually fine-tune the stability of the system in the latest stages of development also because these instabilities are very difficult to predict. On the other hand, studying thermoacoustics requires combining all usual physics involved in reacting flows (fluid mechanics, heat transfer and chemical kinetics) with acoustics, hydrodynamic stability and control theory. The strong couplings that exist between these physical phenomena are not

trivial to describe, that has made thermoacoustic instabilities the hidden and feared problem of many combustion programs, starting with solid- and liquid-fuel rocket engines in the 50s and continuing more recently in gas turbines, industrial furnaces or even domestic heating systems [1]. Thermoacoustic instabilities in domestic heating systems may not be as intense as in e.g., gas turbines, but they are specifically important since they considerably limit the operating range of the system. On the other hand, manufacturers of domestic heating appliances are dealing with strict residential noise regulations and cannot afford even low noise levels. This is why the heating industry has been recently very engaged in the thermoacoustic research in order to develop design rules for engineering stable and silent heating systems.

A typical configuration of a residential heating appliance including a premixed perforated cylindrical burner and two types of heat exchanger (helical steel tubes and pinned aluminum sections) are illustrated in Figure 1.1. A blower feeds air into the system and fuel mixes with the flow through a venturi. The mixture then burns on the surface of the burner, forming laminar or near turbulent surface-stabilized flames. The hot combustion products pass through the heat exchanger and cool down before going to the exhaust. The exhaust temperature is defined as a design parameter for the efficiency of the heat exchanger and it may be limited to the same order of magnitude as the unburned mixture temperature due to environmental regulations.

| (a) | (b) | (c) |
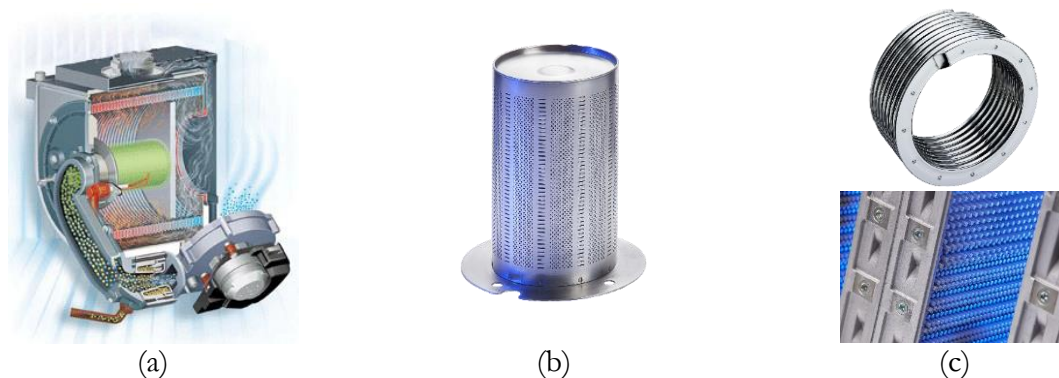
Figure 1.1: (a): A typical configuration of a heating appliance (image courtesy of Houseneeds Inc.); (b): a premixed perforated cylindrical burner (image courtesy of Bekaert Combustion Technology B.V.); (c): a helical steel-tube heat exchanger (image courtesy of Viessmann Group) and a pinned aluminum heat exchanger (image courtesy of Bekaert Combustion Technology B.V.).

For studying (low-frequency) acoustics in such systems, a simple schematic of the heating appliance is usually used to show the sequence of elements. Such a schematic is illustrated in Figure 1.2. The typical values for the unburned (T_u), burned (T_b) and exhaust (T_e) temperatures are given.
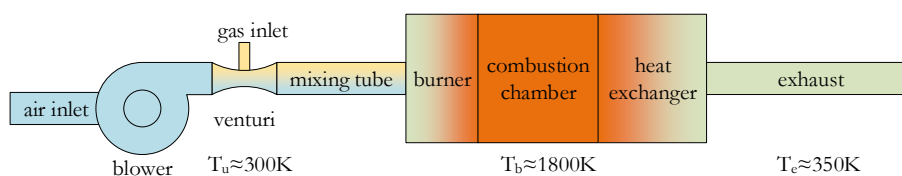
Figure 1.2: A simple schematic of a heating appliance showing the sequence of elements and typical values of the unburned (T_u), burned (T_b) and exhaust (T_e) temperatures.

The first step in thermoacoustic research is to identify the active and passive thermoacoustic elements in the system. An active element (such as the burner/flame) is one that can be used to

provide amplification of a signal or can be made to oscillate. However, passive elements (such as ducts, vessels and terminations) do not exhibit amplification or oscillation and may only cause reflection, attenuation and/or phase shift in propagation of acoustic waves [2]. As a common practice, the burner is usually treated as the only active element and the other components are assumed to be passive [3, 4]. An illustration of this practice for a typical heating appliance is shown in Figure 1.3. Here, the system contains a premixed perforated burner and the focus is on the processes that affect the acoustic response of the burner. The system acoustics and properties of all passive elements are collected in the element labeled "acoustics". The major processes affecting the burner are in the fuel and air supplies. The gas provided by the network may have varying properties (especially with the recent developments on gas-adaptive systems, the burners are expected to operate on various gaseous fuels and compositions). The airflow is often not completely laminar and may include fluctuations, vortices or turbulences caused by e.g. the blower blades (the so-called blade passing frequency). Such fluctuations in the gas or air stream create perturbations of mixture velocity and/or composition, and may even produce extra vortices and turbulence. All these fluctuations may change the flame shape and anchoring conditions that in turn alter the heat release rate in premixed combustion [1]. The fluctuating heat release is known to act as an acoustic source and feed energy back into the system acoustics. These fluctuations induce acoustic waves travelling upstream and downstream of the burner, hence creating additional velocity fluctuations, vortices and, if large enough, turbulence, and close the feedback loop in the system. If the gain in this feedback loop is larger than the acoustic losses in the system, instabilities arise.
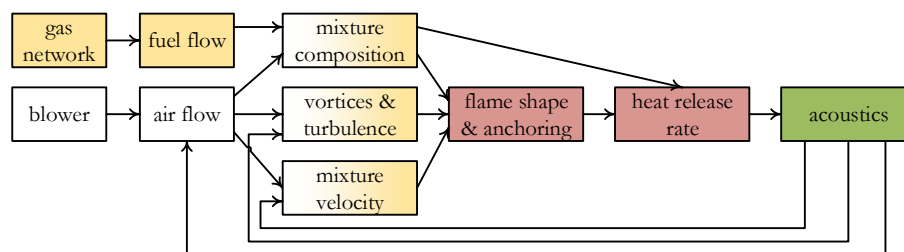
Figure 1.3: The processes affecting the thermoacoustics in heating appliances with the premixed burner as the only active element.

Recently, it has been introduced that schematics such as presented in Figure 1.3 are incomplete, due to considering the heat exchanger as a passive thermoacoustic element [5–8]. The heat exchanger is designed to absorb most of the heat and create a reverse temperature jump of the same order of magnitude as the burner. It is well-known that an acoustically forced flow can create a fluctuating heat flux on the surface of the bodies in the flow [9, 10]. Therefore, the heat exchanger itself is an additional active acoustic element next to the burner in the acoustic network. In this respect, a more complete schematic of the system is presented in Figure 1.4. Various processes may create fluctuating heat flux of the heat exchanger. The acoustic fluctuations in the burned mixture alter the bulk flow velocity near the heat exchanger. Possible turbulence and vortices induced by acoustic or hydrodynamic fluctuations may also create a fluctuating velocity field around the heat exchanger. This fluctuating velocity changes the thermal and hydrodynamic boundary layers and thus creates a fluctuating heat flux on the heat exchanger surface.
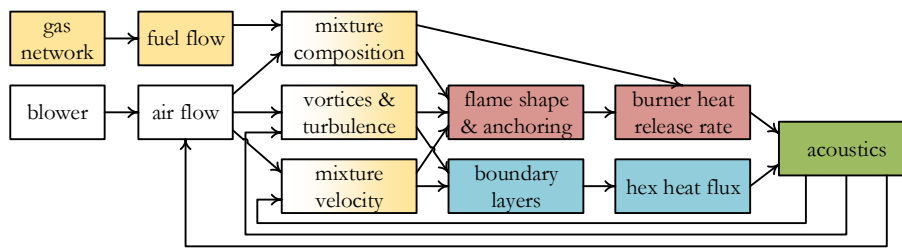
Figure 1.4: The processes affecting the thermoacoustics in heating appliances with both the premixed burner and heat exchanger as active elements.

The simplest way to analyze such systems is to deal with the active acoustic sources of the burner and heat exchanger as independent and serial. On the other hand, the practical need to reduce the built volume of heating appliances and minimize nitrogen oxides, leads to the desire to locate the heat exchanger very close to the burner. The smaller this distance is, the more questionable it becomes to consider the burner and the heat exchanger as two acoustically independent elements. It is known that in the limit case of impinging flames, the intense interaction of flames with the heat exchanger leads to changes of the acoustic properties of the burner. Particularly, it was observed that impingement may change the noise produced by the flame [11–13]. Similarly, the proximity of a heat source (burner) to the heat exchanger surface can affect the periodic heat transfer between the surface and hot gases [14–16]. Thus, one may foresee that the fluctuations induced by the flame dynamics may alter the acoustic properties of the heat exchanger. Therefore, the thermoacoustic properties of the combination of the burner and heat exchanger may differ drastically from when considered independent. This motivates studying the coupled thermoacoustic effects of the burner and heat exchanger in order to obtain a correct description of the thermoacoustic behavior of the heating appliance.

1.2 Objectives

The ultimate goal in the presented work is to elucidate the thermoacoustic phenomena in heating appliances containing premixed burners and heat exchangers. The approach is to analyze the system by investigating the separate and coupled thermoacoustic behavior of its constituting elements. Particularly, it is important to answer the following questions:

- What are the separate thermoacoustic responses of practical laminar premixed burners and heat exchangers in heating appliances?
- How do the burner and heat exchanger come together to define the TA characteristics of a heating appliance?
- What kind of interactions are envisioned between the burner and heat exchanger that may affect the TA behavior of the complete system?
- What are the physical phenomena and governing parameters responsible for these interactions?
- Is it possible to decouple the effects of the burner and heat exchanger? If so, how can one decouple these effects and use them to design more stable heating appliances?

1.3 Research objects

To solve the formulated problem and questions, various configurations are studied, which consist of Bunsen-type premixed flames anchored on perforations in a burner deck, and interacting with heat exchangers placed downstream of the burner. First, simplified academic configurations are studied, such as a 2D wedge flame and a circular-tube heat exchanger as illustrated in Figure 1.5. Such configurations are composed of relatively simple elements, which have been studied in the past on theoretical, experimental and numerical levels [17–20]. This enables to describe the physics of the problem in detail. Furthermore, these configurations are representative for the design of a majority of heating appliances.
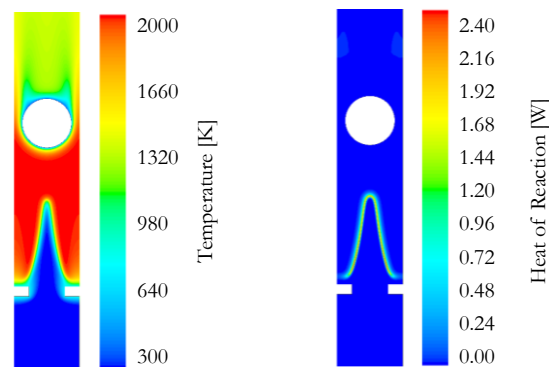
Figure 1.5: The contours of temperature (left) and heat of reaction (right) for a 2D wedge flame and a circular-tube heat exchanger.

Experiments and CFD simulations are performed in order to measure the response of the burner to acoustic waves in various operating conditions. For the heat exchanger, there are no convenient and measurable direct indicators (like light emissions by chemical radicals for flame heat release) for the oscillating rate of heat transfer from the hot gases to the heat exchanger. One may propose to measure the velocity instead of heat flux and use indirect approaches to reconstruct the acoustic response of the heat exchanger. However, this requires velocity measurement equipment that works accurately when placed in post-combustion temperature upstream of the heat exchanger, which can be very challenging. These facts motivate the use of the CFD-based analysis to evaluate the response of simplified and realistic heat exchangers. The burner and heat exchanger are then combined and the response of the total system to acoustic fluctuations is evaluated. After evaluating the separate and coupled responses of the elements, the stability of the total system is analyzed using an acoustic network model in simplified cases, and a Helmholtz solver for the cases with more complicated configurations.

1.4 Contributions

The major contributions of this thesis can be summarized as follows,

- Thermoacoustic instabilities in heating appliances are investigated using a method of decomposition/recomposition.

- The system is decomposed to its active and passive thermoacoustic elements and details are revealed about the possible decomposition methods.
- Analyzing the burner transfer function exposes novel details of flame area contribution that are captured in simulations and confirmed by measurements.
- The decomposed elements are recomposed to construct the total system behavior and various interaction scenarios are investigated (the significant effects of the active heat exchanger on the thermoacoustic properties of the system, which has mainly been ignored in the past, are found and emphasized).
- Broad parametric studies lead to a holistic view of the thermoacoustic behavior in heating appliances, which can be used as guidelines by manufactures to produce more stable heating systems.

1.5 Thesis structure

In the following chapter (Chapter 2), the theory and physics of thermoacoustic instabilities in heating appliances are discussed, where the governing phenomena and instability scenarios are introduced along with related literature. Chapter 3 is dedicated to describing the experimental and numerical methods and tools that are used in the present work. In Chapter 4, the tools described in Chapter 3 are used to study the separate thermoacoustic behavior of simplified and realistic burners and heat exchangers. In Chapter 5, the combinations of burner and heat exchanger are analyzed to obtain the thermoacoustic behavior of simplified heating appliances. In Chapter 6, the data obtained in Chapters 4 and 5 are used for the stability analysis of simplified and more realistic heating appliances. The findings are concluded in Chapter 7 and recommendations are formulated for future researchers to contribute to the findings.

Theory and Physics of Thermoacoustic Instabilities in Heating Appliances

In this chapter, the most dominant physics associated to combustion instabilities in heating appliances are briefly introduced. Then the basic theory of thermoacoustic instabilities is discussed.

2.1 Instability scenarios in heating appliances

Various types of combustion instabilities have been discussed in detail in the literature [1, 21, 22]. However, not all types are applicable to heating appliances as the focus of this work. The important mechanisms that may be the root cause of combustion instabilities in heating appliances are categorized as, fluid dynamic instabilities, thermoacoustic instabilities and, as a specific case, intrinsic thermoacoustic instabilities.

2.1.1 Fluid dynamic instabilities

Fluid dynamic instabilities are related to certain flow patterns that occur in such a way that results in a periodic heat release due to combustion. In burners with perforated-plate-stabilized flames, for example, sufficiently large standoff distance or sensitive flame anchoring may give rise to fluid dynamic instabilities [23]. Figure 2.1a visualizes the vortices in the anchoring region of a

premixed methane-air flame stabilized on a flat burner deck with rectangular (slit) perforations [24]. These vortices are a result of large standoff distance between the flame and flame holder. Figure 2.1b presents a sequence of images acquired with a high-speed camera from a similar flat burner deck with rectangular (slit) perforations. From top left to bottom right, it shows periodic motion of a flame that is formed due to the merging of two adjacent flames. This situation is caused by weak flame anchoring that is affected by vortex shedding downstream of the slit perforations (a proper stabilization would have resulted in two separate and stable flames).

(a)   (b)   (c)
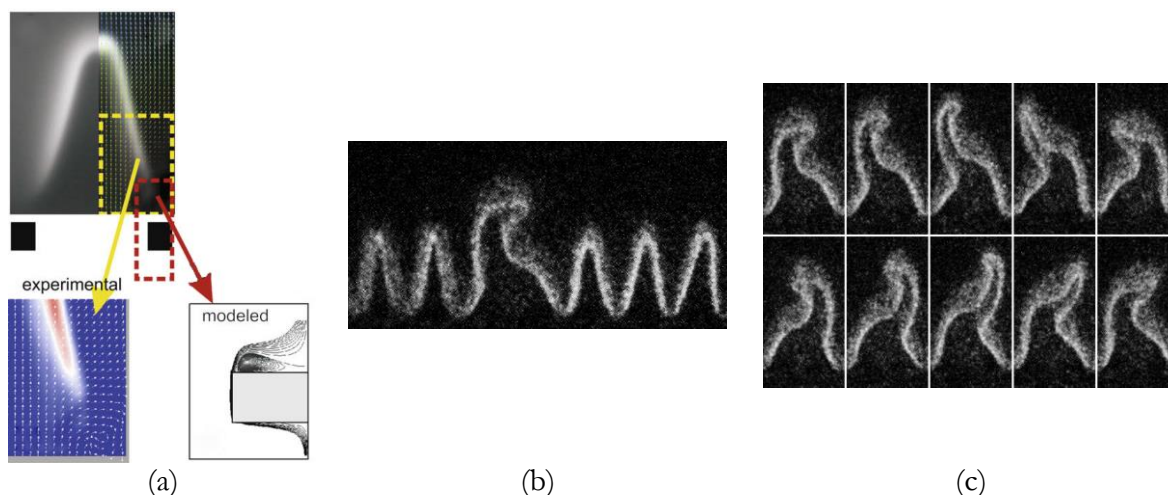
Figure 2.1: (a): Premixed methane-air flames stabilized on a flat burner deck with rectangular perforations (slits) with the vortices in the anchoring region [24]*; (b): a snapshot of slit flames stabilized downstream of a burner deck, showing two merged flames due to weak anchoring and vortex shedding downstream of the slits; (c): a sequence of images (from top left to bottom right) of the same burner deck showing the periodic movement of the merged flames (image courtesy of Bekaert Combustion Technology B.V.).*

On the other hand, the heat exchanger in a heating appliance acts as a bluff body and may induce fluid dynamic instabilities, such as von Kármán Vortex Street. Since in this work the heat exchanger is considered a possible active thermoacoustic element, it is important to consider these effects. Details related to these processes are discussed in Chapter 4.

2.1.2 Thermoacoustic instabilities

Thermoacoustic instability is one of the most common types of combustion instabilities in heating appliances and is characterized by the propagation of acoustic waves in the system. The oscillations are usually harmonic and possess a frequency, which is determined by the system geometry and the velocity of sound in the medium contained in the system. Thermoacoustic instability occurs when the amount of energy fed into the acoustic filed by unsteady combustion or heat transfer, exceeds the amount extracted by absorption and radiation losses.

The feeding of energy is performed by active thermoacoustic elements and a very important factor is the size and location of these elements. Regarding size, they can be generally categorized into compact and non-compact, in comparison to the acoustic wavelength in the system. Examples of compact elements are burners with concentrated flames like premixed Bunsen-type flames, and heat exchangers with small tubes (see Figure 1.1c top). The dimensions of large swirl flames or

distributed heat exchangers (see Figure 1.1c bottom) may be comparable to the acoustic wavelength in the system, making them non-compact elements.

Thermoacoustic instabilities may occur in various modes, such as longitudinal (axial), radial, tangential, annular, or any combination of them, such as oblique modes. The geometry of the system and configuration of the active elements are the main parameters that dictate the occurring mode. The annular modes may occur in gas turbines with multiple burners placed around an annulus in the combustion chamber. The tangential modes may occur in rocket engines with cylindrical geometry. The radial modes require maximum heat release near the chamber axis and are rarely observed.

The longitudinal modes, however, are the most common in heating systems and occur most easily when the energy feed takes place in a zone where the pressure and velocity variations are large. These modes can be very intense and according to Rayleigh's theory (see section 12.2 *"Rayleigh criterion"*), maximum amplification occurs when the pressure fluctuations are in-phase with the periodic energy feed. In heating appliances, these modes usually correspond to a pipe open at both ends, i.e. the Rijke tube [25].

2.1.2.1   *Intrinsic thermoacoustic (ITA) instabilities*

In traditional thermoacoustics, it is understood that for a system to be thermoacoustically unstable, a coupling should exist between the active elements and the acoustic reflections from the rest of the system. However, it was established recently that a combustor can be unstable even in the absence of any acoustical reflections upstream or downstream of the burner [1]. This type of instability is thought to originate from an inherent coupling within the active element itself and are called Intrinsic Thermoacoustic (ITA) instabilities. The system modes associated to this inherent coupling are called "*ITA modes*". Any resonance mode of the system is either an acoustic mode or an ITA mode [26, 27].

ITA instabilities may be observed in many types of systems prone to thermoacoustic instabilities, such as rocket engines, gas turbines and heating appliances. They are specifically important since they usually manifest as instabilities that do not respond adequately to the changes in upstream and/or downstream acoustic properties. This means that the conventional approach of increasing acoustic damping at the system boundaries would prove useless in mitigating this type of instability. Moreover, it has been shown that in certain conditions, increasing acoustic damping would further destabilize the system [26, 27].

These briefly introduced mechanisms are further investigated in Chapters 4, 5 and 6.

2.2   Rayleigh criterion

The first observation of thermoacoustic instabilities dates back to 1777 when Higgins [28] first observed the "singing flame", which was due the excitation of a characteristic sound wave by placing a hydrogen diffusion flame in a tube with open ends. Rijke investigated this phenomenon in detail by placing a wire mesh in a similar tube. He observed that the oscillations are strongest

when the wire mesh is placed at one fourth of the tube length [25]. The work of Soundhauss in 1850 is known to be the first in forming the modern thermoacoustics. He investigated this phenomenon in glass blowing process and observed that sound frequency and intensity depend on the length and volume of the bulb. However, Lord Rayleigh later gave a qualitative explanation of Sondhauss's observations. He stated that producing any type of thermoacoustic oscillations needs to meet a criterion, later named after himself "*The Rayleigh Criterion*" [29]:

> *"If heat be periodically communicated to, and abstracted from, a mass of air vibrating (for example) in a cylinder bounded by a piston, the effect produced will depend upon the phase of the vibration at which the transfer takes place. If heat be given to the air at the moment of greatest condensation, or taken from it at the moment of greatest rarefaction, the vibration is encouraged. On the other hand, if heat be given at the moment of greatest expansion, or abstracted at the moment of greatest condensation, the vibration is discouraged."*

This criterion shows that thermoacoustics is related to the interplay of density variations and heat generation. The first mathematical formulation of the Rayleigh criterion was derived by Putnam and Dennis [30] in 1954 as

$$R = \int_0^T p'(t)q'(t)dt > \int_0^T \Phi(t)dt, \tag{2-1}$$

where R, T and Φ denote the Rayleigh index, period of oscillation and wave energy dissipation, respectively, and the prime indicates fluctuating values of the pressure (p) and heat release rate (q). A positive Rayleigh index indicates an energy transfer from the heat release/absorption to the pressure oscillations (amplification of the pressure oscillations) and a negative index corresponds to a damping of the pressure oscillation (indicating an inverse energy flow). However, the coupling between the heat source/sink and the pressure wave is essential for the formation of thermoacoustic instabilities. Therefore, the starting point in understanding thermoacoustics in heating appliances is to investigate this coupling.

2.3 Thermoacoustic theory

The basics of thermoacoustic theory can be obtained by linearizing the conservation equations in presence of acoustic fluctuations, and then realizing models for generation and propagation of the disturbances.

2.3.1 Conservation equations

The linearized one dimensional conservation equations of mass and momentum in the simple case of a compressible inviscid fluid with no external forces are given as [31]

$$\frac{\partial \rho'}{\partial t} + \overline{\rho}\nabla \cdot u' = 0 \text{ and} \tag{2-2}$$

$$\bar{\rho}\frac{\partial u'}{\partial t} + \nabla p' = 0, \tag{2-3}$$

where ρ denotes the density and the overbar shows the steady means.

The variations in density are due to changes in both pressure and entropy. In most heating appliances, it is reasonable to assume that combustion occurs for perfect gases with no molecular weight change, low Mach number and no gradient of mean pressure (because the flow velocity is relatively small and combustion occurs at constant pressure). Therefore, following the procedure explained by Dowling [31] and assuming no mean velocity and no mean heat input, we can obtain the inhomogeneous wave equation

$$\frac{1}{\bar{c}^2}\frac{\partial^2 p'}{\partial t^2} - \bar{\rho}\nabla\cdot\left(\frac{1}{\bar{\rho}}\nabla p'\right) = \frac{\gamma-1}{\bar{c}^2}\frac{\partial Q'}{\partial t}, \tag{2-4}$$

where c is the speed of sound, Q' is the oscillating heat release/absorption rate per unit volume, and γ is the ratio of specific heats. Here, Q' is considered to be an acoustic source affecting the acoustic wave pressure. If there is no fluctuating heat source/sink, $Q'=0$ and this equation reduces to the homogeneous wave equation. If the oscillating heat release is in phase (or the oscillating heat sink is out of phase) with the acoustic field, it enhances the acoustic energy in the system and the amplitude of the oscillations will increase. If the amplitudes grow sufficiently large, the responses of the active elements and acoustic losses become nonlinear and lead to a saturation into limit cycle [32].

Using Equation (2-4) with proper initial and boundary conditions yields the complete solution to describe the system. However, in thermoacoustic instabilities, the acoustic and heat release/absorption fluctuations are coupled. Therefore, Q' needs to be defined according to the type of the feedback loop encountered. When this coupling is described, it acts as a damping or amplification term in the equation.

2.3.2 Helmholtz equation

The inhomogeneous Helmholtz equation can be obtained by rewriting Equation (2-4) in the frequency domain using $p' = \hat{p}e^{-i\omega t}$ and $Q' = \hat{Q}e^{-i\omega t}$.

$$-\frac{\omega^2}{\bar{c}^2}\hat{p} - \bar{\rho}\nabla\cdot\left(\frac{1}{\bar{\rho}}\nabla\hat{p}\right) = i\omega\frac{\gamma-1}{\bar{c}^2}\hat{Q}, \tag{2-5}$$

where ω denotes the angular frequency. Now it is possible to couple the frequency-dependent source term to the acoustic modes.

There are various ways that a closure can be introduced between the acoustic field and the heat release/absorption oscillations by active elements. For the case of dependent sources, like burner and/or heat exchanger, heat fluctuation is a function of acoustic parameters. One of the most common ways to analyze this dependence is via a transfer function (TF) in the form of

$$\mathbb{F} = \frac{\hat{Q}/\overline{Q}}{\hat{\varepsilon}/\overline{\varepsilon}}, \tag{2-6}$$

where ε denotes the acoustic parameter. In heating appliances with lean premixed burners, the heat release is mainly affected by velocity and/or equivalence ratio fluctuations [1]. Since the focus of this work is on the fully premixed systems, only the velocity-sensitive transfer function is considered. Therefore,

$$\mathbb{F} = \frac{\hat{Q}/\overline{Q}}{\hat{u}/\overline{u}} \tag{2-7}$$

and

$$\hat{Q} = \mathbb{F}\frac{\overline{Q}}{\overline{u}}\hat{u}, \tag{2-8}$$

that changes Equation (2-5) to

$$\frac{\omega^2}{\overline{c}^2}\hat{p} + \overline{\rho}\nabla \cdot \left(\frac{1}{\overline{\rho}}\nabla\hat{p}\right) = -i\omega\frac{\gamma-1}{\overline{c}^2}\frac{\overline{Q}}{\overline{u}}\mathbb{F}\hat{u}. \tag{2-9}$$

Assuming that the linearized system is also time-invariant (LTI) [31], this equation can be solved using various approaches, of which two major ones are introduced in the next section and further discussed in the following related chapters.

2.3.3   Solutions strategies

The two major strategies to solve the system are the lumped and distributed approaches. In the lumped approach, the system is divided into sub-systems and the defined behavior of these sub-systems are coupled to each other. In the distributed approach, the equations are solved using a discretization scheme, such as finite difference or finite element. The basic theory of the lumped approach is discussed in the following and the distributed approach is further elaborated in Chapter 3, section 3.4.2.2 *"FEM acoustic simulations using Comsol"*.

2.3.3.1   Lumped approach or network models

In such models, the complex thermoacoustic system is conceived as a network of segregated elements, of which the responses are characterized by the amplitudes of the ingoing and outgoing waves. This implies that the acoustic behavior of a single element does not depend on the presence of other elements in the acoustic network. These models are also known as "*network models*" and are commonly used in the literature, due to their versatility and simple calculations in defining and describing complex systems [4, 33, 34]. The elements in a network model are evaluated based on their complexity and involved physical phenomena. The result is then a network of interconnected acoustic elements that represents the acoustics of the complete system. The elements can be simulated separately and coupled in time domain [7, 8, 35] (this is the approach in Chapter 5), or in frequency domain [4, 6, 36] (this is the approach in Chapter 6).

In the case of 1D plane wave propagation, it is possible to solve the obtained low-order model analytically. Here, the elements are modelled either as algebraic relations due to acoustically

compact discontinuities in area and/or medium properties, or (linear) Green's functions of ducts [37, 38].

In general, any network element can be expressed in upstream and downstream parameters. The choice of the parameters usually depends on the type of study performed. The most common parameters are either the pair of acoustic pressure and velocity (p and u), or the Riemann invariants (f and g) [39, 40]. The relation between these parameters are expressed as

$$\frac{p'}{\rho c} = f + g \text{ and } u' = f - g. \tag{2-10}$$

Figure 2.2 illustrates an arbitrary LTI element and shows the upstream and downstream acoustic fluctuations.
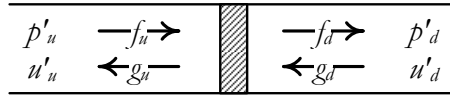
Figure 2.2: The acoustic fluctuations upstream and downstream of an arbitrary LTI element.

Depending on the choice of the input and output waves, various matrices can be derived that describe the transformation of waves through the element. The three most common matrices are illustrated in Figure 2.3, where the inputs and outputs are arranged on the left- and right-hand sides of the element, respectively. The acoustic transfer matrix (M) is illustrated in Figure 2.3a and relates the velocity and pressure fluctuations upstream and downstream of the element. A similar transfer matrix between the Riemann invariants (T) is presented in Figure 2.3b. Using the incoming waves as input and the outgoing waves as output of the LTI system, respects causality and leads to an informative form of the matrix called the scattering matrix (S) and is shown in Figure 2.3c. The diagonal elements of the scattering matrix S_{11} and S_{22} represent the reflection coefficients as seen from the upstream and downstream sides of the element when g_d or f_u are zero, respectively. Moreover, S_{12} and S_{21} are the transmission coefficients to the up- and downstream sides when f_u or g_d are zero, respectively [41]. Therefore, the scattering matrix respects causality and provides additional physical insight into what should be considered as input and output for the element.

$$\begin{bmatrix} p_d \\ u_d \end{bmatrix} = \begin{bmatrix} M_{11} & M_{12} \\ M_{21} & M_{22} \end{bmatrix} \begin{bmatrix} p_u \\ u_u \end{bmatrix} \qquad \begin{bmatrix} f_d \\ g_d \end{bmatrix} = \begin{bmatrix} T_{11} & T_{12} \\ T_{21} & T_{22} \end{bmatrix} \begin{bmatrix} f_u \\ g_u \end{bmatrix} \qquad \begin{bmatrix} f_d \\ g_u \end{bmatrix} = \begin{bmatrix} S_{11} & S_{12} \\ S_{21} & S_{22} \end{bmatrix} \begin{bmatrix} f_u \\ g_d \end{bmatrix}$$

(a)   (b)   (c)
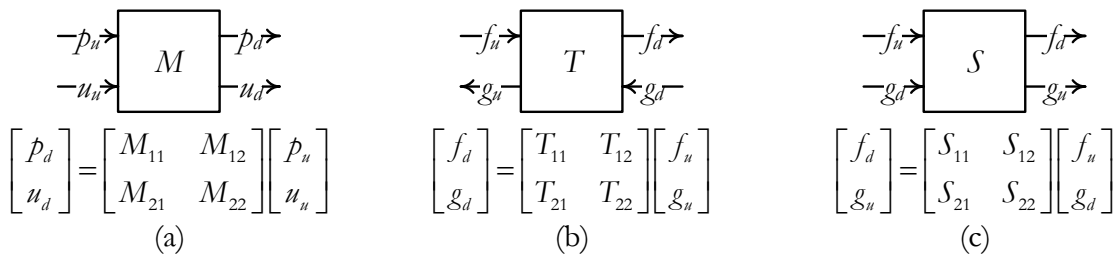
Figure 2.3: The three most common matrices for describing the relation between acoustic quantities upstream and downstream of an element; p-u transfer matrix (a), f-g transfer matrix (b) and scattering matrix (c).

In order to describe the acoustic system completely, the conditions at the boundaries need to be defined. If the pressure and velocity are considered, the upstream and downstream boundary conditions will be defined in the form of acoustic impedance [38]

$$Z_u = \frac{p'_u}{u'_u} \text{ and } Z_d = \frac{p'_d}{u'_d}, \tag{2-11}$$

with units $[Ns/m^3]$. Impedance is a complex number and its real and imaginary parts are referred to as resistive and reactive components, respectively.

If the network model is built using the Riemann invariants f and g, then the reflection coefficient (R) is used, which is defined as the ratio of the outgoing to incoming waves. The portion of the incoming wave that is transmitted forms the transmission coefficient (T). Therefore, we have

$$R_u = \frac{f}{g}, \; T_u = \frac{g_{tr}}{g}, \; R_d = \frac{g}{f} \text{ and } T_d = \frac{f_{tr}}{f}, \tag{2-12}$$

where f_{tr} and g_{tr} are the portions of the waves that are transmitted through the boundaries. The impedances and reflection coefficients can then be related as

$$\frac{Z_u}{\rho c} = -\frac{1+R_u}{1-R_u}, \; R_u = \frac{Z_u + \rho c}{Z_u - \rho c}, \; \frac{Z_d}{\rho c} = \frac{1+R_d}{1-R_d} \text{ and } R_d = \frac{Z_d - \rho c}{Z_d + \rho c}. \tag{2-13}$$

A network model representation of a typical heating appliance (as shown in Figure 1.2) is presented in Figure 2.4. The active elements (burner and heat exchanger) are indicated with gray shade.

open end (acoustic reflections)	inlet tubing (ducts and area changes)	burner (active source)	combustion chamber (duct)	heat exchanger (active sink)	exhaust tubing (ducts and area changes)	open end (acoustic reflections)
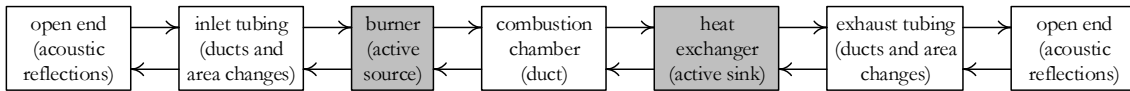
Figure 2.4: A network model representation of a typical heating appliance (as shown in Figure 1.2) showing the burner and heat exchanger as active elements and the rest as passive.

The details of how these methods are used in this work are presented in Chapter 3. The network model approach is applied in Chapters 4 and 5. The results in Chapter 6 include the solution of the distributed approach using the finite element commercial package, Comsol [42].

CHAPTER 3

The Experimental and Numerical Methods and Tools

In this chapter, details of the methods and tools used in this work are presented. This information contains the configuration of the measurement setup for measuring burner transfer function, and the numerical setups for calculating the burner and heat exchanger transfer functions, as well as system stability analysis.

3.1 Experimental apparatus

The burner is the most complex element in studying thermoacoustics of heating appliances. Therefore, detailed measurements were performed in order to evaluate the TF of various burner decks with circular and rectangular perforations. The fuel used in all the measurements was methane which was fully premixed with natural air forming a mixture with equivalence ratio φ. An illustration of the measurement setup is shown in Figure 3.1. It also illustrates different modules of the system, i.e., operating software, mixture supply, excitation and response, and control and safety.
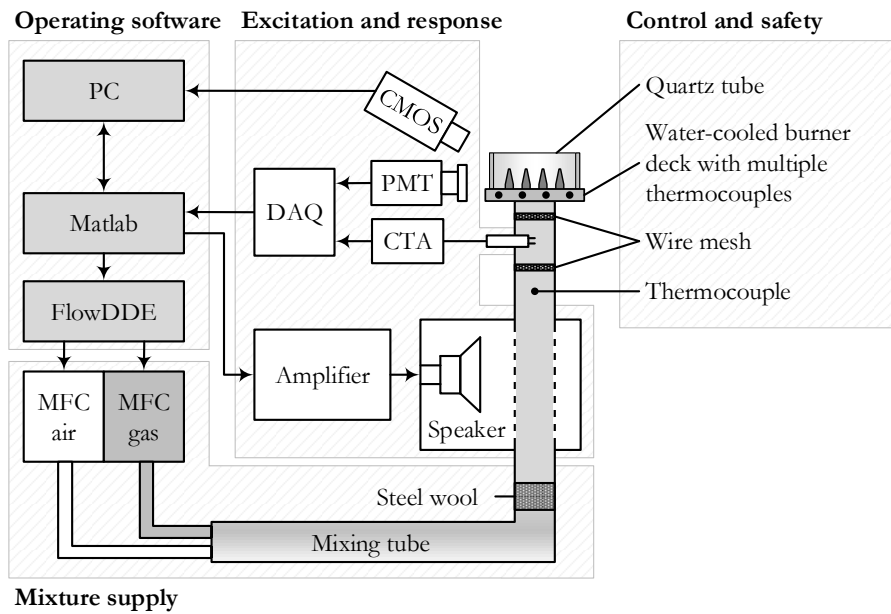
Figure 3.1: Schematic of the burner TF measurement setup showing the operating software, mixture supply, excitation and response, and control and safety modules of the system.

3.1.1 Operating software

The major operating software was *Matlab* that controls the mixture supply via *FlowDDE*, a software developed by *Bronkhorst High-Tech B.V.* for controlling the mass flow controllers (MFCs). In addition, the *Matlab* code was responsible for sending the excitation signal and reading the response signal and further post-processing to calculate the burner TF.

3.1.2 Mixture supply

The mixture was supplied using Bronkhorst's *EL-FLOW* and *LOW-ΔP-FLOW* MFCs for air and gas, respectively. It was specially realized that the MFCs do not operate at the lower and upper *15%* of the nominal capacity, in order to maximize measurement accuracy. Therefore, two sets of air and gas MFCs (low and high capacity) were used which could be selected based on the operating conditions. The mixing tube was chosen long enough (around *4m*) so that air and gas have enough time to completely mix before combustion. Mixing was further enhanced by placing steel wool inside the tube that also acted as a flow laminarizer.

3.1.3 Excitation and response

The acoustic excitation signal was generated by the computer sound card, amplified by an *HQ-Power VPA2100MN* amplifier and sent to a *JBL P953* speaker. It was ensured that the speaker response was linear for the whole frequency range (*10-1000Hz*) and it could produce a pure single-frequency sine wave. The excitation was performed as a sweep of single frequency harmonic waves. The resolution of the sweep could be as fine as *1Hz*. However, for most experiments a resolution

of *3* to *5Hz* was enough and it helped to reduce the duration of the frequency sweep. The part of the mixture supply tube that was inside the speaker housing, was perforated to allow propagation of acoustic waves. The distance between this section and the burner deck was large enough (around *1m*) to allow reformation of planar acoustic waves in the tube.

The generated velocity fluctuations were measured by a *Dantec Dynamics 55P16* single-sensor constant-temperature anemometer (CTA) probe which was placed *3cm* upstream of the burner deck. This distance is far enough to prevent acoustic deformation of waves due to the area change at the burner deck [43]. The level of velocity fluctuations were chosen between *7* to *10%* of the mean flow, which was large enough for good signal-to-noise ratio and small enough for the flame response to remain in the linear regime [43–45]. Since the CTA output voltage changes nonlinearly with flow velocity and the system has resonances at specific frequencies that may strengthen or dampen acoustic fluctuations, the excitation signal was automatically varied by the controlling code to make sure that a specific velocity fluctuation is achieved at the location where the CTA was placed.

The response of the burner was measured using a *Hamamatsu H10723-110* photomultiplier tube (PMT) equipped with *Omega* band-pass filters designed for *OH** radical (wavelength of *308nm*) or *CH** radical (wavelength of *430nm*) emissions. The filters had a full-width-half-max (FWHM) equal to *10nm*. This parameter is defined by the region of the passband where the transmission of the filter is *50%* of the maximum transmission. These radical emissions are shown to be good indicators of premixed methane-air flame heat release rate [46–48]. The *308nm*-filter for *OH** was used for most of the measurements since it operates in the UV range and can better filter out the possible noise from ambient light. However, some results were also checked with the *430nm*-filter for *CH** to increase the reliability of the results, but no significant deviation was observed.

The output voltage signals of the CTA and PMT were acquired by a *National Instruments NI9215* module, which is a 4-Channel, *±10V*, 16-bit simultaneous analog input module. The signals were acquired for one second with a sampling rate of *80kHz*, which was large enough to resolve the harmonic signal associated to the maximum frequency of interest (*1kHz*). The raw signals were further processed in *Matlab* to obtain the complex burner TF. The details of this calculation are presented in section 3.2 *"Burner transfer function calculation"*.

3.1.3.1 *Flame shape image processing*

In order to investigate the flame shape, a *Nikon D3200* DSLR camera with a CMOS sensor was used at *105mm* focal length to acquire bitmap images of the flames. The images were recorded under constant values of focal length, shutter speed, aperture and ISO sensitivity to perform reliable comparisons in various cases. A reference photograph was taken from a grid placed on top of the burner deck to calculate the flame height and compare it with simulations. Two types of coarse and fine grid with resolutions of *0.5* and *0.2mm* were used. A sample picture of the flames from various angles and an overlaid picture of the coarse grid are presented in Figure 3.2.
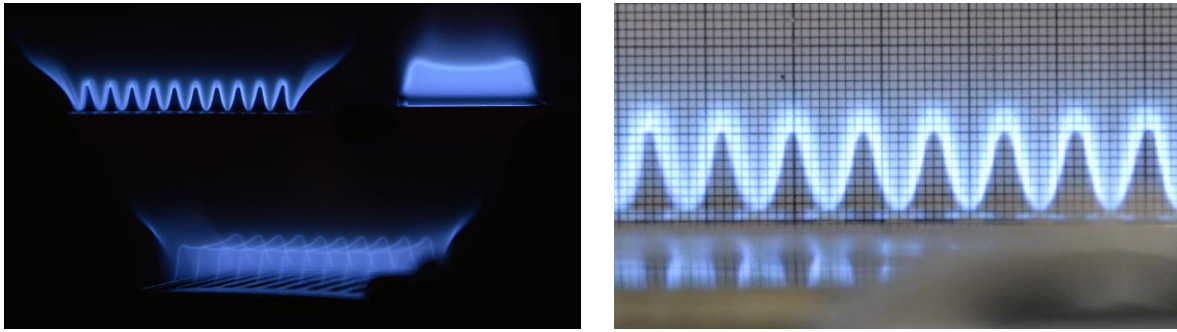
Figure 3.2: A sample picture of the flames (left) and image processing grid (right) acquired using the CMOS camera.

It was specifically considered that in burner decks with slits of high aspect ratio, deformations due to thermal expansion may occur. Therefore, a so-called double-deck configuration is applied, where the burner deck was split into two layers, fixated on top of each other with heat resistant tape. This configuration allowed room for thermal expansion and helped maintaining the shape of the burner deck and flame while heating up. Figure 3.3 shows the difference it made on the shape of the flames stabilized on a burner deck with *2.2×30mm* slits.

(a) (b)
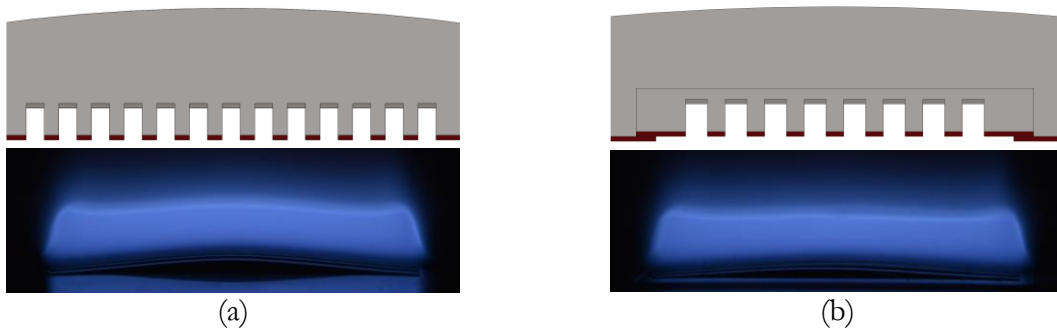
Figure 3.3: The single-deck (a) and double-deck (b) configuration of a burner deck with slits of 2.2×30mm. Thermal expansion deforms the burner deck and causes deformation of the metal bridge between two adjacent flames, which can be observed in the flame photos.

3.1.4   Control and safety

The measurement conditions need to be as controlled and stable as possible to ensure that the results are reliable. Moreover, working with premixed combustion requires specific safety considerations as well. Therefore, the following measures were taken,

- Placing a UV-transparent quartz tube on the burner deck surrounding the flames to prevent air entrainment and stabilize the flames better.
- Spot-welding multiple thermocouples below the burner deck to accurately measure the burner deck temperature distribution (placing them below the burner deck prevents them from absorbing radiation from the flames and false readings).
- Controlling the burner heat loss and temperature using a water jacket fixed to the burner edge with controlled inflow and outflow temperatures.
- Placing an extra thermocouple in the mixture supply tube to have a correct indication of mixture temperature and accurate flow velocity calculations.

- Fixing the CTA in a CTA-holder to keep its perpendicularity with the flow direction
- Embedding two layers of wire mesh in the supply tube (one between the burner and CTA, and one between the CTA and speaker) in order to prevent upstream propagation of flames in case of flashback. These wire meshes also helped to laminarise the flow.

A 3D model and a photo of the burner head showing some of these features is illustrated in Figure 3.4.
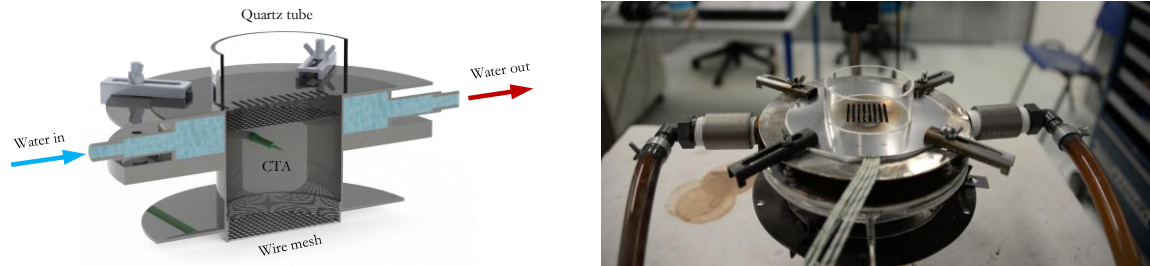
Figure 3.4: The 3D model (a) and photo (b) of the burner head showing the quartz tube, water jacket, CTA holder, and the two layers of wire mesh.

3.2 Burner transfer function calculation

The CTA and PMT voltages were harmonic and the PMT signal was lagging behind the CTA signal. Therefore, we have

$$v_{CTA} = \overline{v}_{CTA} + v'_{CTA} \sin(\omega t), \tag{3-1}$$

$$v_{PMT} = \overline{v}_{PMT} + v'_{PMT} \sin(\omega t - \phi), \tag{3-2}$$

where the overbar and prime signs denote the DC and AC parts of the signals, respectively. The DC offset for the CTA needs to be high enough to prevent the signal from crossing the zero line. If it does, the CTA measures double the actual frequency, since the heat transfer from the hot wire occurs regardless of the direction of flow velocity around it. [49]. A representation of the signals is illustrated in Figure 3.5.
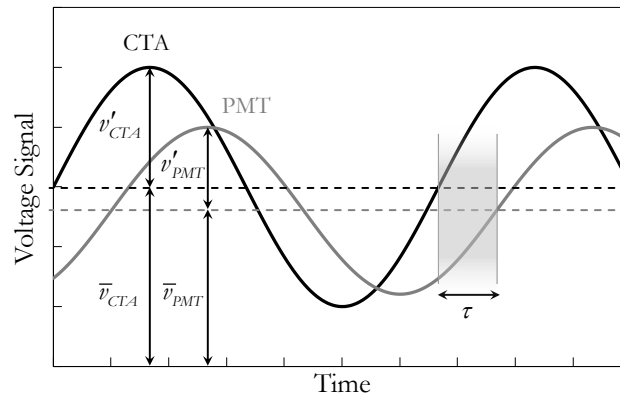
Figure 3.5: An illustration of the CTA and PMT signals showing their DC and AC parts, and the delay between them.

The gain and phase of a TF between the CTA and PMT signals would simply be equal to v'_{PMT}/v'_{CTA} and ϕ, respectively. In order to obtain these values, a discrete Fourier transformation (DFT) was applied to the signals and the signal TF was reconstructed as

$$TF_s(\omega) = \frac{\mathcal{F}(v_{PMT})}{\mathcal{F}(v_{CTA})} = N.G_s(\omega)e^{i\phi_s(\omega)}, \tag{3-3}$$

where $G_s(\omega)$ and $\phi_s(\omega)$ are the discrete frequency-dependent gain and phase of the complex $TF_s(\omega)$, respectively, and N is a normalization factor which is explained in the following section. Since the signals were harmonic and the calculations were performed in the frequency domain, no filtering was required and the raw signals were used. A sample of the CTA and PMT frequency responses at *70Hz* are presented in Figure 3.6. It is clearly visible that the signal to noise ratio was large enough to enable proper post-processing. This ratio was constantly monitored for all excitation frequencies to ensure a reliable signal. It can also be observed in Figure 3.6 that the first harmonics of the signals are present as well. However, they are one order of magnitude smaller than the original signal, which indicates linearity of CTA and PMT responses.
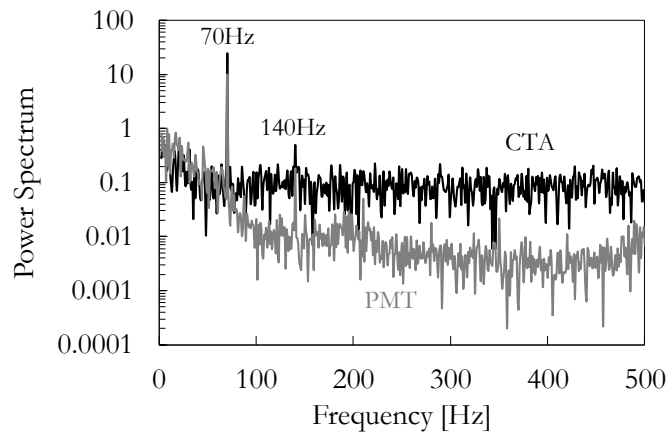
Figure 3.6: A sample of the CTA and PMT frequency responses at 70Hz.

3.2.1   Normalization of burner transfer function

As mentioned in section 3.1.3 *"Excitation and response",* the output voltage of the CTA and PMT are indirect measures of velocity and heat release. Therefore, a calibration is required in order to obtain the velocity and heat release data. The CTA response can be calibrated based on the mass flow controllers and mixture temperature. Based on the mass flow rate measured by the MFCs, the mixture density can be calculated and depending on the mixture temperature and cross sectional area, the bulk flow velocity is obtained. This calculation was incorporated in the *Matlab* code in order to use the obtained bulk flow velocity values as input for simulations.

The PMT calibration is more complicated, since the radical emissions from the flames vary by changing parameters such as equivalence ratio, burner load, PMT distance and angle. However, to measure the burner TF, no direct calibration is necessary if the relation between the signals and the measured quantities are known. If the relation is not linear, which is usually the case, it can be

linearized around the operating point, i.e. the quasi-steady-state. This is why before starting each measurement, TF normalization was performed by acquiring the mean signals for three conditions, i.e., the nominal operating condition and two extra states with *10%* smaller and larger mixture bulk velocity. The slope of the linearized relation between the CTA and PMT signals was then calculated and used as a normalization factor for calculating the gain of burner TF. This normalization ensures that the gain of burner TF converges to unity for very low frequencies (quasi-steady-state), which is simply based on the conservation of energy. Figure 3.7 shows an example of this normalization. The mean signals were acquired five times (the crosses) and an average of the values (the filled circle) was selected for the calculations. The scales of the axes on the left clearly show the repeatability of the normalization measurements.
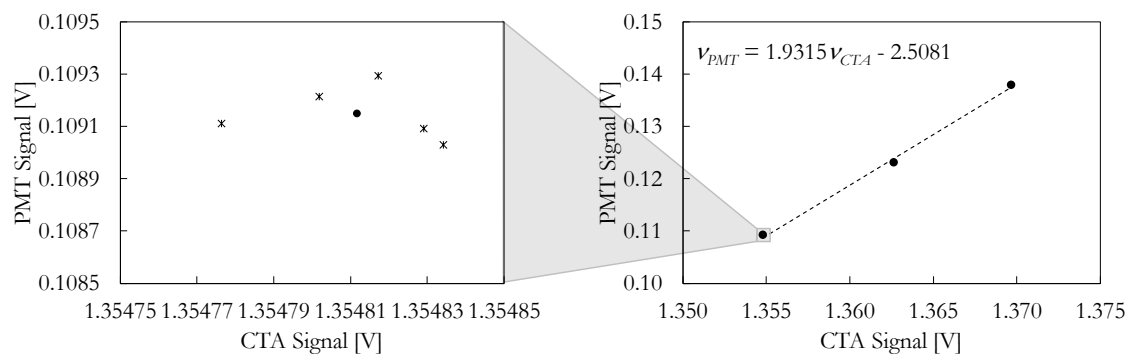
Figure 3.7: An example of the normalization factor measurement (the slope of the linearized relation between the CTA and PMT signals). The mean signals were acquired five times (the crosses) and an average of the values (the filled circle) is selected for the calculations.

Based on the described techniques and tools, the burner transfer function can be measured. Figure 3.8 shows an example of the gain (a) and phase (b) of the TF of a burner deck with *12* slits of *2.2×20mm*. The presented data shows very good repeatability and well-resolved curves for three independent measurements.
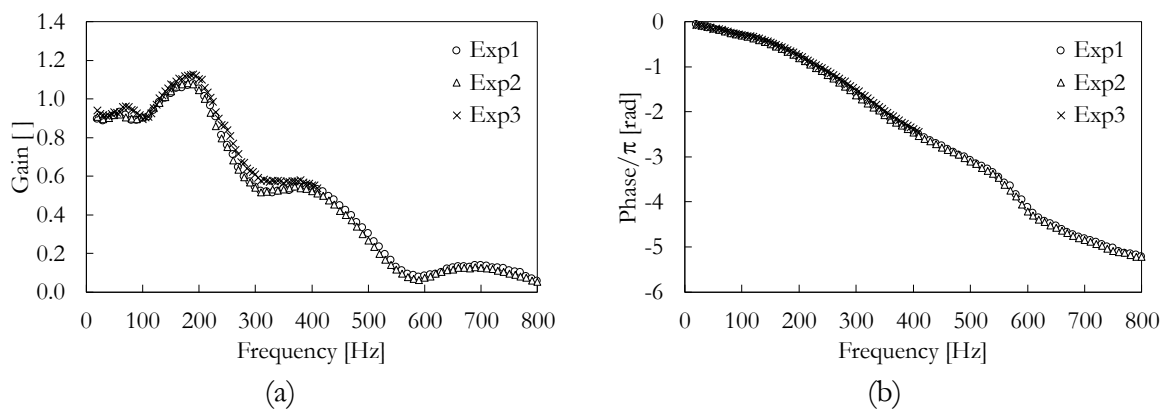
Figure 3.8: An example of three independent measurements of gain (a) and phase (b) of the TF of a burner deck with 12 slits of 2.2×20mm.

3.2.2 Burner deck temperature measurement

The burner decks were all made from round perforated stainless steel plates of *120mm* diameter and *0.6mm* thickness. The water-cooling was applied underneath the burner deck between radii *30* and *55mm* and a *1.5mm*-thick soft gasket layer was placed between the water ring and the burner deck in order to house the thermocouple wires and prevent leakage. The water temperature was maintained around *22°C* and high flow rate was used to minimize water heat-up to less than *1°C*, which is negligible. Since the stabilization temperature of the burner has considerable effects on the burner TF [50–52], it is crucial to perform accurate burner deck temperature measurements. This was performed via spot-welding multiple K-type thermocouples below the burner deck. Placing the thermocouples below the burner deck shields them from direct radiation from the flames and ensures more accurate measurements. Figure 3.9 illustrates the configuration of the thermocouples on a burner deck with *8* slits of *2.2×30mm*. The subscript denotes the bridge (the metal between the slits) number, and whether the thermocouple is welded on the inner (*i*) or outer (*o*) side of the bridge. Depending on the burner deck used and the importance of the resolution of the temperature distribution on the burner deck, a number of the indicated thermocouples were used. Nevertheless, T_{1i} and T_{5o} were always included to have an indication of the highest and lowest burner deck temperatures, respectively.
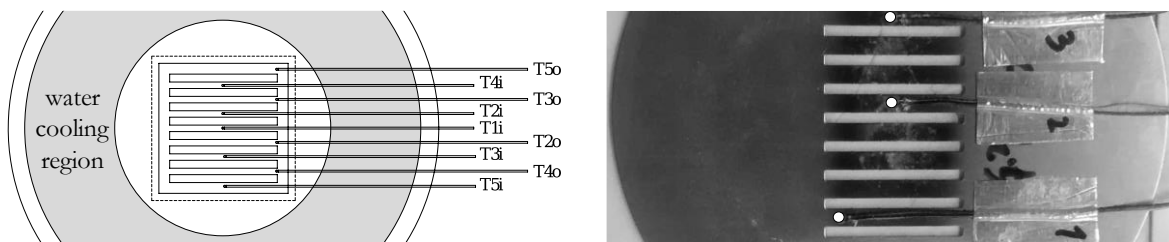
Figure 3.9: A burner deck with 8 slits of 2.2×30mm and multiple thermocouples spot-welded below it. The subscript denotes the bridge number and whether the thermocouple is welded on the inner (i) or outer (o) side of the bridge.

For each operating point, the temperatures were measured on a separate burner deck than the one used for TF measurements. The reason was to exclude the possible flow, and consequently flame, distortions due to the presence of the thermocouple wires upstream of the burner deck.

3.3 Possible measurement errors

The measured TF has a good reproducibility, as was shown in Figure 3.8. However, inherent errors of the measurement setup may cause inaccuracies in the measured data. The possible sources of such errors are addressed here.

3.3.1 TF measurement errors

Comparing the CTA and PMT time signals reveals that the main source of the noise in the data is the occasional fluctuations of flame radiation and the intrinsic noise of the PMT. Figure 3.10 shows these signals with and without excitation at *70Hz*. A small low-frequency component in the

CTA signal was present that could be due to the inherent flow fluctuations. The noise in the PMT signal was mainly due to the internal electrical circuits and had a much higher frequency than the range of interest (*1kHz*). It was already shown in Figure 3.6, that the main signal was at least one order of magnitude larger than the noise, which enables accurate post-processing.
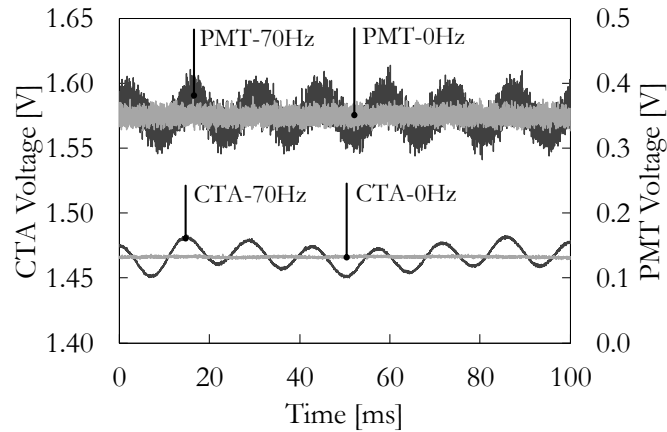
Figure 3.10: The CTA and PMT time signals for the unperturbed (0Hz) and perturbed (70Hz) cases.

The repeatability and reproducibility tests include TF measurement on different days (and sometimes with different hot-wire probes after disassembling and reassembling the setup). The results of these experiments show a maximum of *±0.1* scattering in TF gain and *±0.1π* scattering in TF phase (see Figure 3.8).

3.3.2 Flow rate and mixture equivalence ratio errors

The mass flow controllers described in section 3.1.2 *"Mixture supply"* have a maximum error of *±1%*, when operated within *15-85%* of their nominal capacity. This is declared by the producer and confirmed in frequent calibrations. All measurements were performed for lean flames with the equivalence ratio around *0.8* and various MFCs with different ranges were used for different conditions to make sure that the optimal MFC range was in use. Therefore, the MFC inaccuracies can be estimated by taking into account the chemical reactions. One mole of methane (molecular weight of *16g*) reacts with two moles of air (molecular weight of *29g*). Therefore, the stoichiometric fuel-to-air mass ratio is *0.275*. and it is *0.22* at equivalence ratio of *0.8*. The *±1%* error in the fuel or air mass flow rate causes the same error on the equivalence ratio. In the extreme worst case of the two errors occurring simultaneously, a linear summation of the errors leads to a maximum error of *±2%* in the equivalence ratio (in practice a quadratic summation is a more realistic case, which leads to only *1.41%* error). Nevertheless, this level of error in equivalence ratio may only negligibly change the burner TF [43].

3.3.3 Mixture bulk velocity errors

The mixture bulk velocity was measured as an input for simulations and normalizing the measured velocity fluctuations to achieve the desired level of acoustic velocity (see section 3.1.3 *"Excitation and response"*). The bulk velocity was calculated back from the mass flow rates and temperature-dependent mixture density. The mixture temperature was measured by a K-type thermocouple with an error of *±2°C* that induces maximum *±0.7%* error in the mixture density and bulk flow velocity. This error may be quadratically added to the *±2%* MFC error and lead to a final maximum of *±2.12%* for bulk flow velocity. Therefore, at the beginning of every measurement and just before starting the frequency sweep, steady-state time signal of the CTA was obtained for *5* durations of *5* seconds each, and the average bulk velocity is calculated. This procedure minimizes the effects of the discussed inaccuracies.

3.3.4 Geometrical errors

There are various geometrical tolerances in the system, of which the supply tube diameter and the burner deck perforation size are the most important. These dimensions were measured with an error below *±1%* that leads to maximum *±2%* error in the area. Accordingly, together with the mass flow rate and bulk flow temperature measurement, the error in bulk flow velocity reaches *±2.91%* (using quadratic sum of independent errors).

Another geometrical measurement was the flame height. It was measured by a grid with *0.2mm* accuracy, as discussed in section 3.1.3.1 *"Flame shape image processing"*. For most of the flames in this study with *6-10mm* height, this equals a maximum of *±3.4%* error in the flame height measurement.

3.4 Numerical tools and methods

This section deals with introducing the numerical tools and methods used in this work. The first part includes the computational fluid dynamics (CFD) setup for calculating burner and heat exchanger TFs. The second part discusses the system identification analysis where the eigenmodes of the system are examined. The data obtained from CFD provides a framework for the network model and Helmholtz solver to find the stability bounds of the system.

3.4.1 CFD simulations of transfer functions

The CFD simulations were performed in *ANSYS® Fluent 17.0* [53] with the mesh generated in *Gambit*. The burner and heat exchanger were simulated in various 2D and 3D configurations in order to find a good match with the experimental results.

3.4.1.1 *Conservation equations*

The conservation equations explained here are mainly obtained from [53] and adapted to the conditions of this work. The continuity equation in the absence of mass sources is written as

$$\frac{\partial \rho}{\partial t} + \nabla.\left(\rho \vec{v}\right) = 0,$$ (3-4)

where ρ, t and $\vec{v}$ denote the density, temperature and velocity vector, respectively.

The momentum equation when the gravitational and external body forces are neglected can be written as

$$\frac{\partial}{\partial t}\left(\rho \vec{v}\right) + \nabla.\left(\rho \vec{v}\vec{v}\right) = -\nabla p + \nabla.\left(\bar{\bar{\tau}}\right),$$ (3-5)

where p and $\bar{\bar{\tau}}$ denote the pressure and stress tensor, respectively. The stress tensor for an incompressible flow is given as

$$\bar{\bar{\tau}} = \mu\left(\nabla \vec{v} + \nabla \vec{v}^T\right),$$ (3-6)

where μ denotes the molecular viscosity.

The energy equation in the absence of viscous heating is written in the form of

$$\frac{\partial}{\partial t}\left(\rho E\right) + \nabla.\left(\vec{v}\left(\rho E + p\right)\right) = \nabla.\left(k\nabla T - \sum_i h_i \vec{J}_i\right) + S_h,$$ (3-7)

where k and T denote the conductivity and temperature, and h_i and J_i indicate the enthalpy and diffusion flux of species i. The heat of chemical reactions is included in the source term S_h and the energy is denoted by E and can be written as

$$E = \sum_i Y_i h_i + \frac{v^2}{2},$$ (3-8)

where Y_i denotes the mass fraction of species i.

The species conservation equation is then given as

$$\frac{\partial}{\partial t}\left(\rho Y_i\right) + \nabla.\left(\rho \vec{v} Y_i\right) = -\nabla.\vec{J}_i + R_i,$$ (3-9)

where R_i is the net rate of production of species i by chemical reactions. The diffusion flux of species i (J_i) in equations (3-7) and (3-9) arises due to gradients of concentration and temperature. The Fick's law is used to describe the diffusion flux as

$$\vec{J}_i = -\rho D_{i,m} Y_i.$$ (3-10)

Here $D_{i,m}$ is the mass diffusion coefficient for species i in the mixture. Using methane as the fuel justifies assuming unity Lewis number and neglecting the thermal (Soret) diffusion. Therefore, the mass diffusion coefficient becomes

$$D_{i,m} = \frac{k}{\rho c_p},$$ (3-11)

where k, ρ and c_p denote the thermal conductivity, density and specific heat of the mixture, respectively.

Combustion was modeled using finite-rate chemistry for a two-step reaction mechanism as

Reaction 1: $CH_4 + 1.5O_2 \Rightarrow CO + 2H_2O,$ (3-12)

Reaction 2: $CO + 0.5O_2 \Leftrightarrow CO_2.$ (3-13)

In general, the molar rate of creation or destruction of species i in reaction r is given by

$$\hat{R}_{i,r} = \left(v''_{i,r} - v'_{i,r} \right) \left(k_{f,r} \prod_{j=1}^{N_r} \left[C_{j,r} \right]^{\eta'_{j,r}} - k_{b,r} \prod_{j=1}^{N_r} \left[C_{j,r} \right]^{\eta''_{j,r}} \right), \tag{3-14}$$

where

$v''_{i,r}$ is the stoichiometric coefficient for product i in reaction r,

$v'_{i,r}$ is the stoichiometric coefficient for reactant i in reaction r,

$k_{f,r}$ is the forward rate constant for reaction r,

N_r is the number of chemical species in reaction r,

$C_{j,r}$ is the molar concentration of each reactant and product species j in reaction r,

$\eta'_{j,r}$ is the forward rate exponent for each reactant and product species j in reaction r,

$k_{b,r}$ is the backward rate constant for reaction r,

$\eta''_{j,r}$ is the backward rate exponent for each reactant and product species j in reaction r.

The rate constant for reaction r is computed using the Arrhenius expression

$$k_r = A_r T^{\beta_r} e^{-E_r/RT}, \tag{3-15}$$

where A_r is the pre-exponential factor, β_r is the temperature exponent, E_r is the activation energy of the reaction, and R is the universal gas constant (*8314.34J/kmol-K*). The temperature dependency of reaction rates are neglected, so β_r is set to zero. Table 3.1 lists the corresponding input values for the reactions obtained from [53]. The pre-exponential factor of Reaction 1 is further tuned to yield more accurate results (see section 3.4.1.5 *"Validations"*). The rate exponents for species are only mentioned if they are not zero.

Table 3.1: The values used in the finite-rate chemistry formulation for the two-step reaction mechanism.

	A_r [consistent units]	E_r [J/kmol]	$\eta'_{j,r}$ or $\eta''_{j,r}$	
Reaction 1	1.58×10^{12}	2×10^8	CH_4	0.7
			O_2	0.8
Reaction 2 forward	2.24×10^{12}	1.7×10^8	CO	1
			O_2	0.25
			H_2O	0.5
Reaction 2 backward	5×10^8	1.7×10^8	CO_2	1

The explained conservation equations were solved using *ANSYS® Fluent 17.0* with a coupled approach for pressure and velocity, along with second order spatial discretization for momentum, energy and species. The transient formulation was first-order implicit (using second-order did not change the results, but slowed down the simulations). More details of the solution methods are available in [53].

3.4.1.2   Geometry and meshing

A sample of the 3D geometry of a multiple-slit burner deck together with a few rows of heat exchanger tubes are presented in Figure 3.11. Varying dimensions are indicated with letters and the upstream and downstream parts of the numerical domain were set to *5* and *100mm*, respectively. These distances were chosen large enough for the thermal and viscous non-uniformities to damp out. In the 3D simulations, symmetric conditions were used in both X and Y directions, thus only one-fourth of one slit perforation was considered. The slit perforation dimensions were L_1 and L_2, and the pitch between the perforations were P_1 and P_2. The horizontal distance between the heat exchanger tubes was chosen equal to P_1 so that each flame had a corresponding heat exchanger tube downstream of it.
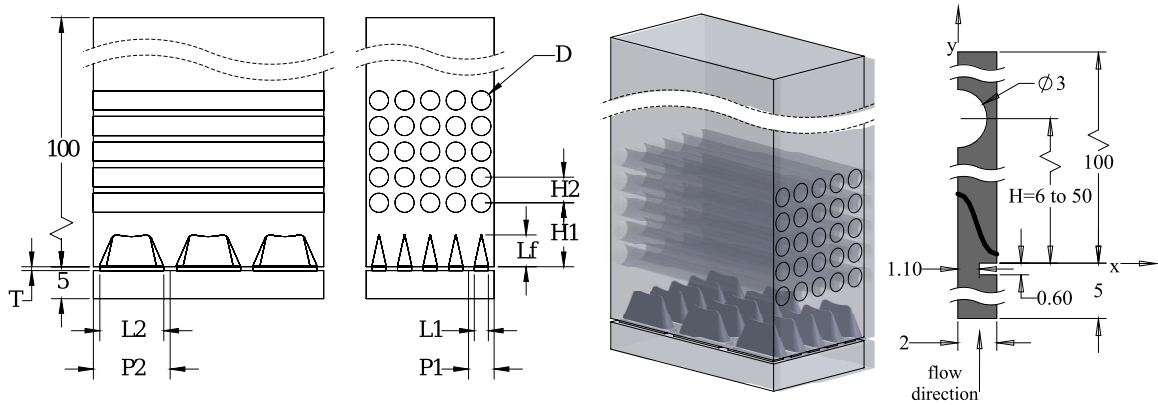
Figure 3.11: The 3D domain containing a multiple-slit burner deck and a multiple-tube heat exchanger showing the related dimensions, as well as a sample of the simplified 2D domain containing one slit and one row of heat exchanger tube.

In 2D simulations, three major patterns of burner deck perforations were studied, i.e. the slit, and rectangular and hexagonal patterns of round holes. The slit and hole patterns were simulated in Cartesian 2D and axisymmetric 2D domains, respectively. In order to find the correct geometrical settings for the axisymmetric cases, an equivalent area and pitch needs to be calculated. Figure 3.12 includes the schematic for this calculation for the rectangular and hexagonal patterns. The equivalent radius (used in axisymmetric simulations) was chosen so that the area of the equivalent circle (shown as the shaded area in Figure 3.12) was equal to the area of the smallest polygon surrounding a hole. Therefore, we have

for the rectangular pattern: $\pi \left(\dfrac{P_{eq}}{2} \right) = P^2 \Rightarrow P_{eq} = \sqrt{\dfrac{4}{\pi}} P \approx 1.13 P$,　　　　　　(3-16)

for the hexagonal pattern: $\pi \left(\dfrac{P_{eq}}{2} \right) = \dfrac{\sqrt{3}}{2} P^2 \Rightarrow P_{eq} = \sqrt{\dfrac{2\sqrt{3}}{\pi}} P \approx 1.05 P$.　　　　　(3-17)
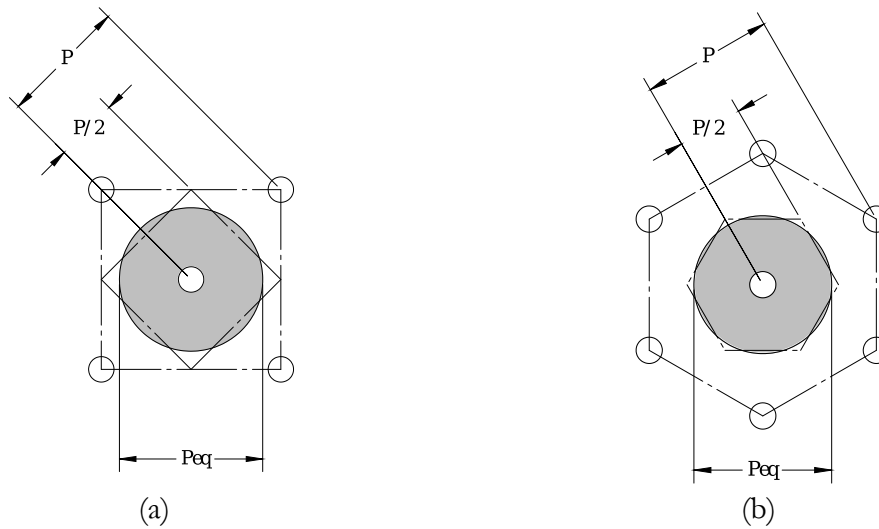
Figure 3.12: Schematic of the equivalent area and equivalent pitch calculation for the rectangular (a) and hexagonal (b) patterns.

The grid size used in the simulations was *160μm*, which was refined to *40* and *20μm* around the heat exchanger and burner, respectively, in order to resolve the thermal boundary layer and flame thickness properly. These values were obtained after careful comparisons with the literature and grid independency checks and were kept consistent in almost all simulations. More details are discussed in section 3.4.1.5 *"Validations"*. Figure 3.13 illustrates the meshing zones.
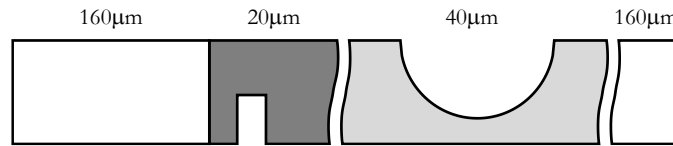
Figure 3.13: The simulation grid size that is 160μm and refined to 40 and 20μm around the heat exchanger and burner, respectively.

The naming conventions for different burner deck configurations are listed in Table 3.2.

Table 3.2: The naming conventions for different burner deck configurations.

Configuration	Generic naming convention	Example
Rectangular slit perforations – multiple rows	D(L$_1$-L$_2$ in mm)_P(P$_1$-P$_2$ in mm)_ V(perforation velocity in m/s)_ φ(equivalence ratio)	D2.2-10_P4-12_V1.2_φ0.8
Rectangular slit perforations – single row	D(L$_1$-L$_2$ in mm)_P(P$_1$-0 in mm)_ V(perforation velocity in m/s)_ φ(equivalence ratio)	D2.2-10_P4-0_V1.2_φ0.8
Circular hole perforations	DR(hole diameter in mm)_P(P in mm)_ Rect/Hex(hole pattern)_V(perforation velocity in m/s)_φ(equivalence ratio)	DR2.2_P4_Rect_V1.2_φ0.8

3.4.1.3 *Boundary conditions and material properties*

The simulation domain is presented in Figure 3.11. The inlet boundary was set to constant velocity, the outlet boundary to atmospheric pressure and the lateral boundaries to symmetric. Some studies have suggested using a correction factor for flame expansion effects [54]. However, these effects marginally alter the flame TF and do not change the nature of the interactions and the conclusions to be drawn. The burner deck and heat exchanger had isothermal boundaries with the values obtained from measurements. Here, the heat exchanger walls were thin and the constant temperature assumption was acceptable. Nevertheless, if a more accurate and detailed investigation is required, conjugate heat transfer needs to be taken into account.

The mixture was methane-air with equivalence ratio of φ (*0.8* for most of the work). The specific heats of all individual species were obtained from temperature-dependent polynomials and their viscosities and thermal conductivities using the kinetic theory. The corresponding properties of the mixture were then available using the mixing law [53].

3.4.1.4 TF *calculation*

In order to obtain the burner and heat exchanger TF or TM, transient simulations were performed to calculate their responses to a block change in velocity. This was done by imposing a step function with *5%* increase in the inlet velocity as excitation. The response of the burner was then calculated using the volume integral of reaction source term, which indicates the burner heat release rate. The response of the heat exchanger was calculated using the surface integral of heat flux through the heat exchanger walls. It was particularly checked that the time step size (*10μs*) is small enough to capture the premixed flame dynamics. It was also checked that the perturbations are small enough to prevent nonlinearities and can be regarded as a broadband excitation covering a wide range of frequencies. This approach has proved to be efficient and representative of obtaining the system response using multiple harmonic excitations [55].

In Figure 3.14, a sample of the step excitation and response signals for the burner and heat exchanger are plotted. The signals are normalized to their corresponding values before the excitation. The excitation was applied at *t=0ms* and after *40ms* relaxation time (of which only *10ms* is plotted in Figure 3.14), the system stabilized at the new operating point and then a step back to the original value was imposed. This created a periodic signal for Fourier transformation. The periodicity can also be manually created by mirroring the signals (if nonlinearity by hysteresis is not expected), which is the procedure used in most of this work. Note that the reference point for calculating TF of a specific acoustic element is usually chosen at a distance upstream of the element, where the acoustic waves can be assumed planar. Consequently, for the burner the combined effects of the flame and flame holder are considered.
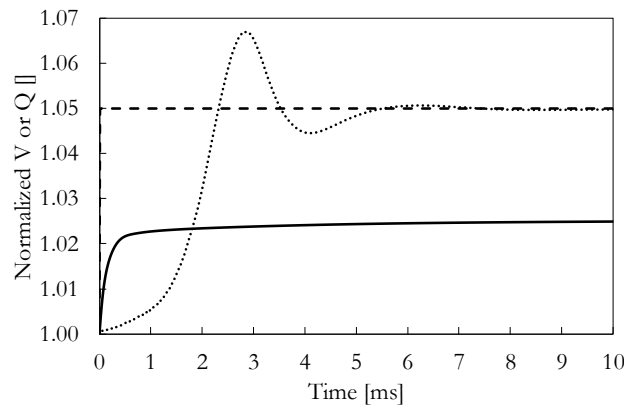
Figure 3.14: Samples of normalized excitation (− −) and response signals of the burner (·····) and heat exchanger (——). The periodic signal is created by manually mirroring these signals.

3.4.1.5 Validations

The most complicated part of the CFD simulations is the correct prediction of the burner response to acoustic fluctuations. However, it is first necessary to resolve the steady flame and capture flame characteristics, such as flame shape, temperature and laminar flame speed.

3.4.1.5.1 Pseudo-1D flame validations

The initial validations were performed in a pseudo-1D domain in order to obtain the correct laminar flame speed. The width of this domain was equal to the size of one element and its length was large enough to enable capturing the movement of the flame front. The boundary conditions were similar to the actual 2D case, but with no heat exchanger (see section 0 "

Boundary conditions and material properties"). If the inlet velocity is equal to the laminar flame speed, the flame position does not change. If it is not, then the difference between the inlet velocity and the flame movement velocity indicates the laminar flame speed. Figure 3.15 shows the variations of the reaction heat and temperature profiles with time, and illustrates that the flame is moving towards the outlet (right hand side). Therefore, in this specific case, the inlet velocity is larger than the laminar flame speed.
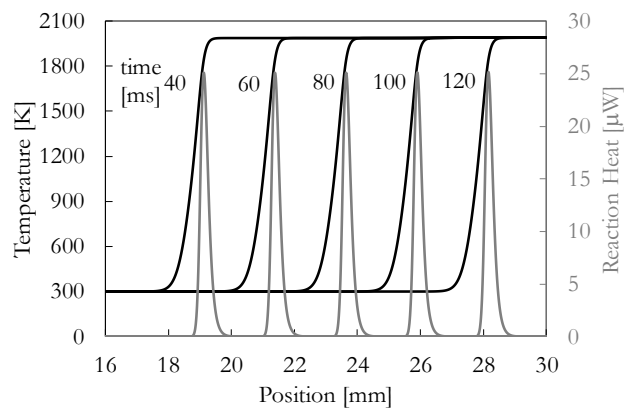
Figure 3.15: The variations of the reaction heat and temperature profiles with time, illustrating that the flame is moving with constant shape and velocity towards the outlet (right hand side).

The laminar flame speed was also used for grid independency study, where the grid size was refined from *100* down to *20μm*. Figure 3.16 shows the laminar flame speed and the number of elements inside the flame front for each refinement level. This number of elements can be calculated from dividing the flame thickness (obtained from the reaction heat graphs in Figure 3.15) to the element size. It can be observed that further refinements were not necessary and *20μm* is chosen for the flame zone.
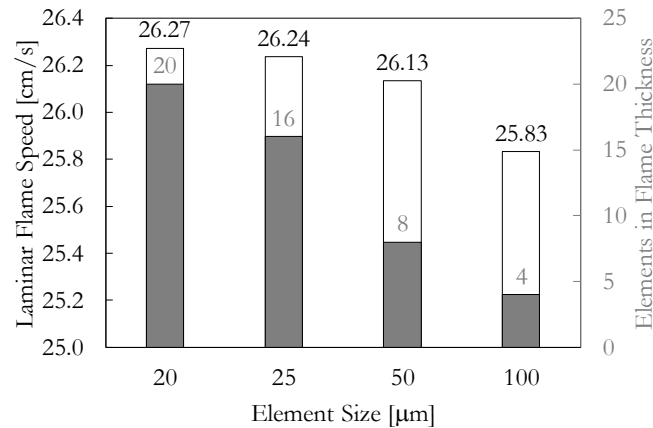
Figure 3.16: The laminar flame speed (white bars) and the number of elements inside the flame front (gray bars) for each refinement level.

Using the chosen grid size and the described methods for laminar flame speed calculation, various simulations were performed in order to obtain a laminar flame speed close to the literature data. The dependency of the laminar flame speed to the changes in equivalence ratio and unburned mixture temperature were analyzed and the results are plotted in Figure 3.17a and b, respectively. These pseudo-1D simulations were used for tuning the pre-exponential factor of Reaction 1 in Table 3.1. It can be observed that the tuned chemistry nicely follows the trends presented in the literature.
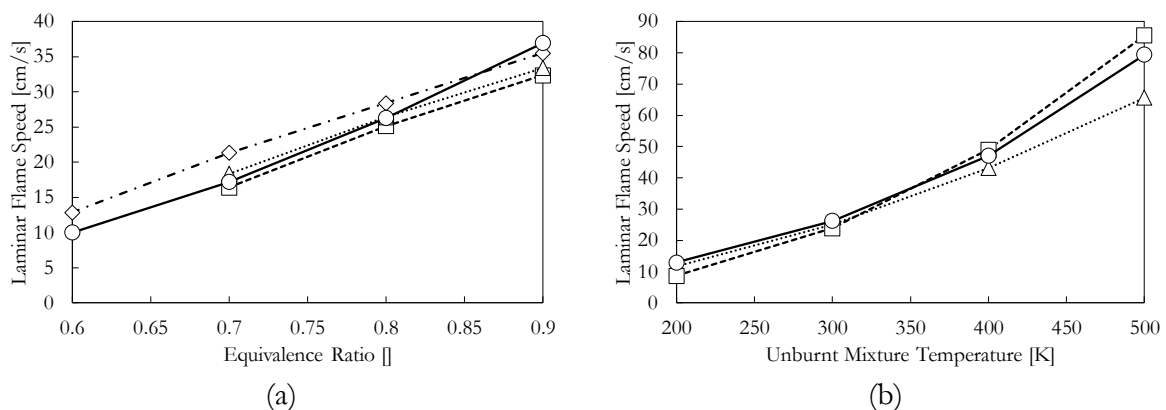
Figure 3.17: The dependency of the laminar flame speed to equivalence ratio (a) in this study (○) compared with the data from de Lange (◇) [56], Dyakov et al. (□) [57] and Kishore et al. (△) [58], and to the unburned mixture temperature (b) in this study (○) compared with the data from Sharma et al. (△) [59] and Brown et al. (□) [60].

3.4.1.5.2 2D steady and unsteady validations

The steady 2D simulations of the burner were performed using various reaction mechanisms including the simple 1-step, the modified 2-step (see Table 3.1), and skeletal mechanics such as GRI3 [61] and DRM19 [62]. The results are presented in Figure 3.18 and illustrate good agreement regarding flame height, thickness and standoff distance between the 2-step mechanism used in this work and the detailed skeletal mechanisms. The 1-step reaction mechanism, however, predicted a larger flame thickness and smaller standoff distance. The thicker flame is an inaccuracy that is common in over-simplified reaction mechanisms. Conversely, the 2-step mechanism predicted a slightly thinner flame and a larger standoff distance compared to the skeletal mechanisms, but the transient results of burner TF (see further) obtained using this mechanism show a better match with the measurements.
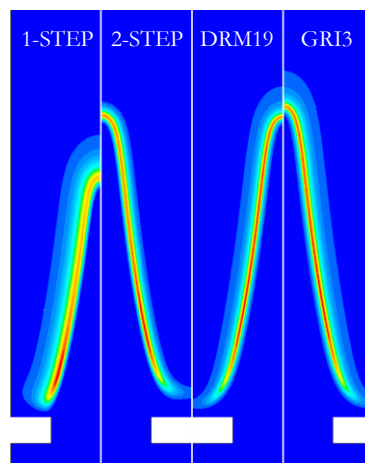
Figure 3.18: The steady flame shape when simulating using the 1-step, modified 2-step (see Table 3.1), DRM19 and GRI3 reaction mechanisms.

The TF validation of the burner with 2D unsteady stretched flames was performed in comparison with the work of Kornilov et al. [24]. They provided measurement and DNS simulation results of wedge flames stabilized on a perforated deck. This work was chosen because the configuration was close to this study and their results had been confirmed in other independent studies as well [54]. The comparison of the steady flame shape and the TF gain and phase are presented in Figure 3.19a and b, respectively. This comparison also provides a double check for the laminar flame speed and flame height, since these parameters significantly affect the TF [24, 54, 63]. The results show that the model is able to reproduce the experimental and numerical data from the literature with good agreement.
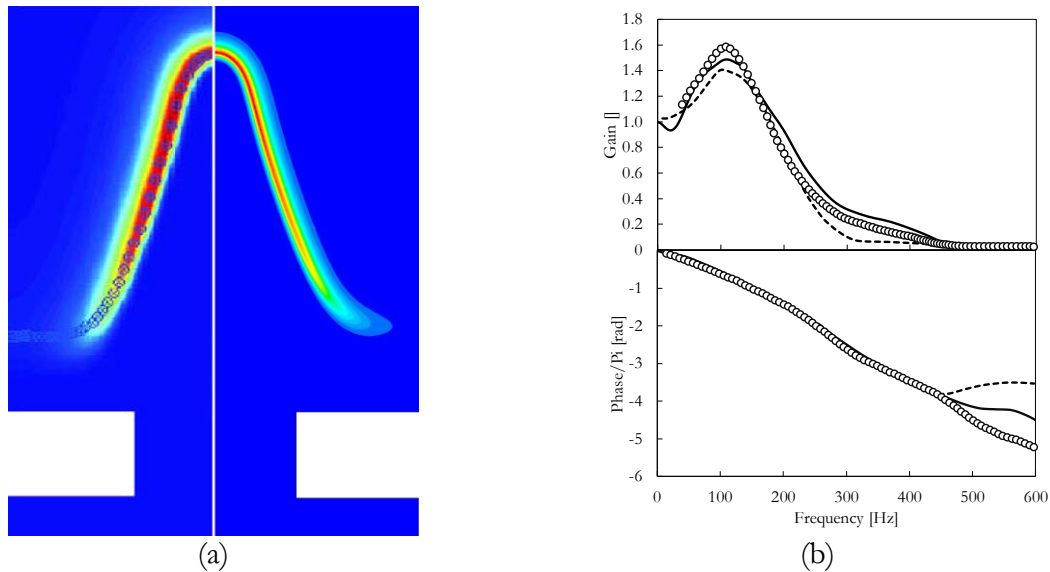
Figure 3.19: The comparison of the flame shape in the simulations of Kornilov et al. [24] *(left side of (a)) and that of this work (right side of (a)), and the flame transfer function (b) in this work (━) and the simulations (━ ━) and experiments (○) of Kornilov et al.* [24].

The introduced and verified CFD model is used in the rest of this work for simulating the response of various burners and heat exchangers to the velocity oscillations.

3.4.2 System identification analysis

This section deals with explaining the tools used for solving the characteristic equation of the system (Equation (2-9)), in order to obtain its complex eigenfrequencies. Some basic theory and equations are already discussed in section 2.3 "*Thermoacoustic theory*" and the remaining are presented here.

3.4.2.1 *Network modelling using taX*

One of the tools used for system identification is *taX*, a state-space network modelling tool developed by *Technical University of Munich*. This network model is a low-order simulation tool for the propagation of acoustic waves in an acoustic network and is able to determine stability, mode shapes, frequency responses, scattering matrices and stability potentiality of acoustic networks of arbitrary topology. The state-space modeling approach used in *taX* is numerically efficient as it is based on matrices with constant, frequency-independent coefficients. This provides a standard linear eigenvalue problem to be solved directly in small to moderate model sizes. However, for large models an iterative algorithm is required [64]. The environment for running *taX* is *Matlab Simulink* and it requires the Control System and System Identification toolboxes.

Figure 3.20 shows a representative network model of a typical heating appliance, as presented in Figure 1.2. The inlet and outlet can be open, closed, or have a specific reflection coefficient and there are various acoustic ducts between the elements. The burner and heat exchanger are similar elements that each include a TF defining their active thermoacoustic behavior, related area changes and ducts inside, and a temperature change.
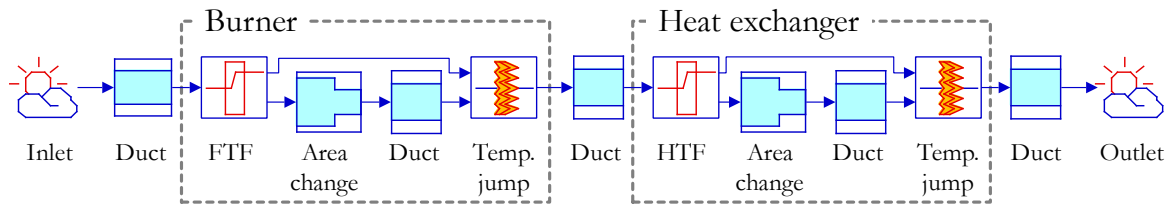
Figure 3.20: A representative network model of a typical heating appliance in taX, as presented in Figure 1.2.

The model for the TF of the burner or heat exchanger can be either a simple *n-τ* model or a generic TF obtained from simulations (see section 3.4.1 *"CFD simulations"*) or measurements (see section 3.2 *"Burner transfer function calculation"*). It is worth mentioning that in measurements of burner TF, it is usually not possible to measure only the flame TF without the effects of the flame holder. However, it is possible in *taX* to include the acoustic effects of the area changes and ducts in the flame holder. More information on the details of the elements and methods in *taX* can be found in the user's guide and element documentation [65].

3.4.2.2 FEM acoustic simulations using Comsol

The acoustics module of *Comsol* consists of a set of physics interfaces that enable simulating the propagation of sound in fluids and solids. Acoustic simulations using this module can easily solve classical problems such as scattering, diffraction, emission, radiation, and transmission of sound [42]. Such finite element method (FEM) solvers are required for solving the Helmholtz equation in complicated geometries, such as realistic heating appliances. Therefore, they are crucial in translating the findings in simplified configurations to full-scale systems in order to improve the designs.

Implementing the inhomogeneous Helmholtz equation (Equation (2-9)) in Comsol is relatively straightforward and consists of the following three steps [41],

- Defining the source terms for all the active acoustic elements
- Defining a coupling operator (averaging or extrusion coupling in Comsol) that would couple the source to the acoustic velocity
- Iteratively solve the nonlinear eigenvalue problem

3.4.2.2.1 Implementing the active acoustic source (monopole source)

Referring back to Equation (2-9), we have the Helmholtz equation in the form of

$$\frac{\omega^2}{\overline{c}^2}\hat{p} + \overline{\rho}\nabla.\left(\frac{1}{\overline{\rho}}\nabla\hat{p}\right) = -i\omega\frac{\gamma-1}{\overline{c}^2}\frac{\overline{Q}}{\overline{u}}\mathbb{F}\hat{u}.$$

Since for perfect gases $\gamma\overline{p} = \overline{\rho}\overline{c}^2$, it can also be written as

$$\frac{\omega^2}{\overline{c}^2}\hat{p} + \nabla.\left(\frac{1}{\overline{\rho}}\nabla\hat{p}\right) = -i\omega\frac{\gamma-1}{\gamma\overline{p}}\frac{\overline{Q}}{\overline{u}}\mathbb{F}\hat{u}. \tag{3-18}$$

A series of manipulations can make this equation easily implementable in Comsol. Taking into account that $\overline{Q}$ is per unit volume, the non-dimensional temperature is defined as

$$\theta = \frac{T_b}{T_c} - 1 = \frac{\Delta T}{T_c} = \frac{\overline{Q}V}{\dot{m}c_p T_c} = \frac{\overline{Q}V}{A\overline{u}\rho c_p T_c},$$ (3-19)

where V denotes the total volume, A the cross-sectional area and the subscripts b and c the hot and cold values, respectively. Taking the ideal gas assumption, we have $p=\rho RT$ and c_p and c_v are functions of temperature only. With the additional assumption that the specific heats are constant over the temperature range of interest (perfect gas assumption), and considering $R=c_p-c_v$ and $c_p/c_v=\gamma$, we can rewrite θ as

$$\theta = \frac{\overline{Q}V}{A\overline{u}} \frac{\gamma - 1}{\gamma \overline{p}}.$$ (3-20)

Considering only one-dimensional disturbances and a harmonic heat input concentrated at the plane $x=b$, the solution of the wave equation can be calculated as explained in [31]. Substituting Equation (3-20) in (3-18) and considering the Dirac δ-function, we get

$$\frac{\omega^2}{\gamma \overline{p}} \hat{p} + \nabla \cdot \left(\frac{1}{\overline{\rho}} \nabla \hat{p} \right) = -i\omega \delta (x-b) \theta \mathbb{F} \hat{u}.$$ (3-21)

This equation can be easily implemented in Comsol if an approximation of the Delta function is available. For the heat release in a finite length s centered around $x=b$ we have [66, 67]

$$\delta (x-b) = \begin{cases} 0 & \text{if } b-s/2 > x > b+s/2 \\ 1/s & \text{if } b-s/2 < x < b+s/2 \end{cases}.$$ (3-22)

Therefore, the total heat release rate in the whole domain is the same as if it would be concentrated in a plane. Since $\lim_{s \to 0} \frac{1}{s} = \delta(x)$ we have

$$\int_{-\infty}^{\infty} \delta(x) dx = \int_{-s/2}^{s/2} \frac{1}{s} dx = 1.$$ (3-23)

The thickness of the monopole source is then easily inserted in the source definition in Comsol.

3.4.2.2.2   Geometry, meshing and boundary conditions

Comsol was used in both simplified and realistic geometries in order to calculate the eigenvalues of the system in this thesis. Figure 3.21 shows both the geometry of a simple Rijke burner and a full-scale heat cell in Comsol. The heat cell includes a blower, cylindrical burner, parallel heat exchanger sections and exhaust. The inlet and outlet boundaries were set to open and were, in most cases, acoustically fully reflecting. However, a parametric study was also performed where the inlet and outlet reflection coefficients are varied (see section 6.1 *"Intrinsic thermoacoustic modes and their interplay with acoustic modes in a Rijke burner"*). The rest of the boundaries were treated as sound-hard boundaries. The Rijke burner features two active elements that are representatives of the burner and the heat exchanger, respectively. The burner in the full-scale case is cylindrical and the heat exchanger is a distribution of heat sinks (pins).

(a)   (b)
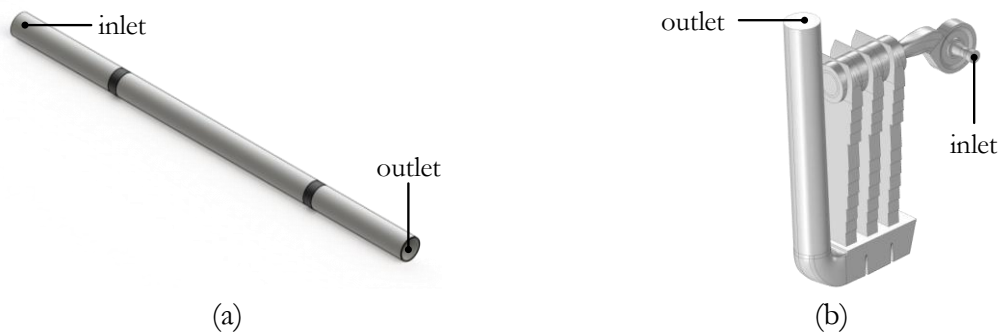
Figure 3.21: The geometry of a simple Rijke tube (a) and a full-scale heat cell (b) in Comsol showing the boundary conditions. The heat cell includes a blower, cylindrical burner, parallel heat exchanger sections and exhaust. (image courtesy of Bekaert Combustion Technology B.V. [68]).

Figure 3.22 shows a part of the Rijke burner model in Comsol and illustrates the grid size used in the monopole source. It is important to include a few grid points along the source to create an accurate coupling [69]. In the rest of the domain, the meshing is automatic (controlled by Comsol).
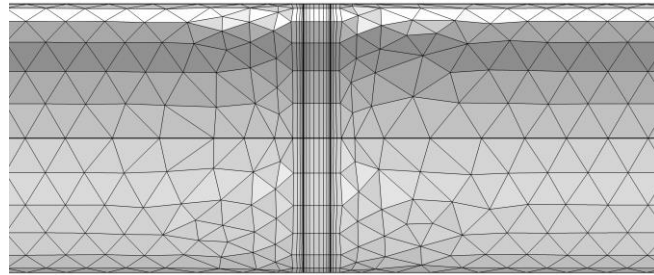
Figure 3.22: The generated mesh inside and around the monopole source in the Rijke burner.

3.4.2.3 Solution of the eigenvalue problem

The solution of the constructed eigenvalue problem in the network model or Helmholtz solver yields the complex eigenfrequency of the system, that consists of the eigenfrequency (real part) and its corresponding growth rate (imaginary part). A positive growth rate that is larger than the decay rate due to acoustic damping in the system, results in an unstable system. The results are predominantly presented as pole-zero plots and mode shapes, in the form of distribution of acoustic pressure or acoustic velocity in the system. Figure 3.23 shows the acoustic pressure in the simulation domain for the Rijke burner and a full-scale heat cell.
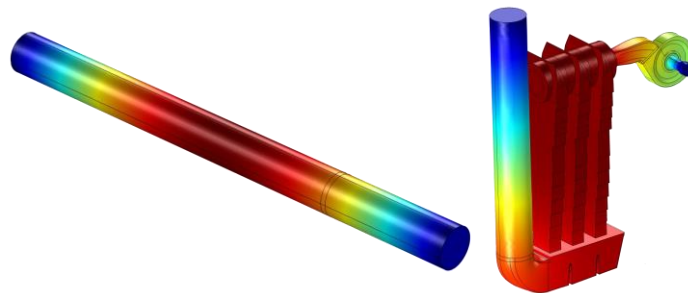
Figure 3.23: Acoustic pressure in the simulation domain for the Rijke burner and a full-scale heat cell (images courtesy of Bekaert Combustion Technology B.V. [68]).

Transfer Functions of the Burner and Heat Exchanger as Segregated Active Elements

The acoustic properties of passive elements such as ducts, area changes and terminations are, in most cases, readily available [39]. This leaves the properties of the active elements to be defined in order to achieve closure of the system equation (see section 2.3.2 *"Helmholtz equation"*). Since the burner and heat exchanger are the major active thermoacoustic elements in heating appliances, this chapter deals with identifying their transfer functions separately as two independent elements. These elements are considered velocity-sensitive and the tools and methods used in obtaining their transfer functions are discussed in Chapter 3.

4.1 Transfer function of practical laminar premixed burners

Laminar premixed burners are found in various designs and configurations of heating systems. Most commonly used designs include variations of surface-stabilized flames that are formed downstream of a perforated or porous surface. Figure 4.1 shows some possible configurations of practical burners, i.e. perforated cylindrical (a), metal fiber cylindrical (b), metal fiber flat (c), and ceramic flat (d) burners.

Figure 4.1: Some possible configurations of practical burners, i.e., perforated cylindrical (a), metal fiber cylindrical (b), metal fiber flat (c), and ceramic flat (d) burners (images a, b and c courtesy of Bekaert Combustion Technology B.V., and image d courtesy of American Range Corporate).

Since the flames that are stabilized on these surfaces may be quite complex, various simplifications have been considered in the early studies of flame transfer function. The initial investigations on the response of flames to acoustic forcing have been focused on single Bunsen-type flames that provides a simple but informative setup for flame transfer function investigations. The experiments and simulations on single-flame setups have revealed that the heat release fluctuations in laminar premixed flames is directly related to the flame front dynamics. i.e. flame wrinkling [70]. The first theoretical description of these wrinkles made considerable use of the n-τ model developed by Crocco, originally for rocket engines [71]. This model is vastly used to date by researchers for various types of laminar and turbulent flames [22]. Merk has been among the first to identify the transfer function of laminar premixed conical flames [72]. He found that the FTF phase increases with frequency and flame height, but the low-pass characteristic of the FTF gain was not properly captured.

The next step in analyzing the flame dynamics was taken with the introduction of flame front tracking methods, such as the G-equation [73]. Such methods were capable of analyzing the motion of the flame front by relating it to the incoming flow patterns and fluctuations [73–75]. Using the G-equation, Fleifil et al. [76] showed that the FTF of a single long conical flame depends only on a flame Strouhal number defined as $St=\omega R/S_u$, where ω is the angular frequency, R is the perforation radius and S_u is the laminar flame speed. Ducruix et al. [77] generalized this dependence to all flame sizes by incorporating the flame half angle α and introducing a reduced frequency $\omega^*=\omega R/S_u Cos\alpha$. The obtained results were in good agreement with the measurements, except for the FTF phase at high frequencies. This shortage was compensated by Schuller et al. [78] taking into account that the low-frequency perturbations are convected with the mean flow. Consequently, they identified the FTF as a function of the reduced frequency and flame angle independently. They were able to reconstruct the increasing behavior of the FTF phase with frequency in conical flames as well as the phase saturation of flat flames.

Considerable progress has been made by Lieuwen et al. in multiple stages to analytically describe the flame response taking into account the mean flow velocity profile, anchoring point dynamics, flame stretch and flame curvature [22]. However, quantitative comparison of the obtained theoretical results with experiments or simulations was not thoroughly performed.

The experiments of Kornilov [43] and Karimi et al. [79] have shown the contribution of flame anchoring point dynamics to the wrinkling and phase behavior at high frequencies. The heat

transfer in the anchoring region has also been the focus of some researchers [50, 80]. They have found that the flame stabilization conditions may significantly modify the FTF.

The dynamics of the unburned mixture are critical in defining the flame response. One of the aspects that has been neglected in analytical expressions of the FTF is the exothermicity [81, 82]. In confined flames (either by walls or neighboring flames), the overpressure caused by the exothermicity may modify the steady-state velocity field. This may cause flow acceleration in the streamwise direction and increase the flame length. However, this effect is easily captured in CFD simulations and has been reported in the DNS work of Schlimpert et al. [83].

As shown in Figure 4.1, industrial premixed perforated-plate burners usually feature a variety of circular and rectangular perforation patterns with dimensions small enough to prevent flashback. Therefore, it is of practical interest to study multiple flames and of small dimensions. Researchers have shown that multiple flames, unlike single flames, may feature FTF gains exceeding unity, i.e. gain overshoot [18, 24, 84, 85]. Noiray et al. [32] found this feature in small conical flames for a relatively large range of excitation frequencies. They also reported that the acoustic response of such flames are still governed by convective velocity waves that result in an increasing FTF phase with frequency. They also found that the response of a cluster of small flames cannot be properly captured by kinematic models [76–78, 86].

If the perforation size is reduced sufficiently and a high porosity flat burner is used, then planar laminar flames may stabilize downstream of the burner. This configuration has been widely investigated at *Eindhoven University of Technology* [87–94] (some of these works are reviewed in [95]). This series of investigations led to the conclusion that the combined effects of acoustic fluctuations and unsteady heat transfer between the flame and the burner surface is what governs the FTF of such flames. Rook et al. [88] developed an analytical model to predict the FTF of premixed flat flames and showed that the gain overshoot can be due to constructive interferences between the motion of the flame anchoring point and the heat and mass transfer between the flame and the burner surface. Other researchers have further developed this model to analyze the FTF of small conical flames stabilized on perforated surfaces [18, 96]. They associated the gain overshoot to flame burning velocity oscillations due to unsteady heat loss to the burner, and indicated that flame area oscillations become dominant at frequencies higher than the overshoot frequency. Their predictions showed good agreement with DNS when the standoff distance and burner surface temperature are properly adjusted, but comparison with experiments were not as successful [97].

Kornilov et al. [24] performed experiments and DNS of the FTF of conical methane/air flames stabilized downstream of rectangular slits. They parametrically studied the effects of the mixture bulk velocity, equivalence ratio, slit width and distance between slits, and were able to qualitatively capture the measured FTF using simulations at a fixed burner deck temperature of *100 °C*. They concluded their work by mentioning the following recommendations for analytical analysis of similar flames. First, to predict the FTF phase lag it is necessary to combine a kinematic model including a model for the creation of convective waves at the burner outlet. Second, to predict the FTF saturation, the jagged behavior and, probably the effect of the gain overshoot, it is necessary to develop a method to describe the dynamics of the flame-anchoring zone. Finally, including a model for the flame retroaction to the upstream flow and flame-to-flame interaction in the

multiple-flame configurations could improve the accuracy and capability of kinematic models to predict the FTF of practically interesting burners.

Several other studies have also pointed out the importance of developing FTF research towards realistic and practical burners [82, 90, 98, 99], which is an integral part of this work as well. These studies have shown the effects of various parameters, such as perforation size, distance between perforations, flow velocity, equivalence ratio, and material and bulk temperature of stabilization surface on the FTF. The following two subsections are dedicated to some further fine details of the TF of laminar conical flames stabilized downstream of flat plates with round and rectangular perforations. Since the flame shape and stabilization conditions are sorted among the most important parameters in defining the TF of such flames, they earn the focus of this chapter. The effects of the 3D flame shape vs. 2D flame shape are analyzed in section 4.1.1 *"Three-dimensional effects"* and the effects of surface temperature profiles are discussed in section 4.1.2 *"Effects of stabilization temperature"*.

4.1.1   Three-dimensional effects

From the various burner types illustrated in Figure 4.1, the ones featuring perforated plates are very common type in the heating industry. The majority of such burners feature circular and/or rectangular (slit) perforations. In CFD simulations of such flames, the flame thickness needs to be properly resolved by choosing a numerical grid size in the order of a few tens of micrometers (this concern is addressed in Figure 3.16 of section 3.4.1.5.1 *"Pseudo-1D flame validations"*). In case of steady flames, this requires local refinement in the flame region, and in case of unsteady flames, either a dynamic mesh that is updated based on the flame shape and position, or defining a larger refinement zone to contain the flame front for all unstable cases. Therefore, these perforations are usually treated as Cartesian or axisymmetric 2D in order to reduce the computational effort of full-scale 3D simulations. This approach has been chosen by many researchers in the field of thermoacoustics, but has not been fully investigated if it poses systematic errors. One may, for example, argue about the specific length to width ratios of slit flames to be compared to 2D simulations. On the other hand, flame chemistry is known to be the most influencing factor in predicting heat release and thus acoustic response of laminar flames. Therefore, many of discrepancies that are observed in comparing simulations to measurements are minimized by fine-tuning the flame chemistry. However, in the course of validations for this work, it was found that there are inherent 3D geometrical effects that play an important role in the flame response. Neglecting these effects may result in over-tuning the model in other aspects such as the chemistry. In simulating 3D cylindrical patterns as 2D axisymmetric geometries, the equivalent pitch and area are important (this is addressed in Figure 3.12 and Equation (3-16) and (3-17) of section 3.4.1.2 *"Geometry and meshing"*), and in simulating 3D rectangular slit patterns as Cartesian 2D, the length-to-width ratio of the slits. The rest of this section deals with the latter case, which is found to be the potential cause of some specific characteristics of FTF.

Figure 4.2a illustrates a set of photographs taken from different angles from a series of flames stabilized on a burner deck with rectangular slits (*D2.2-4_P4-20*). The corresponding 3D simulation results are shown in Figure 4.2b that features a temperature isosurface (to illustrate the flame shape)

and the contours of flow velocity magnitude just downstream of the burner deck. The velocity contours show an intense flow contraction and increased velocity at the two ends of the slit perforations, causing the two 'humps' on either sides of the flame. In this case, a 2D simulation may still be considered acceptable in comparison to a cross-section of the 3D flame at the middle of the flame length. However, the variations in the rest of the length may pose considerable inaccuracies, because they are simply not taken into account in 2D simulations.

(a)   (b)
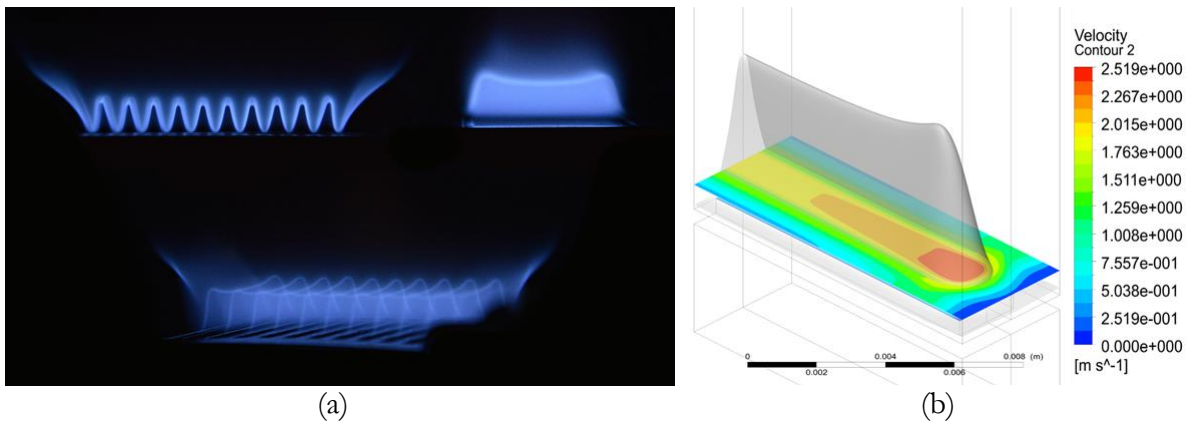
Figure 4.2: Photographs (a) and 3D simulations (b) of flames stabilized on a burner deck with rectangular slit perforations (D2.2-4_P4-20). The contours in (b) illustrate the flow velocity magnitude and show intense flow contraction and increased velocity in the two ends of the slit perforations.

A first step in identifying the 3D effects of slit fames is to analyze the effects of the aspect ratio, i.e. the ratio of the slit length to its width. It is clear that in the limit case of very long slits, the 2D simulations are acceptable. Nevertheless, the 3D flame surface shown in Figure 4.2b can be decomposed into two major parts, a purely 2D (wedge) part and two caps on either ends. Further detailed analysis of flame surface shows that the geometry of these caps is most similar to half of an oblique cone with the base diameter equal to the slit width. Figure 4.3 shows an illustration of the right and oblique cone geometries, showing the slit width (L_1), slit length (L_2) and flame height (L_f). In the oblique cone method, the location of the tip of the cones are estimated by analyzing the flame images for a specific case (*D2.2-4_P4-20*).

(a)   (b)
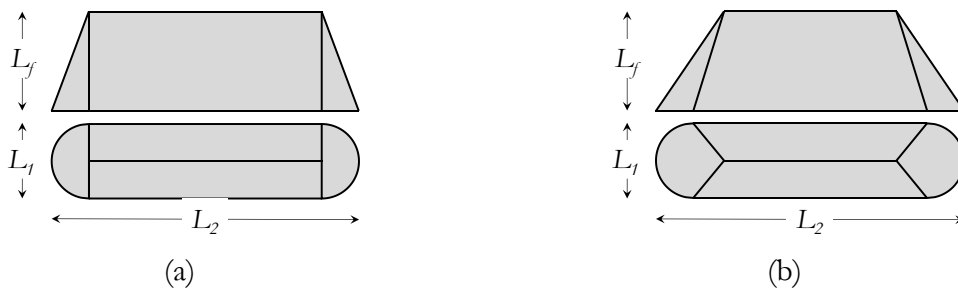
Figure 4.3: The side and top views of the simplified geometry of a right cone flame (a) and an oblique cone flame for the specific case of D2.2-4_P4-20 (b).

The contribution of these conical parts to the total flame area for various slit aspect ratios $\alpha = L2/L1$ is shown in Figure 4.4. The conical share β is defined as the ratio of the conical to total

flame area and is calculated using three methods, the ratio, right cone and oblique cone. In the ratio method, only the width and length of the perforation is considered and the conical share is calculated as

$$\beta = \frac{L_1}{L_1 + L_2} = \frac{1}{1 + \alpha}.$$

(4-1)

In the right cone method, the cone axis is assumed perpendicular to the base. Using some geometrical calculations, the flame height L_f can be ruled out and the conical share becomes

$$\beta = \frac{\pi\left(\frac{L_1}{2}\right)\left(\sqrt{L_f^2 + \frac{L_1^2}{4}}\right)}{\pi\left(\frac{L_1}{2}\right)\left(\sqrt{L_f^2 + \frac{L_1^2}{4}}\right) + 2\left(L_2 - L1\right)\left(\sqrt{L_f^2 + \frac{L_1^2}{4}}\right)} = \frac{1}{1 + \frac{4}{\pi}(\alpha - 1)}.$$

(4-2)

It can be seen from Equations (4-1) and (4-2) that the ratio and right cone methods lead to the same estimation of conical share when the slit aspect ratio is $\alpha = 4.66$ (this value can be traced back in Figure 4.4, where the solid and dashed lines collide). It can also be seen in Figure 4.4 that the ratio method still provides a good estimation of the conical share. However, the most important conclusion from this figure is that even with a slit aspect ratio as high as *10*, still around *10%* of the flame area is conical. If the acoustic response of this conical part is inherently different from the wedge parts, this can pose significant systematic errors in 2D simulations, because it is well-known that the FTFs of laminar premixed flames are dominated by flame area fluctuations.
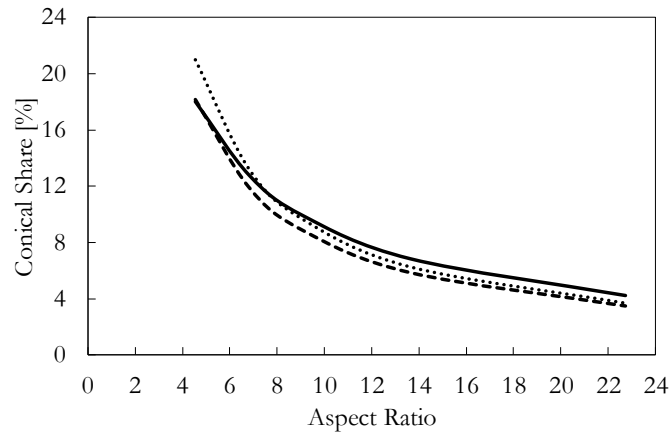
Figure 4.4: The contribution of the conical part of a slit flame to the total flame area for various slit aspect ratios (L_2/L_1), using three different methods, ratio (—), right cone (– –) and oblique cone (·····).

Motivated by these findings, 3D simulations were performed for slit dimensions of *2.2* by *10*, *15*, *30* and *50mm* (thus aspect rations of *4.55*, *6.82*, *13.64* and *22.73*, respectively), perforation velocity of *1.2m/s* and equivalence ratio of *0.8*. The FTF of the flames were compared to that obtained from 2D simulations and the results are presented in Figure 4.5. The FTF phase is hardly affected, which is due to the same flame height in all cases, but the gain clearly shows the convergence to that of the 2D case as the aspect ratio increases. Note that the jagged behavior of the gain is an artifact of simulating with slightly coarser grid in order to make the heavy 3D

simulations possible with the available computational resources. Nevertheless, the trends are clearly visible in the graph.
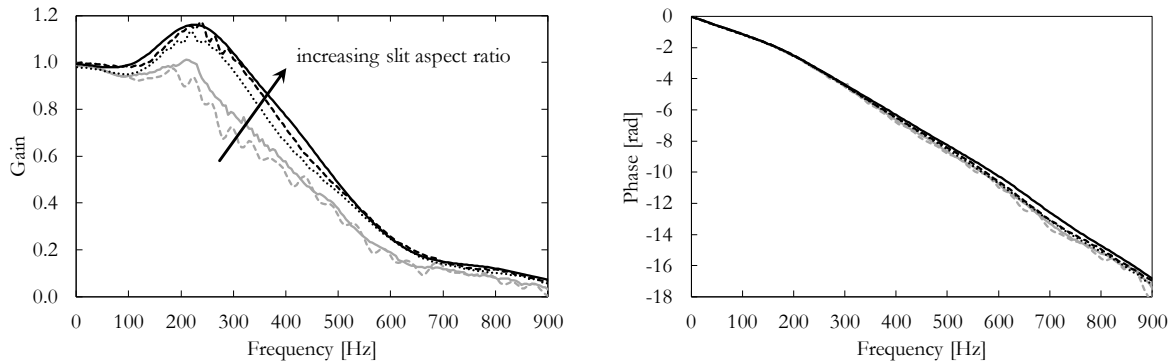
Figure 4.5: The simulated gain and phase of FTF of a 2D flame of 2.2mm width (solid black line), and corresponding 3D flames with length of 10mm (aspect ratio of 4.55) (dashed gray line), 15mm (aspect ratio of 6.82) (solid gray line), 30mm (aspect ratio of 13.64) (dotted black line) and 50mm (aspect ratio of 22.73) (dashed black line). The perforation velocity is 1.2m/s and the equivalence ratio is 0.8.

The same analysis was performed by measurements, where burner decks with slit perforations of *2.2* by *6*, *10* and *15mm* (thus aspect ratios of *2.73*, *4.55* and *6.82*, respectively) were used. Figure 4.6 illustrates the burner decks used in this measurement (note that the results of larger slit lengths are not reliable due to buckling of long bridges between the slits and distorted flame shape (see Figure 3.3)). The perforation velocity was *1.2m/s* and the equivalence ratio *0.8*. Due to the geometrical effects, the porosity of the burner decks vary slightly between *42-48%*, but this amount was negligible in the measured burner deck temperatures.
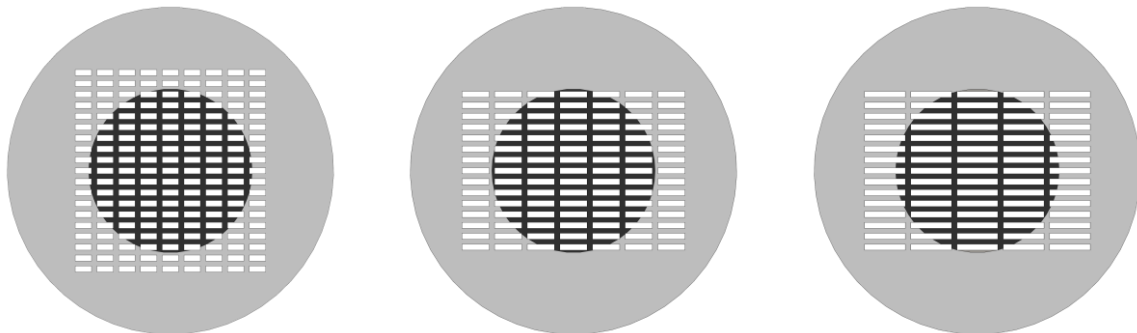
Figure 4.6: The burner decks with slit perforations of 2.2 by 6, 10 and 15mm (thus aspect ratios of 2.73, 4.55 and 6.82, respectively) to show the measurement results if increasing slit aspect ratio.

Figure 4.7 shows the results of the measurements and that the same trends as in the simulation results (see Figure 4.5) are observed. The discrepancies between the simulations and measurements may be due to the burner deck temperature profiles, which were not taken into account in the simulations. In addition, the real burner decks featured several incomplete flames around the edge that can contribute to these discrepancies. Nevertheless, the observed trends with increasing slit aspect ratio are similar in simulations and measurements.
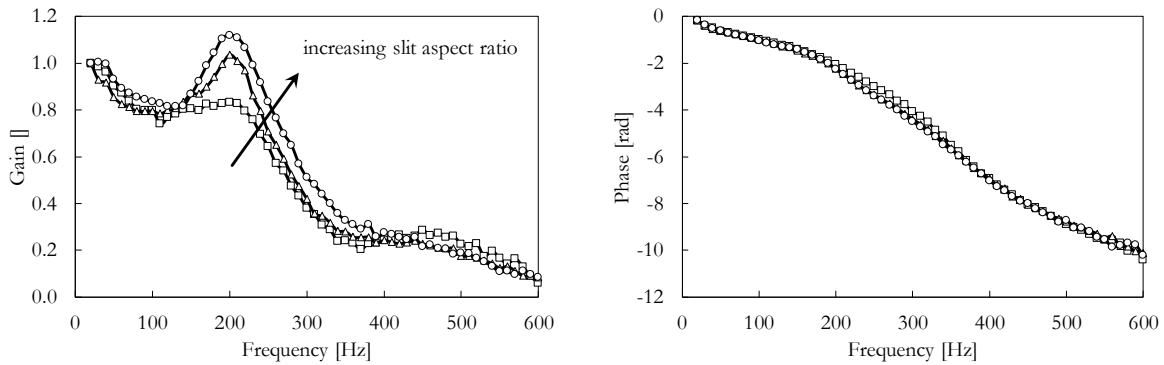
Figure 4.7: The measured gain and phase of burner TF with perforations of 2.2 by 6 (▱), 10 (△) and 15mm (◯), thus aspect ratios of 2.73, 4.55 and 6.82, respectively. The perforation velocity was 1.2m/s and the equivalence ratio 0.8.

Based on the presented data, an aspect ratio below *10* would pose significant deviations from the purely 2D simulation. Maintaining such high aspect ratios has not always been the case in the literature, and CFD simulations of flames with much smaller aspect ratios were reported to be in good agreement with measurements [24, 54, 89, 100]. This poses the probability of unknowingly solving geometrical problems by over-tuning other parameters, such as chemistry, in the simulations.

For practical reasons, such as manufacturing, the slit perforations in the premixed perforated burners do not usually feature a high aspect ratio. In simulating such kind of burners, it may be possible to combine the wedge and conical parts of the flame to reproduce a combined acoustic response of the total flame. Assuming that the two half-cone caps on either sides of the slit flame can form one fully conical flame, a combination of Cartesian and axisymmetric 2D simulations can be performed to obtain more accurate results. This combination can be done directly on the heat release data, or after obtaining the complex FTFs in the frequency domain using weighing factors proportional to the surface area of the wedge and conical parts. Figure 4.8 shows the results of the latter combination method next to the measured FTF for case *D2.2-20_P4-22_V1.2_ϕ0.8* (slit aspect ratio of *9.1*). The combinations are manually created by calculating a weighted sum of the complex FTFs of the pure Cartesian 2D (dark blue) and pure axisymmetric 2D (dark red) simulations. The percentage of the 2D part is indicated on the figure. It is clearly observed that a pure Cartesian 2D simulation is not fully capable of reproducing the fluctuations in the FTF gain, while these fluctuations do exist at the correct frequencies in the axisymmetric simulations. Therefore, a combination of Cartesian and axisymmetric simulations would lead to a better prediction of the burner response. The weighing factors for this combination can be retrieved from Figure 4.4, which for the aspect ratio of *9.1* results in the weighing factor of *0.9* and *0.1* for the Cartesian and axisymmetric parts, respectively. However, the results presented in Figure 4.8 show that a combination with even higher weighing factor for the axisymmetric case is more desirable. This shows that the actual contribution of the conical part of the real flame might be even higher than only the area ratio.

Figure 4.8 also shows that for frequencies below the first dent in the FTF gain (around *400Hz*), the phase changes gradually between the Cartesian and axisymmetric cases by changing the weighing factor. However, for higher frequencies a phase jump occurs that results in a separation

between the two groups of curves, the ones dominated by the Cartesian or by the axisymmetric case. The phase of the measured FTF matches well with the Cartesian-dominated cases, while the fluctuations of gain match better with the axisymmetric-dominated cases. This makes it difficult to judge which method better captures the complex FTF.
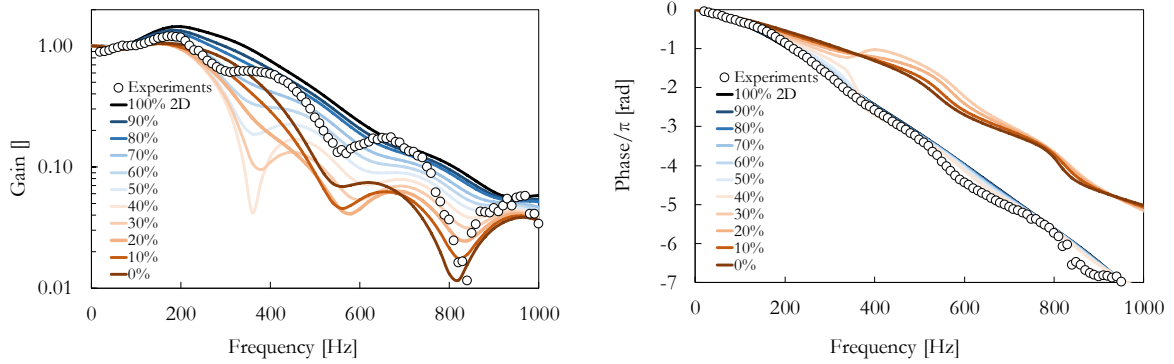
Figure 4.8: Combining the complex FTF of a pure Cartesian (dark blue line) and a pure axisymmetric (dark red line) 2D simulation with various weighing factors indicated with shades of blue and red (the values mentioned are associated to the 2D part. The experimental measurements are plotted with markers for D2.2-20_P4-22_V1.2_ϕ0.8.

Additionally, more accurate measurements were performed on only one row of slits (to minimize flame-flame interactions around the caps) and with better controlled burner decks (including water cooling and buckling control as indicated in Figure 3.3b of section 3.1.3.1 *"Flame shape image processing"*) for case *D2.2-4_P20-0_V1.2_ϕ0.8*. These results are presented in Figure 4.9, where it is found that the FTF gain in the measurements is actually "bound" by that of the Cartesian and axisymmetric simulations. This indicates that the dominance of various parts of the slit flame FTF may be frequency-dependent and different mechanisms take over depending on the excitation frequency.
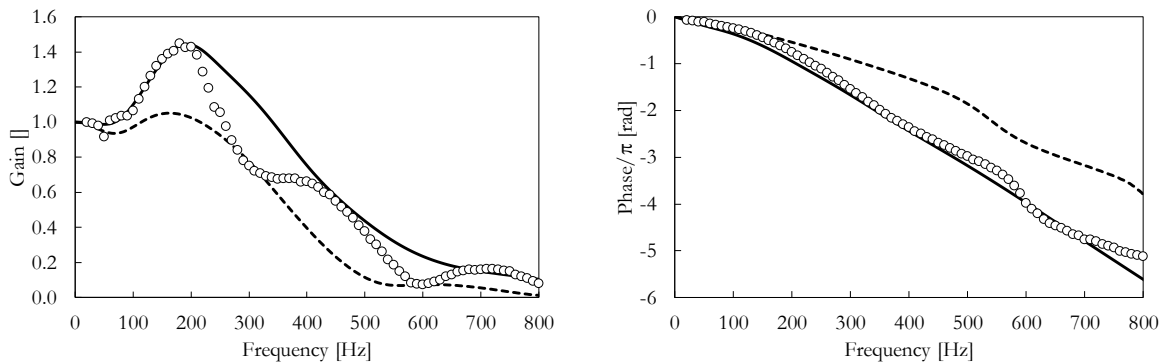
Figure 4.9: The gain and phase of FTF for case D2.2-4_P20-0_V1.2_ϕ0.8, measurements (markers), pure Cartesian (solid lines) and axisymmetric simulations (dashed lines). FTF gain in the measurements is "bound" by that of the 2D and axisymmetric simulations.

These observations can also be explained mathematically by simply considering the constructive and destructive combinations of two complex numbers with different phase behaviors. Let us consider two hypothetical complex FTFs in the form of *n*-*τ* models as, $FTF_1 = n_1 e^{-i\omega\tau_1}$ and

$FTF_2 = n_2 e^{-i\omega\tau_2}$, where $n_1=1$, $n_2=0.4$, $\tau_1=1ms$ and $\tau_2=5ms$. Since the time delays are constant, the phase increases linearly with frequency, with a slope proportional to the value of the time dely. The gain and phase of FTF_1, FTF_2 and FTF_1+FTF_2 are plotted in Figure 4.10. It can be observed that the gain of FTF_1+FTF_2 fluctuates between n_1+n_2 and n_1-n_2 and the frequencies of the minima and maxima correspond to when the phase difference between FTF_1 and FTF_2 equals odd (destructive) and even (constructive) multiples of π, respectively. In addition, the phase of the summation follows that of FTF_1 that has the larger gain (this also explains the same observation in the FTF phase in Figure 4.8 and Figure 4.9).
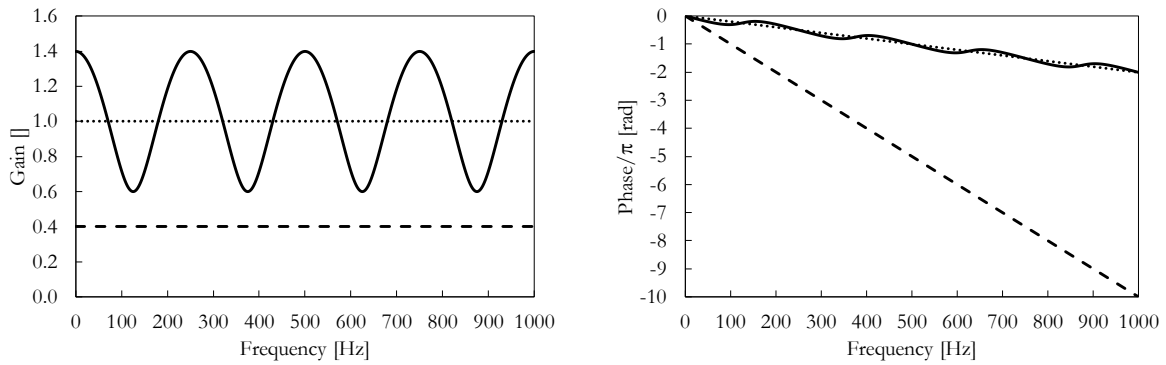
Figure 4.10: Gain and phase of $FTF_1=n_1exp(-i\omega\tau_1)$ *(dotted lines),* $FTF_2=n_2exp(-i\omega\tau_2)$ *(dashed lines) and* FTF_1+FTF_2 *(solid lines), where* $n_1=1$, $n_2=0.4$, $\tau_1=1ms$ *and* $\tau_2=5ms$.

If the FTF gains are also frequency-dependent, more complicated patterns may emerge. For example, if the gain of FTF_1 is linearly decreasing from *1* to *0* at *1000Hz*, it will become smaller than that of FTF_2 for frequencies larger than *600Hz*. This frequency is also where the slope of the phase of FTF_1+FTF_2 changes. In other words, the time delay of FTF_1+FTF_2 follows that of the FTF with the larger gain.
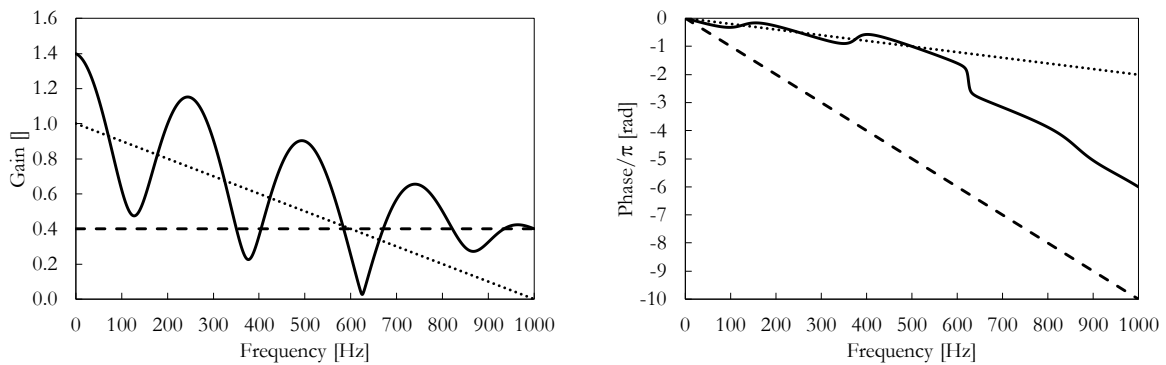
Figure 4.11: Gain and phase of $FTF_1=n_1exp(-i\omega\tau_1)$ *(dotted lines),* $FTF_2=n_2exp(-i\omega\tau_2)$ *(dashed lines) and* FTF_1+FTF_2 *(solid lines), where* $n_1(f)=1-f/1000$, $n_2=0.4$, $\tau_1=1ms$ *and* $\tau_2=5ms$.

A more realistic combination would be the case where the FTFs are normalized and their gains are equal to one at *0Hz* (this is the case for premixed flames due to conservation of energy). In order to see the interference pattern, a virtual overshoot is created for the gain of FTF_2 so that it has a larger gain than FTF_1 for frequencies lower than *300Hz*. The results are plotted in Figure

4.12 and similar trends as in Figure 4.11 are observed. These patterns are also very similar to those observed in combining Cartesian and axisymmetric 2D FTF simulations.
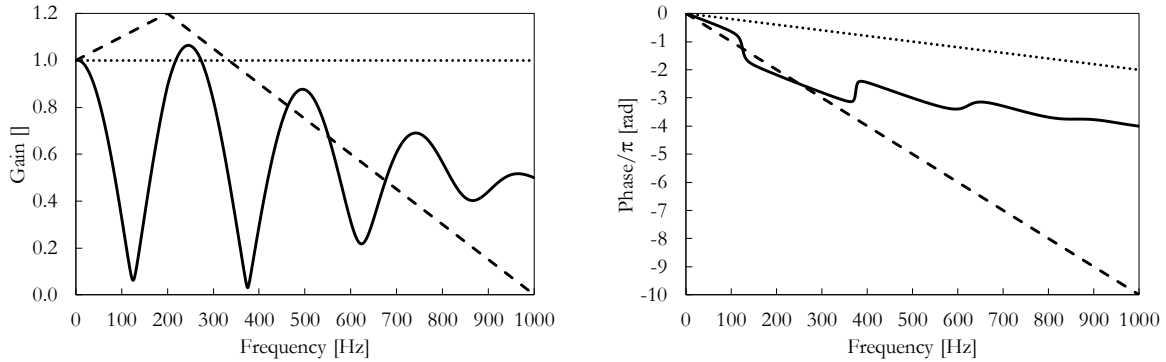
Figure 4.12: Gain and phase of FTF₁=n₁exp(-iωτ₁) (dotted lines), FTF₂=n₂exp(-iωτ₂) (dashed lines) and FTF₁+FTF₂ (solid lines), where n₁=1, n₂(f)=1+f/1000 when f∈[0,200] and n₂(f)=1.5(1-f/1000) when f∈[200,1000], τ₁=1ms and τ₂=5ms.

Effort was made to confirm these findings in measurements, by blocking parts of the flame using plates with specific openings to cover either the two conical caps or the wedge part of the flame. In this way, the photomultiplier tube would only pick up the heat release signal from the uncovered part(s) of the flame. The results are presented in Figure 4.13, where it is immediately visible that the trends captured in measurements are similar to that of simulations. The wedge and conical parts of the flame feature low and high FTF gain fluctuation, respectively, and the full flame FTF gain falls in between these two. The FTF phase of the full flame and wedge part are almost equal and they are both larger than that of the conical part. This observation is in agreement with the comparison with CFD simulations (see Figure 4.9).
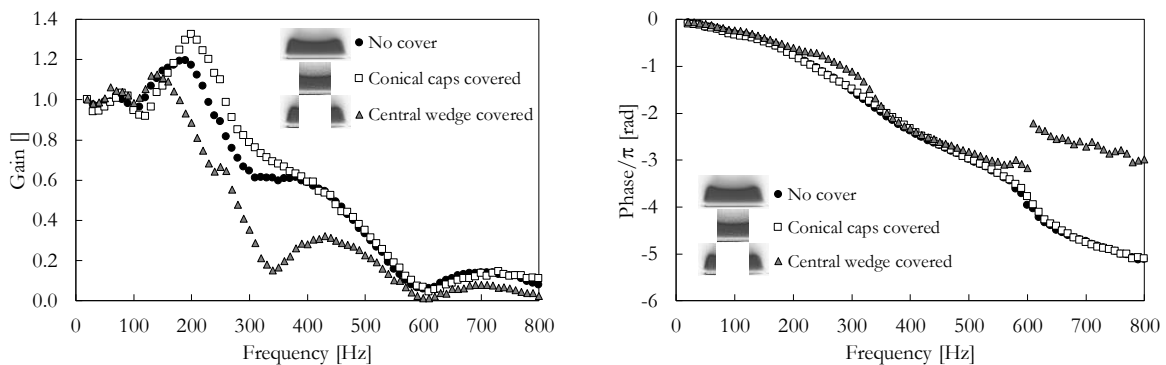
Figure 4.13: FTF measurements for case D2.2-4_P20-0_V1.2_ϕ0.8 using specific plates to cover different parts of the flames.

In general, the fluctuations in FTF gain have been a controversial topic and studied by many researchers. They have mainly attributed these fluctuations to two (or more) phenomena acting simultaneously, but with a phase delay, such as flame bulk motion vs. flame wrinkling [86, 101], flame body heat release vs. flame root heat release [43], and laminar flame speed vs. heat transfer to the flame holder [88, 96]. The findings presented in this section add other possible mechanisms playing a role in such details of laminar premixed FTF. The finer details of these findings are not investigated further here, but it is concluded that the contribution of the conical parts of a slit flame

are not negligible, unless the aspect ratio is extremely large, which is not the case in most industrial applications and previous research studies.

4.1.2 Effects of stabilization temperature

The stabilization mechanism of surface-stabilized laminar flames is mainly governed by the heat loss to the flame holder. This makes the temperature of the burner surface a key factor that affects certain characteristics of the FTF, such as the time delay and gain overshoot [24, 80, 102, 103].

Many lab-scale experimental setups are designed to work with perforated plates in order to enable investigating multiple flames and their possible interactions. Such setups deal with larger heat loads compared to single-flame setups and usually operate with rather high burner temperatures (to enable enough cooling to the ambient environment) or need some measure of dedicated cooling. This cooling is usually implemented in the form of water channels in the burner head, if it is thick enough [50], or in the construction that holds the burner plate [43], in case of thin perforated plates (see Figure 3.4). To make this water-cooling effective, highly conductive materials such as aluminum and brass have been used in many instances in the literature [24, 91, 104, 105]. However, industrial perforated burners are usually made from stainless steel due to price, manufacturing and mechanical reasons. Stainless steel has around one order of magnitude smaller thermal conductivity compared to brass or aluminum that may cause significant temperature distribution on the burner surface and pose inaccuracies in the obtained results based on uniform burner deck temperatures.

4.1.2.1 Temperature profile in burner decks with rectangular perforations

In the presented work, the temperature was measured on multiple locations on the burner deck to capture the temperature distribution (see Figure 3.9). This temperature distribution is presented in Figure 4.14 for the case *D2.2-30_P4-0_V1.2_ϕ0.8*. Note that in all measurements, water-cooling at *22 ℃* was applied around the burner deck between radii *30* and *55mm*. However the temperature on the outer edge of the burner deck (radius *60mm*) was still higher than the water temperature due to the thermal resistances between them (this temperature is not measured, but estimated to be around *100 ℃*). The values reported in Figure 4.14 are obtained at the *9* thermocouple locations marked with round and triangular markers on the centers and ends of the slits, respectively, and are plotted in Figure 4.14b (the contours in Figure 4.14a are created assuming linear interpolation and symmetry). It can be observed that there is a significant radial temperature profile that leads to more than *100 ℃* temperature difference between the center and the two ends of a slit.
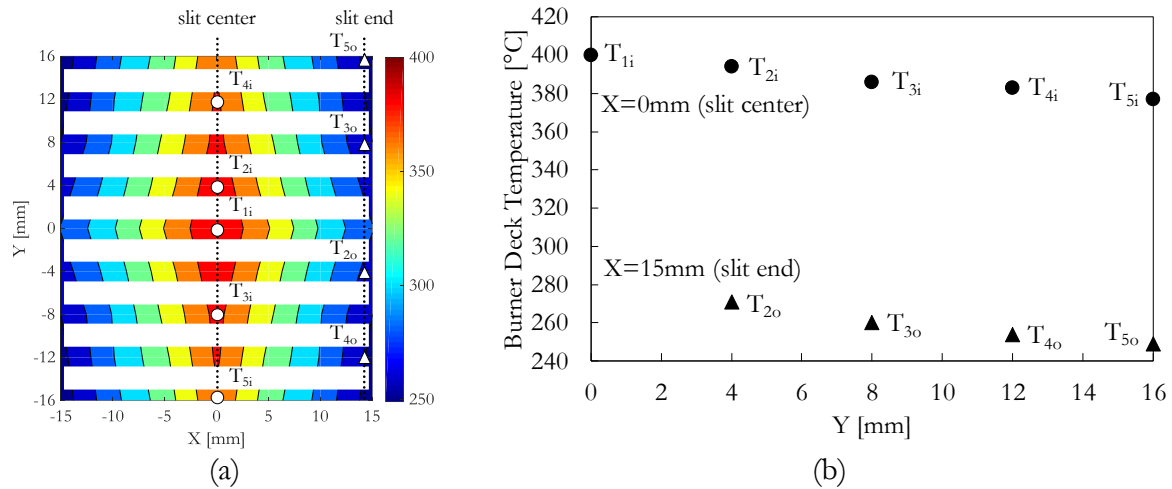
Figure 4.14: Measured temperature distribution on the burner deck for the case D2.2-30_P4-0_V1.2_ϕ0.8. Temperature values are obtained at the 9 thermocouple locations marked with round and triangular markers on the centers and ends of the slits, respectively. The contours are then created assuming linear interpolation and symmetry.

Similar measurements were performed for shorter (*20mm*) and longer (*40mm*) slits in order to investigate the effects of slit aspect ratio on the burner deck temperature profile. For this purpose, the central thermocouple (*T_{1i}*) and the end thermocouple of the last slit (*T_{5o}*) were used as measures of the maximum and minimum temperatures, respectively, and the difference between them was recorded. The results are plotted in Figure 4.15 and show that the burner deck temperature variation increases with increasing slit aspect ratio (note that for these experiments, the number of slits were changed in a way that the total open area, and thus the burner heat load, remained the same, i.e. *12×D2.2-20*, *8×D2.2-30* and *6×D2.2-40*).
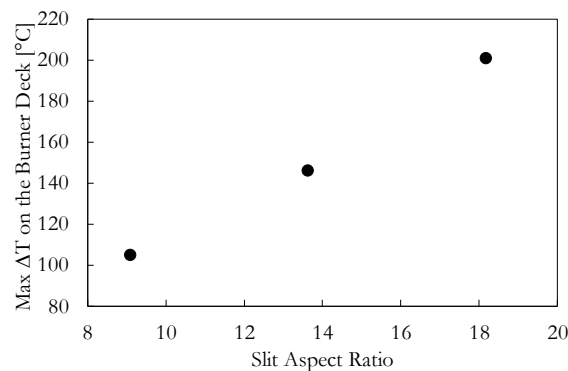
Figure 4.15: The influence of slit aspect ratio on the maximum temperature difference on the burner deck. The investigated cases are burner decks with 12 slits of D2.2-20, 8 slits of D2.2-30, and 6 slits of D2.2-40, and all of them P4-0_V1.2_ϕ0.8.

The observed temperature distributions for the investigated burner decks are intense enough to affect the FTF significantly. Increasing the stabilization surface temperature reduces the gain overshoot and phase delay [43, 50, 80]. Therefore, a burner deck with such an intense temperature distribution is essentially a composition of various flames with different FTFs. However, these flames are attached to each other and this makes them inherently different from a simple sum of separate flames. Therefore, simplified 2D simulations or measurements of bulk heat release from

these flames are not able to capture these local effects. This may be a potential cause of systematic errors in FTF research in such burners.

4.1.2.2   *Temperature profile on burner decks with circular perforations*

In an effort to investigate the possible effects of burner deck temperature distribution on the FTF of conical flames, axisymmetric simulations were performed for circular holes in a rectangular pattern (case *DR4_P10_Rect_V1.2_ϕ0.8*), including an imposed temperature profile that linearly changes with radius. This burner deck was chosen because it had a relatively large perforation diameter and pitch, thus it could be expected that the observed effects were easier to identify. Three cases were investigated, one with the burner deck temperature constant at *300 °C*, and two cases where the temperature radially increases from *273* to *373 °C* and *200* to *570 °C*. Figure 4.16 illustrates the temperature profiles and the flame shapes obtained from reaction heat for these cases. The temperature profiles are chosen such that the burner deck temperature right below the flame root is equal to *300 °C* for all cases. It is observed that the flame shape and standoff distance are hardly affected by the radial temperature distribution (the flame shapes for all the cases are plotted, but the differences are extremely small and can be hardly seen). This can be due to the fact that the temperature right under the flame root is similar for all these cases.
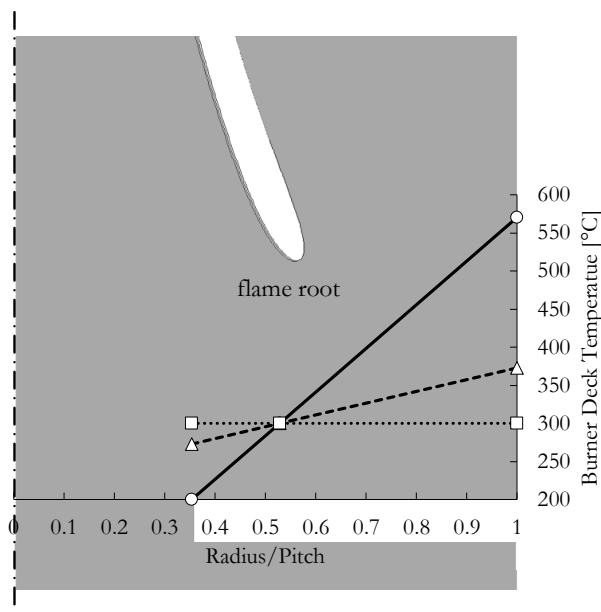
Figure 4.16: Three different burner deck temperature profiles (300 °C constant, 273 to 373 °C, and 200 to 570 °C) and the flame shapes obtained from reaction heat. The flame shapes for all the cases are plotted, but the differences are extremely small and can be hardly seen.

The FTFs for these cases are plotted in Figure 4.17. It can be observed that the flame responses are also very close. The small difference in the gain can be explained by the mean values of burner deck temperature that are slightly different (*300*, *315* and *357 °C*), because the flame root does not stand exactly on the center of the temperature profile.
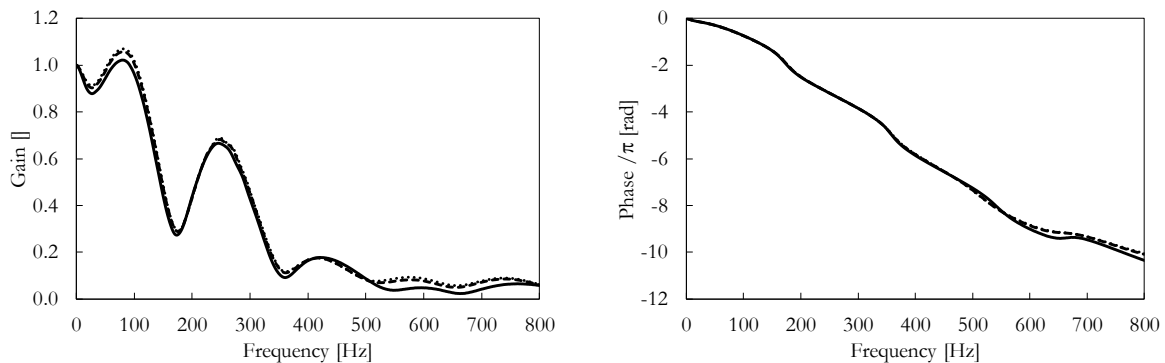
Figure 4.17: The FTFs for three different burner deck temperature profiles (300 °C constant, 273 to 373 °C, and 200 to 570 °C). The small differences in gain are related to the mean deck temperature differences.

The obtained results for conical flames show that their FTFs are not directly affected by the local temperature variations on the stabilization surface. However, in burner decks where perforations are relatively far from each other and the material does not have a high thermal conductivity, the temperature variation on the burner deck intensifies. Therefore, the measured burner deck temperature will be dependent on the placement of the temperature sensor. If it is not placed exactly underneath the flame root, it may record the wrong bulk burner deck temperature. These variations can be observed in industrial burners manufactured to date. For example, the photos in Figure 4.18 (wide angle (a) and close up (b)) are taken from a stainless steel burner manufactured by *Bekaert Combustion Technology B.V.*. It shows the changes in surface color that occur due to oxidation at different temperatures, also known as *"tempering"*. These colors roughly show a temperature distribution that varies multiple tens of degrees Celsius around the perforations [106].
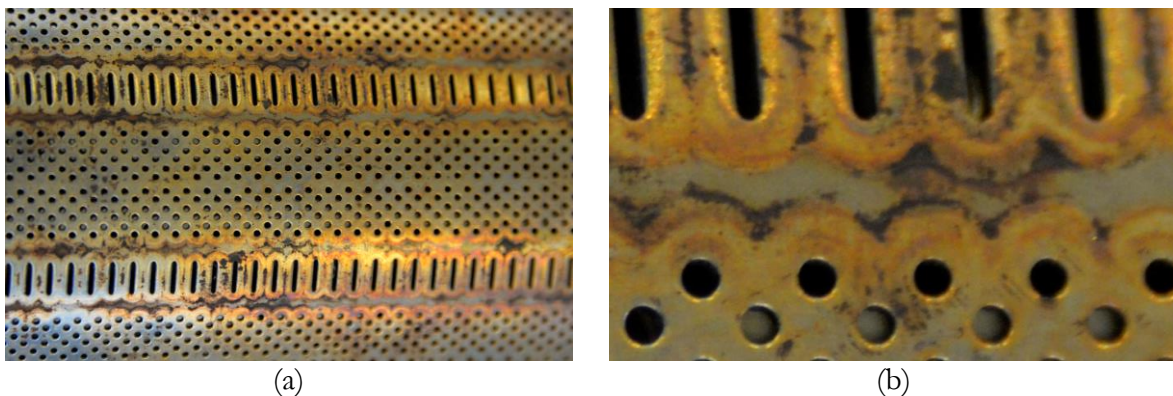
Figure 4.18: Wide angle (a) and close up (b) photos of the surface of an industrial stainless steel burner manufactured by Bekaert Combustion Technology B.V. that shows different tempering colors corresponding to temperatures that vary up to multiple tens of degrees Celsius around the perforations [106].

The presented results show that, in practice, it is of utmost importance to first analyze the burner deck temperature distribution (using proper measurements or steady-state simulations) and then choose a well-thought bulk temperature to be used for transient FTF simulations.

4.2 Transfer function of simplified and realistic heat exchangers

The heat exchanger is a vital part in heating appliances. The recent trends in making compact and efficient heating systems that are able to pass the stringent emission regulations has made the design of the heat exchanger as important as the burner. Most commonly used heat exchangers in heating appliances include variations of material (mainly aluminum or stainless steel) and heat extraction scenario (using narrow channels in a small volume, or routing the flow through multiple sections with extended surfaces in a larger volume). These two dominant industrial heat exchanger designs are introduced in Figure 4.19.

| (a) | (b) |
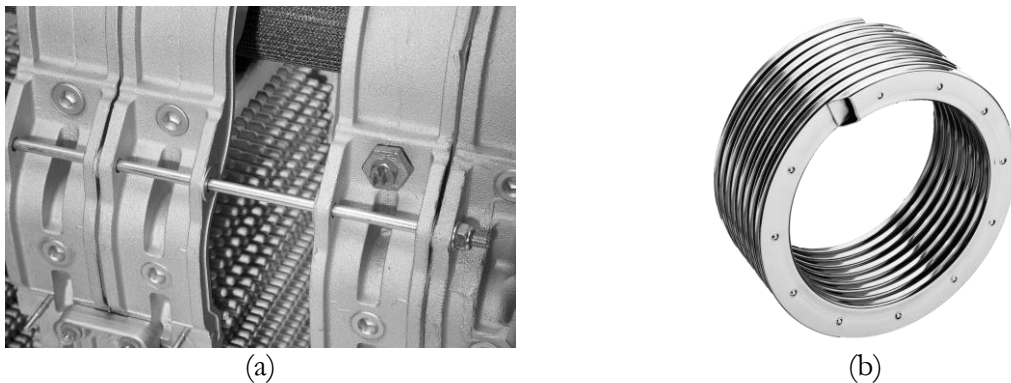
Figure 4.19: (a) An aluminum heat exchanger with multiple pinned sections (image courtesy of Bekaert Combustion Technology B.V.); (b) A helical steel-tube heat exchanger (image courtesy of Viessmann Group).

The heat transfer of a bluff body in cross-flow is one of the typical problems in heat transfer. It is fundamentally and technically relevant to many applications, which has led to a large number of researchers scrutinizing various aspects of this problem [107–109]. Many of these studies focus on enhancing steady-state heat transfer, or look at unsteady effects of flow instability due to vortices or turbulence. The unsteady behavior of heat transfer when the free stream is unsteady (due to, for example, acoustic forcing) has received less attention. Such circumstances are of interest in flow diagnostics using hot-wire anemometry [110–112] (where the frequency response of the wire is important), thermoacoustic heating/cooling engines (where acoustic energy is converted to heating/cooling energy) [113–115] and Rijke tubes [116, 117] (where heating energy is fed into the system acoustics and creates resonance). The latter case is of particular importance in the current work since the unstable behavior of the system is strongly affected by the dynamic response of heat transfer to velocity fluctuations [17].

Lighthill has derived a theoretical framework to describe the response of laminar skin friction and heat transfer to fluctuations in the free-stream velocity [9]. He suggested that the major controlling factor in determining the response is the time needed for the thermal and viscous boundary layers to adapt to the fluctuations in the free-stream velocity. In case of a tube in harmonically fluctuating crossflow, this time lag controls the phase of the TF of the heat exchanger (HTF). For low frequencies, Lighthill estimated this time lag as

$$\tau = 0.2 \frac{D}{U},$$

(4-3)

where τ, D and U denote time lag, tube diameter and free-stream velocity respectively. This estimation has been widely used to date by many thermoacoustic researchers [117–120]. However, the practical need for understanding the unstable heat transfer in industrial systems has motivated using more flexible tools, such as measurements or numerical simulations.

Despite the efforts in performing heat transfer measurements in oscillating flow [121, 122], it is still difficult to measure the heat transfer frequency response with good accuracy and in a broad range of frequencies. This is why CFD simulations have become very common in studying these effects [16, 123, 124] and are also used in the present work.

In the framework of thermoacoustics, several researchers have investigated the frequency response of simplified heat exchangers using either incompressible [125, 126] or compressible [8, 17, 109] CFD and developed semi-analytical models bases on the obtained data [126]. The motivation is that the heat exchanger is also an active thermoacoustic element. Heat exchangers are designed to extract almost all the heat generated due to combustion, in order to provide maximum possible efficiency. This means that they produce temperature jumps as large as the burner. On the other hand, it is well-known that an acoustically forced flow may create a fluctuating heat flux on the bodies in the flow [9, 17]. Therefore, the heat exchanger may be an additional active acoustic element next to the burner in the acoustic network that needs to be studied both separately and in combination with the burner. The former is addressed in this section and the latter in Chapter 5. The modeling and analysis is similar to that presented in a joint effort with Keele University [126].

4.2.1   Single-element and multiple-element heat exchangers

The simplified geometries of the major heat exchanger designs are presented in Figure 4.20. First, two single-element heat exchangers with rectangular and circular tubes are considered. Then three more heat exchangers with *4*, *7* and *10* staggered circular tubes are studied. The heat exchanger with multiple circular tubes and the rectangular tube are meant to mimic the effects of the two major heat exchanger designs presented in Figure 4.19a and b, respectively.
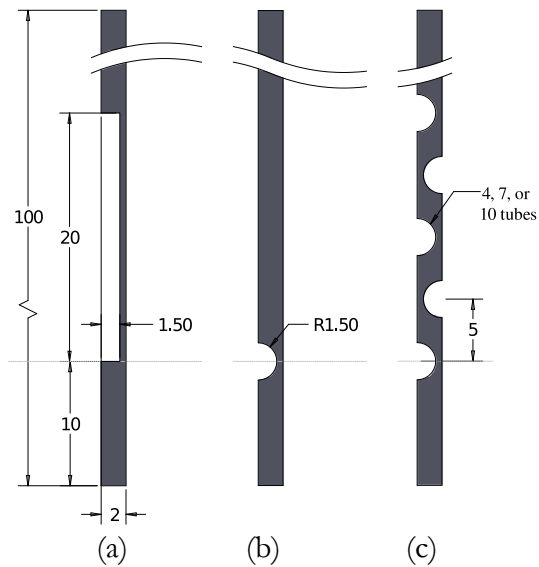
Figure 4.20: The simplified geometries of the major heat exchanger designs presented in Figure 4.19. (a) Single-element rectangular-tube heat exchanger; (b) Single-element circular-tube heat exchanger; (c) Multiple-element (4, 7, and 10) circular-tube heat exchanger.

The simulation setup and solution procedure was as explained in section 3.4.1 *"CFD simulations of transfer functions"*. The domain was considered symmetric on both sides and the incoming flow had the same characteristics (composition, temperature and bulk velocity) as the post-combustion stream. The heat transfer through the heat exchanger walls and inside the water flow was assumed to be large enough so that the heat exchanger surface had a constant temperature. This temperature was set to *70°C*, which was obtained from measurements on a similar simplified setup (see further at Figure 5.1a). This causes a difference in the efficiency of the heat exchangers, i.e. the outlet temperature is not the same for all cases. It was *289, 1124, 412, 116* and *92°C* for the rectangular, 1-tube, 4-tube, 7-tube and 10-tube heat exchanger. The HTF was calculated as the response of the heat absorption of the heat exchanger (the integral of heat flux on all its surfaces) to a step increase in the incoming flow velocity. The results of this calculation are presented in the following section.

4.2.2   Effects of tube geometry, inlet flow velocity and using multiple tubes

Figure 4.21 illustrates the HTF for the long rectangular-tube and circular-tube heat exchangers, corresponding to Figure 4.20a and b, respectively. Here, the inlet velocity is set to *5.5m/s* that corresponds to an average post-flame bulk velocity obtained from the burner simulations. It can be observed that both the gain and phase delay of the rectangular heat exchanger is larger. This is because the thermal boundary layer of the rectangular heat exchanger is much further developed compared to that of the single circular tube. These results have also been reported in the literature for similar geometries [7, 8, 127].
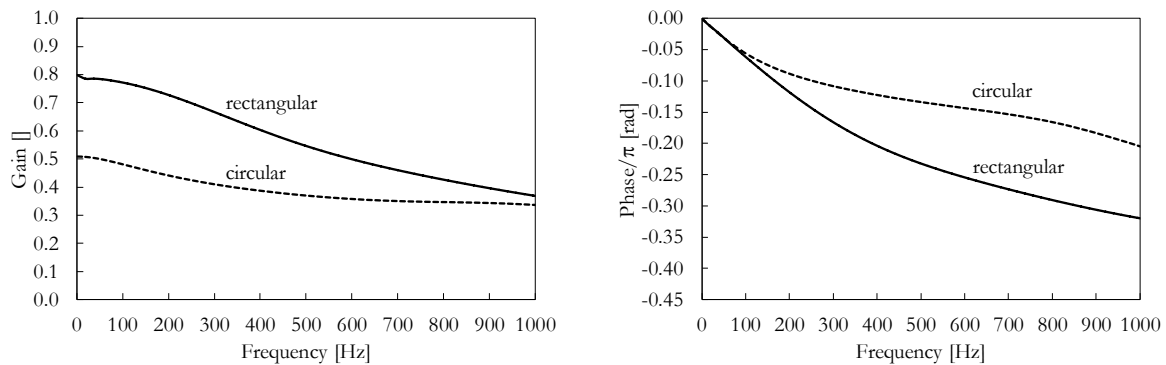
Figure 4.21: Gain and phase of HTF for the single rectangular-tube and circular-tube heat exchanger.

For the rest of this section, we focus on the circular-tube heat exchanger. Figure 4.22 shows the gain and phase of HTF of a single circular-tube heat exchanger for varying inlet flow velocity from *1* to *6m/s*. It is visible that increasing the inlet velocity decreases the slope of phase (time delay), which is expected based on Lighthill's theory (see Equation (4-3)). It occurs because the thicknesses of the thermal and viscous boundary layers reduce by increasing free-stream velocity. The phase also saturates at high frequencies that is a typical behavior of first-order systems. This saturation results in decreasing slope of phase, and thus time delay, with increasing the excitation frequency. For the HTF gain however, the changes by changing flow velocity are twofold, i.e. it decreases for frequencies below *300Hz*, while it increases for frequencies above *300Hz*. In addition, the HTF gain drops more rapidly with frequency for lower flow velocities. In other words, larger flow velocities lead to a less intense low-pass behavior of HTF gain. The reduction of HTF gain in the limit of low frequencies is also explainable by looking at the relation between the mean heat transfer rate and flow velocity. The Nusselt number changes as a power function of Reynolds number with the power value smaller than one, based on the empirical correlation of Hilpert [107]. This means that the slope of the changes of heat transfer rate is larger for smaller velocities, resulting in a larger heat transfer fluctuation amplitude when the mean flow is smaller. This is identical to larger quasi-steady HTF gain for smaller flow velocities.
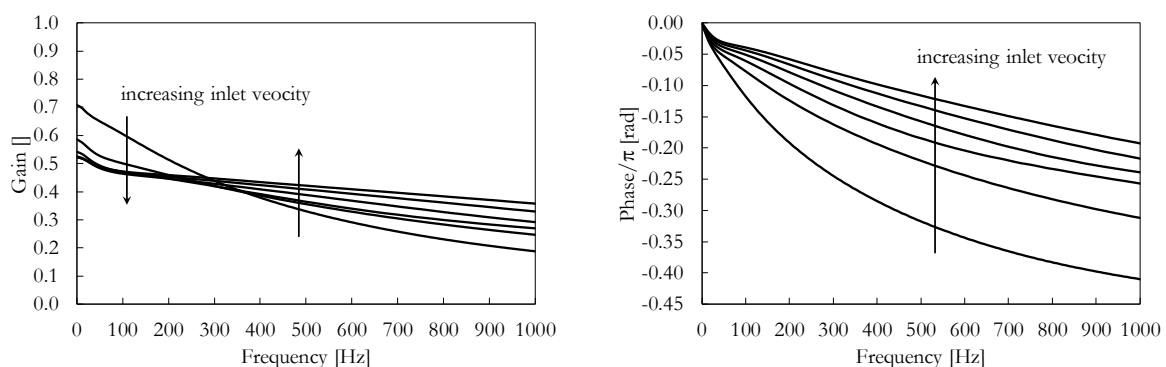
Figure 4.22: the gain and phase of HTF as a functions of frequency for a single circular-tube heat exchanger with varying inlet flow velocity from 1 to 6m/s.

For these cases, it is also comfortable and informative to look at the HTF as a function of Strouhal number rather than frequency. For this purpose, the Strouhal number is defined as

$$St = \frac{fD}{U},\tag{4-4}$$

where f, D, and U denote the frequency, tube diameter, and bulk inlet flow velocity, respectively. The results are plotted in Figure 4.23. Now the gain is monotonically decreasing and going to saturation by increasing velocity, but the phase behavior has become twofold. Nevertheless, the phase plots are close to each other.
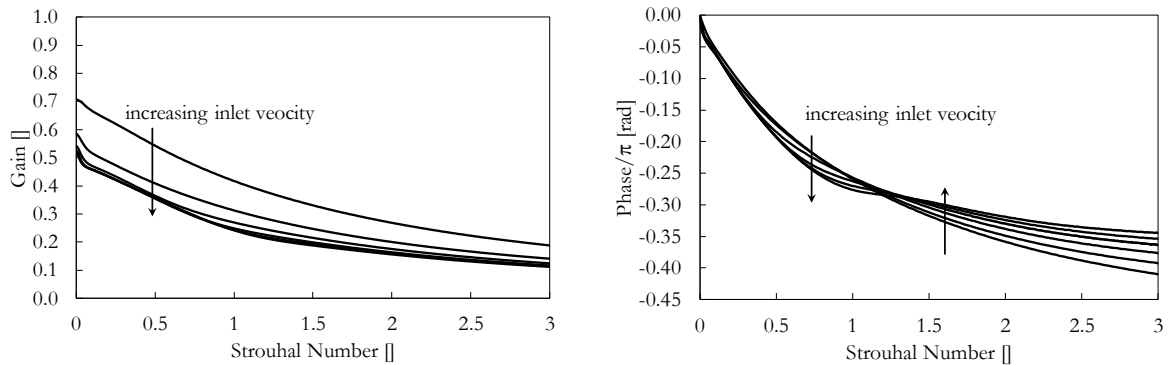
Figure 4.23: Gain and phase of HTF as a function of Strouhal number for a single circular-tube heat exchanger with varying inlet flow velocity from 1 to 6m/s.

The last case involves using multiple staggered round tubes as depicted in Figure 4.20c. Four cases with *1*, *4*, *7*, and *10* heat exchanger tubes are considered and the obtained HTFs are plotted in Figure 4.24. It can be observed that both the gain and phase of HTF saturate by increasing the number of tubes and further increase does not considerably change the HTF behavior. This finding can be useful in defining the HTF of large heat exchangers featuring a large number of pins. In principle, the HTF of such a heat exchanger is mainly defined by the first few row of pins, where most f the heat transfer occurs.
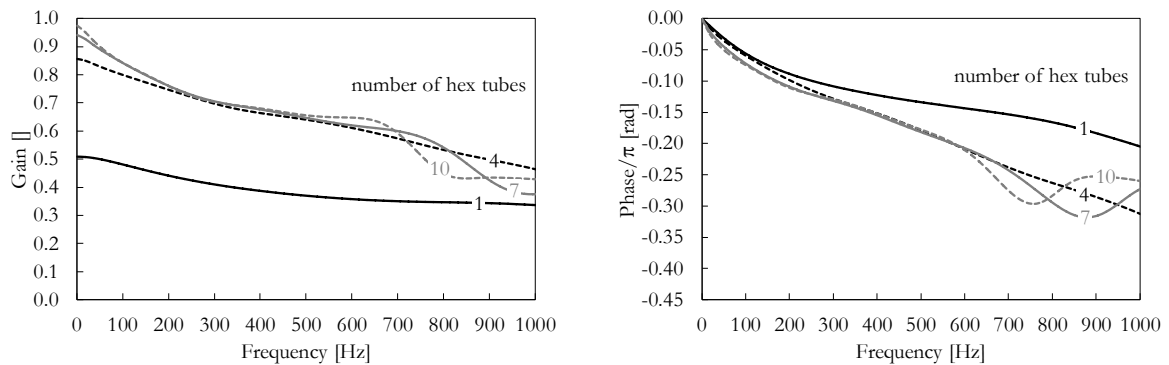
Figure 4.24: The gain and phase of HTF for multiple circular-tube heat exchangers with 1, 4, 7, and 10 staggered tubes.

The response of the heat exchanger to velocity perturbations is much simpler than that of the burner. The gain decays gradually with frequency and no overshoot is observed. The phase also increases gradually with frequency, but saturates around $\pi/2$ at very high frequencies. Nevertheless, for relatively large flow velocities, which are expected in the post-combustion region, the slope of

the phase is almost constant in the *1kHz* frequency range of interest. This makes the *n-τ* model an ideal method for modelling the thermoacoustic response of the heat exchanger.

4.3 Conclusions

The responses of the burner and heat exchanger to velocity perturbations were studied considering them as two independent active acoustic elements. Investigating details of flame front structure and stabilization conditions revealed that the total heat release response of the burner is a result of various parameters acting together and these parameters should be addressed in order to provide a good assessment of the burner TF. Evaluating the heat exchanger TF for a few case studies that correspond to realistic industrial designs showed a range of gain and phase values that can be expected. The heat exchanger TF has generally smaller gain and phase compared to the burner, however the decay rate of the gain is slower. TF gain and time delay are the two major parameters that are used in evaluating the stability of a system including the burner and heat exchanger. The time delay of the heat exchanger is also considerably smaller than that of the burner.

The question now is how the combination of the burner and heat exchanger reacts to acoustic perturbations, and how we can reconstruct the behavior of the complete system using the burner and heat exchanger separate responses. These challenges are addressed in the following chapter.

CHAPTER 5

Thermoacoustic Properties of a Heating Appliance with Active Burner and Heat Exchanger

The thermoacoustic properties of the burner and heat exchanger as separate elements are evaluated in Chapter 4. In this chapter, the thermoacoustic properties of a combination of these two in a typical heating appliance configuration are investigated. The focus of this investigation is to identify and decouple the effects of the burner and heat exchanger on the thermoacoustic properties of the complete system. This chapter has been published in *Combustion and Flame* [125] and is a reprint of the published manuscript. Consequently, some overlap may be expected between the introductory sections of this chapter and the first three chapters of this thesis.

5.1 Introduction

Thermoacoustic instabilities are frequently present in lean (partially) premixed combustion and have been studied for more than a century [1, 128, 129]. Such instabilities may occur in various systems, such as gas turbines, boilers and other heating systems. Many of combustion appliances include not only heat sources (burners) but also heat sinks (heat exchangers). In the combustion thermoacoustic research, the common practice is to treat the burner as the solely active thermoacoustic element and the other components as passive elements (such as ducts, vessels and terminations, including heat exchangers) [4]. One of the crucial prerequisites of this modular

method is the possibility to distinguish and separate the "acoustic elements" from each other, and accordingly to encapsulate their acoustic behavior as a property of the given element only. This paradigm is the basis of the network model approach, where the subsystems are described as linear elements with two acoustic inputs and two outputs (two-ports), interrelated via a Transfer Matrix (*TM*) or a Scattering Matrix (*SM*). The heat release response to acoustic excitation of velocity in an active element, like burner, can be naturally described within the concept of the thermoacoustic Transfer Function (*TF*). For acoustically compact elements (where the size of the element is negligible compared to the acoustic wavelength), the *TM* is related to the *TF* through the heat release rate [36, 130]. There are multiple examples in the literature, where this approach has proven to be productive in predicting system instabilities and evaluating different measures of passive and/or active control [131–134].

On the system level, the heat exchanger is designed to absorb most of the heat produced by the burner and create a reverse temperature jump of the same order of magnitude as the burner. On the other hand, it is well known that an acoustically forced flow may create a fluctuating heat flux on the bodies in the flow [9, 10]. Therefore, the heat exchanger may potentially be an additional active acoustic element next to the burner in the acoustic network. The activity of a heat exchanger can be included in the acoustic network analysis. As an example, the authors have demonstrated in an earlier publication that in a simple one-dimensional Rijke burner with a flame and heat exchanger, the thermoacoustic properties of the heat exchanger can significantly alter the stability of the system [6]. However, the aforementioned study has been purely acoustic and considered approximated and frequency-independent transfer functions for the burner and heat exchanger, neglecting any direct interactions.

On the other hand, the practical need to reduce the built volume of combustion appliances and minimize nitrogen oxides, leads to the desire to locate the heat exchanger very close to the burner. The smaller this distance, the more questionable it becomes to consider the burner and the heat exchanger as two acoustically independent elements. It is known that in the limit case of impinging flames, the intense interaction of a flame with a heat exchanger leads to significant changes of the acoustic properties of the flame. Particularly, it was observed that impingement may change the noise produced by the flame [11–13]. Similarly, the proximity of a flame to the heat exchanger surface can affect the periodic heat transfer between the surface and hot gases. In other words, the fluctuations induced by the flame dynamics may alter the acoustic properties of the heat exchanger. Consequently, the thermoacoustic properties (e.g. *TF* and *TM*) of the combination of the burner and heat exchanger may differ drastically from when considered independent. Therefore, one may a-priori expect that the mutual interactions between the burner and the heat exchanger may alter their individual thermoacoustic properties. Consequently, the direct interactions (hydrodynamic, heat transfer and chemical reactions) will impose a range of implications for the acoustic network modeling of a combustion system with interacting burner and heat exchanger.

The practical relevance, fundamental interest and shortage of knowledge about the burner-heat-exchanger thermoacoustic interactions has stimulated the present work. The ultimate goal of this investigation is to elucidate the physical nature of burner-heat-exchanger interactions in respect to their thermoacoustic behavior. Particularly, the aim is to answer the following questions:

- What are the conditions for considering the combined *TF/TM* of the burner and heat exchanger as the superposition of their individual *TF/TMs*, and how can this be done properly?
- When do the interactions between them affect the individual *TF/TMs*, and what is an applicable method to reconstruct a combined *TF/TM*?
- What are the physical phenomena and governing parameters responsible for these interactions?

To solve the formulated problem and questions, a particular configuration is studied that consists of a bed of idealized Bunsen-type wedge shaped (two-dimensional) premixed flames anchored on slit perforations in a burner deck, and interacting with a heat exchanger consisting of a series of idealized cylindrical tubes placed downstream of the burner (see Figure 5.1). This academic configuration is representative for the design of a majority of heating appliances and is composed of relatively simple elements which have been intensively studied in the past on theoretical, experimental and numerical levels [10, 18–20].

CFD is chosen as the research tool because there are no convenient and easily measurable indicators for the oscillating rate of heat transfer from the hot gases to the heat exchanger (unlike the chemiluminescence of chemical radicals for flame heat release). Consequently, within a physical experiment, it is feasible to evaluate the effects of the heat exchanger on the acoustic properties of the flame, but it is difficult to detect the reciprocal effects of the flame on the heat exchanger. This fact motivates the use of the CFD-based analysis within the present work.

By changing the distance between the burner and heat exchanger, one can alter the intensity of the mutual interactions. For large distances, no hydrodynamic interaction is expected. However, as the distance decreases the hydrodynamic and thermal fields created by the flame and heat exchanger begin to interact. These interactions can be extremely intense and complicated when the flame impinges on the heat exchanger surface. Details of the situations that may occur are discussed in the following section.

Ultimately, by studying this simplified configuration, general conclusions are formulated regarding the physics of the processes responsible for the interactions, considering the thermoacoustic aspects of this problem. The drawn conclusions are generic by nature and can be applicable to other configurations as well.

5.2 Governing phenomena of the interactions between a burner and a downstream-placed heat exchanger

A picture of the constructed burner-heat-exchanger system and a schematic of the simplified configuration used as the simulation geometry are illustrated in Figure 5.1. Symmetry has been used in order to reduce the size of the computational domain and to model the effects of the neighboring flames and heat exchanger tubes. The mixture enters from the inlet at the bottom and the flames stabilize on the slit perforations. The combustion products flow towards the heat exchanger tubes and leave the domain at the outlet. In addition to the dimensions mentioned in Figure 5.1, other

important length scales are flame height ($L\approx5mm$), flame thickness ($\delta\approx0.5mm$) and the smallest acoustic wavelength ($\lambda\approx1370mm$), which is calculated for a maximum temperature of *2000K* and highest relevant frequency of *1000Hz*.

(a)   (b)
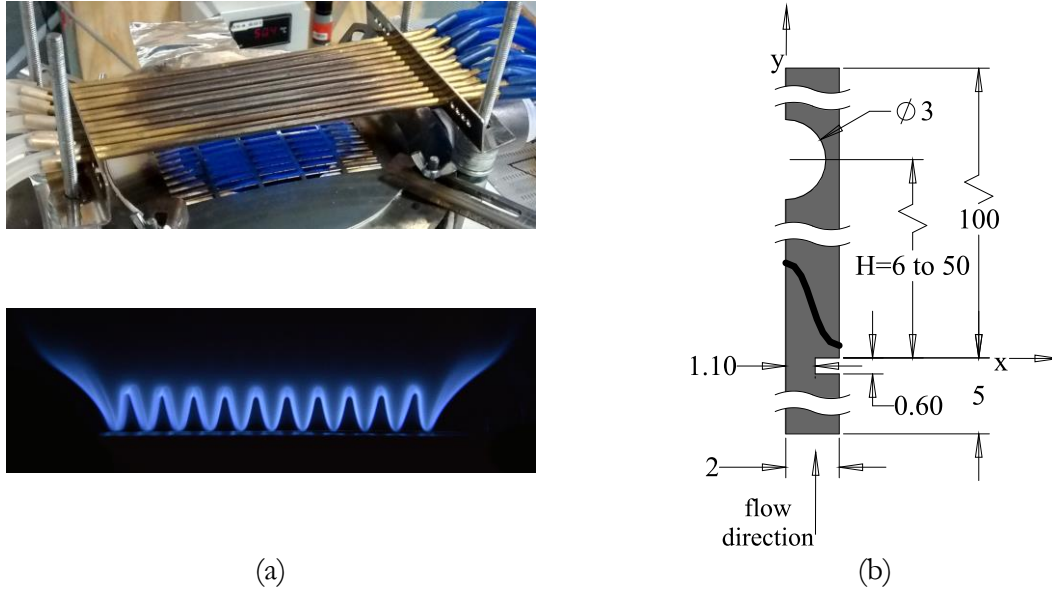
Figure 5.1: A picture of the constructed burner-heat-exchanger system (a) and the geometry and dimensions (mm) of the simulation domain, the flow direction and typical flame shape (b).

A priori, for a heating appliance containing a burner and heat exchanger and in presence of acoustic perturbations, one can foresee several hypothetical interaction scenarios between the two elements. These interactions are mainly governed by the distance between them and are illustrated in Figure 5.2. This figure shows the flow streamlines and the flame shape. In the limit case where the distance is sufficiently large to smoothen all non-uniformities (thermal, kinetic and fluid dynamic), the heat exchanger is exposed to a uniform flow of burned gases with the acoustic perturbations on top of the mean flow (see Figure 5.2a). In this case, the subsystems can be treated separately from the point of view of either convective fluid dynamics or acoustics. In this case, there are no difficulties to define spatial boundaries as inlets and outlets for the burner and the heat exchanger as the succeeding element. Usually these boundaries are defined where acoustic waves can be considered one-dimensional and planar. It can even be necessary and reasonable to include some extra acoustic elements, such as ducts, to model the propagation of acoustic waves between the burner and the heat exchanger [8].

At some level of proximity between the subsystems, either the convective or the acoustic perturbations do not smoothen to a negligible level (see Figure 5.2b). In this case, the thermoacoustic behavior of the heat exchanger may be affected due to the deviations of the incoming fluid field. This is the situation where the properties of the flame are not yet affected by the heat exchanger, but the acoustic properties of the heat exchanger are affected by the proximity of the flame. In general, the convective and acoustic "near-fields" of the excited flame do not have to be spatially the same. Consequently, within this one-way interaction scenario some sub-cases can be foreseen based on the intensity of the effects of the burner on the heat exchanger.

Furthermore, the existence of an acoustically well-defined interface between the burner and heat exchanger is questionable.

Finally, when the heat exchanger is so close to the burner that the mean flame shape is affected, mutual thermoacoustic interactions are expected (see Figure 5.2c). Here, the subsystems may no longer be acoustically separated and should be considered as one combined element with common inlet and outlet interfaces.
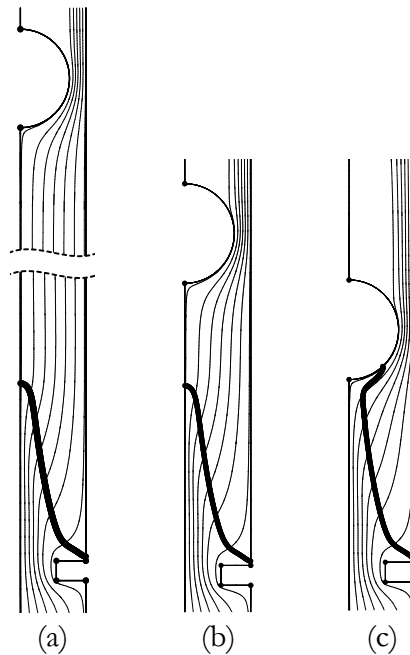
Figure 5.2: The flow streamlines and flame shapes for various conditions of interaction between the burner and heat exchanger, i.e. flame and heat exchanger unaffected (a), flame unaffected and heat exchanger affected (b) and both flame and heat exchanger affected (c).

Within the present contribution, the above-described scenarios are studied in the presented setup. First, the numerical setup is introduced concisely together with brief information about model validation. More details on the model and its validation approach can be found in a previous publication [135]. Next, the thermoacoustic properties of the burner and heat exchanger, and their combined *TFs* and *TMs* are studied as functions of the distance between the burner surface and the heat exchanger. This is the core analysis, which is meant to reveal the changes of the interaction scenarios. The observed interactions are then analyzed in the discussion section, and in conclusions, the generic features of the interactions between the burner and the heat exchanger are retrieved based on the obtained results.

5.3 Numerical setup

The simulation domain is presented in Figure 5.1b. The inlet boundary is set to constant velocity of *0.8m/s*, the outlet boundary to atmospheric pressure and the lateral boundaries to symmetric. Some studies have suggested using a correction factor for flame expansion effects [54]. However, these effects marginally alter the flame *TF* and do not change the nature of the interactions and the conclusions to be drawn. The burner deck and heat exchanger have isothermal boundaries set to

793 and *343K*, respectively, obtained from corresponding measurements, where the walls are thin and the constant temperature assumption is acceptable. Nevertheless, if a more accurate and detailed investigation is required, conjugate heat transfer needs to be taken into account. The grid size is *160μm*, which is refined to *40* and *20μm* around the heat exchanger and flame, respectively, in order to resolve the thermal boundary layers and flame thickness properly.

The flow is assumed laminar and the fluid an incompressible ideal gas, due to low Reynolds and Mach numbers. The mixture is methane-air with the equivalence ratio of *0.8* and combustion is modeled using the finite rate chemistry for a 2-step reaction mechanism as described in [53]. The available Arrhenius rates are modified to match the flame speed and thickness to the available experimental data (see the section *"5.4 Validation"*). The specific heats of all individual species are obtained from temperature-dependent polynomials and their viscosities and thermal conductivities using kinetic theory. The corresponding properties of the mixture are then available using the mixing law. The software package used for this work is *ANSYS® Fluent 17.0*.

The transfer function concept is widely used to characterize the thermoacoustic properties of active elements driven by acoustic velocity in the linear regime. In the frequency domain, the frequency-dependent *TF* is defined as the ratio of the relative perturbation of heat release or absorption, to the relative perturbation of flow velocity,

$$TF(f) = \frac{q'(f)/\overline{q}}{u'(f)/\overline{u}}, \tag{5-1}$$

where *q* is the heat release or absorption, *u* the flow velocity and *f* the frequency of the perturbation. The prime and overbar denote the fluctuating and mean parts of the variables, respectively.

A purely acoustical concept to characterize the thermoacoustic properties of an element is the transfer matrix, in which part of the system is considered as a lumped acoustic element. This approach is most suitable to describe longitudinal acoustic waves in the linear regime of oscillations [1]. The input vector of acoustic variables can be related to the output vector via the transfer matrix,

$$\begin{bmatrix} p' \\ u' \end{bmatrix}_{downstream} = TM(f) \begin{bmatrix} p' \\ u' \end{bmatrix}_{upstream} \text{ and } TM(f) = \begin{bmatrix} M_{pp}(f) & M_{pu}(f) \\ M_{up}(f) & M_{uu}(f) \end{bmatrix}, \tag{5-2}$$

where p' and u' denote the acoustic pressure and velocity, respectively. It is known that for an acoustically compact element in the limit of low Mach numbers, M_{uu} is the only entry that is sensitive to the presence of an oscillating heat source or sink [43, 54, 63]. This entry relates the acoustic components of the velocity downstream and upstream of an element, where the acoustic fields are planar. For the sake of simplicity, the TM_{22} entry of the transfer matrix (M_{uu}) is referred to as *TM* in this chapter. The relation between *TF* and *TM* can be derived from the Rankine-Hugoniot jump conditions [136] and shows their linear proportionality,

$$TM = 1 + (\theta - 1)TF, \tag{5-3}$$

where θ is the ratio of downstream to upstream temperatures in Kelvins.

In order to obtain the burner and heat exchanger *TF* or *TM*, transient simulations are performed to calculate their responses to a block change in velocity. This is done by imposing a step function with *5%* increase in the inlet velocity as excitation. The response of the burner and heat exchanger

are then calculated using the volume integral of reaction source term and the surface integral of heat flux through the heat exchanger wall, respectively. It is particularly checked that the time step size (*10μs*) is small enough to capture the premixed flame dynamics. It is also checked that the perturbations are small enough to prevent nonlinearities and can be regarded as a broadband excitation covering a wide range of frequencies. This approach has proven to be efficient and representative of obtaining the system response using discrete harmonic excitations [55]. The responses of the system and its elements are then calculated both with the transfer function and transfer matrix approaches, according to Figure 5.3 and Table 5.1.

In Figure 5.3, a schematic of the system as a network model is shown, where *u* and *q* denote velocity and heat release/absorption, respectively. Note that the reference point for calculating *TF* of a specific element is usually chosen at a distance upstream of the element, where the acoustic waves can be assumed planar. Consequently, for the burner, the combined effects of the flame and flame holder are measured or simulated.

Figure 5.3: A schematic of the network model for the total system showing the excitation and response signals.

Figure 5.4 shows how the burner heat release and heat exchanger heat absorption change with time as the velocity excitation is applied. This data is for a case where the heat exchanger is placed far from the burner (see Figure 5.2a).
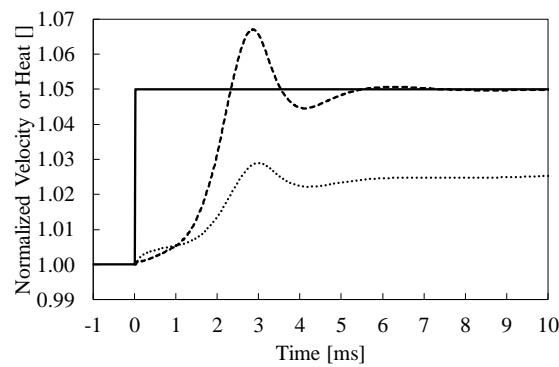
Figure 5.4: Normalized time signals of the inlet velocity (——), burner heat release (— — —) and heat exchanger heat absorption (······). The normalization is performed with respect to corresponding values before excitation.

Table 5.1 summarizes the corresponding excitation and response signals used for calculating the *TF* and *TM* of each element and the combined system.

Table 5.1: The excitation and response signals for calculating the TF and TM of the elements and total system.

Parameter	Excitation	Response	Parameter	Excitation	Response
TF_{burner}	u_{in}	q_{burner}	TM_{burner}	u_{in}	u_{mid}
TF_{hex}	u_{mid}	q_{hex}	TM_{hex}	u_{mid}	u_{out}
TF_{total}	u_{in}	$q_{burner} - q_{hex}$	TM_{total}	u_{in}	u_{out}

5.4 Validation

The modified reaction parameters are first used in a one-dimensional configuration to find the grid size required to capture the flame thickness and laminar flame speed accurately, as well as their dependency on the equivalence ratio and unburned temperature. The obtained data are in good agreement with the literature [58, 60, 137]. In addition, the validation of the *TF* of the two-dimensional stretched flame is performed in comparison with the work of Kornilov et al. [24]. They have provided measurement and DNS simulation results of wedge flames stabilized on a perforated deck. This work is chosen because the configuration is close to our study and their results are confirmed in other independent studies as well [54]. The comparison of the *TF* gain and phase is presented in Figure 5.5. This comparison also provides a double check for the laminar flame speed and flame height, since these parameters significantly affect the burner *TF* [24, 54, 63]. The results show that the model is able to reproduce the experimental and numerical data from the literature with good agreement.
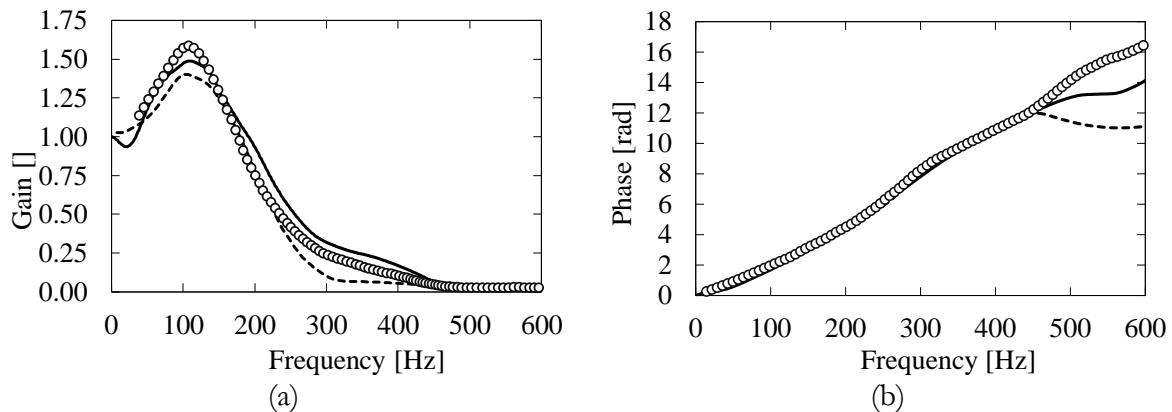
Figure 5.5: The gain (a) and phase (b) of the burner TF for the experiments from [24] (○)*, simulations from* [24] (‑ ‑ ‑) *and this study* (——)*.*

5.5 Results and discussion

The results are categorized in two parts. First, the case where the heat exchanger is placed far downstream of the burner is investigated. Here the sensitivity of the location of the chosen section for decoupling the burner and heat exchanger is studied. Afterwards, various situations that occur when the physical distance between the flame and heat exchanger decreases are discussed.

5.5.1 The heat exchanger far downstream of the burner (at *Y=50mm*)

As can be noticed in Figure 5.2, the flow accelerates across the flame due to the temperature increase. Since the configuration is confined, a velocity profile downstream of the flame is formed which is not flat (not constant in x-direction). The required distance from the burner so that this velocity profile is flat with a maximum deviation of *1%* is defined by *Y=0.05.Re′.s*, where *s* is the pitch between the slits (*4mm* in Figure 5.1b) and *Re′* is the Reynolds number (based on the velocity

downstream of the slits and two times the pitch) [138]. This minimum length is calculated equal to *30mm (6L)* for the geometry and conditions under investigation. This location (*Y=30mm*) is *20mm (>6D)* upstream of the heat exchanger tube, which is far enough for the flow not to be affected by the contraction between the tubes. Therefore, this location is chosen as a mid-section for splitting the system into the burner and heat exchanger subsystems, when they are far from each other. Figure 5.6 shows a schematic of the splitting section and related dimensions.

Figure 5.6: Schematic of the split and related dimensions (mm).

The Helmholtz number is described as *He=2πl/λ*, where *l* is the corresponding length and *λ* is the acoustic wavelength [39]. For *30mm* length and the smallest acoustic wavelength of *λ=1370mm* (see section *"5.2 Governing phenomena of the interactions between a burner and a downstream-placed heat exchanger"*), the Helmholtz number is less than *0.14*. This shows that the subsystems after splitting are still acoustically compact.

The total *TF* can be calculated theoretically using the energy balance in the system and it is not simply the sum or a weighted sum of the burner and heat exchanger *TFs*. Assuming linearity of the system and using the heat balance we have,

$$q_{total} = q_{burner} - q_{hex} \Rightarrow \begin{cases} \overline{q}_{total} = \overline{q}_{burner} - \overline{q}_{hex} \\ q'_{total} = q'_{burner} - q'_{hex} \end{cases}. \tag{5-4}$$

Based on the definition of *TF* and some algebraic manipulations we can calculate,

$$TF_{total} = \left(\frac{\overline{q}_{burner}}{\overline{q}_{total}} \right) TF_{burner} - \left(\frac{\overline{q}_{hex}}{\overline{q}_{total}} \right) TF_{hex} TF_{u_{mid} - u_{in}}. \tag{5-5}$$

Here $TF_{u_{mid} - u_{in}}$ is a velocity-to-velocity transfer function between the inlet velocity and the velocity downstream of the flame (upstream of the heat exchanger). It can be related to burner *TM* using the velocity ratio u_{in}/u_{mid}. This ratio is equal to *1/θ* for an incompressible ideal gas. Therefore, using Equation (5-3) we have,

$$TF_{u_{mid}-u_{in}} = \left(\frac{\overline{u}_{in}}{\overline{u}_{mid}}\right)TM_{burner} = \left(\frac{1}{\theta}\right)\left(1+(\theta-1)TF_{burner}\right) = \frac{1}{\theta}+\frac{\theta-1}{\theta}TF_{burner},$$ (5-6)

so that we have,

$$TF_{total} = \left(\frac{\overline{q}_{flame}}{\overline{q}_{total}}\right)TF_{burner} - \left(\frac{\overline{q}_{hex}}{\overline{q}_{total}}\right)TF_{hex}\left(\frac{1}{\theta}+\frac{\theta-1}{\theta}TF_{burner}\right).$$ (5-7)

Figure 5.7 illustrates the gain and phase of the *TF* of the burner, heat exchanger and total system using both the CFD results and Equation (5-7). Here, the heat exchanger *TF* is calculated using the velocity fluctuations at the splitting section. The gain of the burner *TF* has an overshoot at *300Hz* that is due to the coupling of periodic heat transfer to the burner deck with the velocity fluctuations [18]. The *TF* phase change of the burner is much larger than that of the heat exchanger and therefore the total system time delay is almost identical to that of the burner. The gain of the heat exchanger *TF* is below unity for all frequencies, i.e. the relative amplitude of fluctuations of the heat flux through the heat exchanger is smaller than that of the excitation. This is a usual trend in bluff bodies exposed to oscillating cross flow [9, 10]. Since the heat exchanger is a sink of heat, this causes the relative amplitude of fluctuations of the total heat of the whole system to be larger than that of the excitation, resulting in larger gain for the total *TF*. This causality can be understood by considering harmonic fluctuations with DC and AC components of the signal. In an extreme case, in which the gain of the heat exchanger *TF* is very small, the heat exchanger is still absorbing heat as a mean value (DC component), but the fluctuating part (AC component) of the total heat is still almost equal to that of the burner, since the heat exchanger absorption has negligible fluctuations. Therefore, the ratio of total system heat fluctuations to its mean is always larger than that of the burner. This can also be understood using the data presented in Figure 5.4. If the 5% increase in the excitation signal had led to 5% increase in burner heat release and 5% increase in heat exchanger heat absorption, then the total system heat would have also increased by 5%. However, the heat exchanger absorption has only increased by 2%, which means that the total heat of the system (burner minus heat exchanger) has increased more than 5%. This causes a gain of the total *TF* to be larger than one. Note that this behavior may change depending on the constructive or destructive behaviors due to the changes of *TF* phase for various frequencies.

(a)   (b)
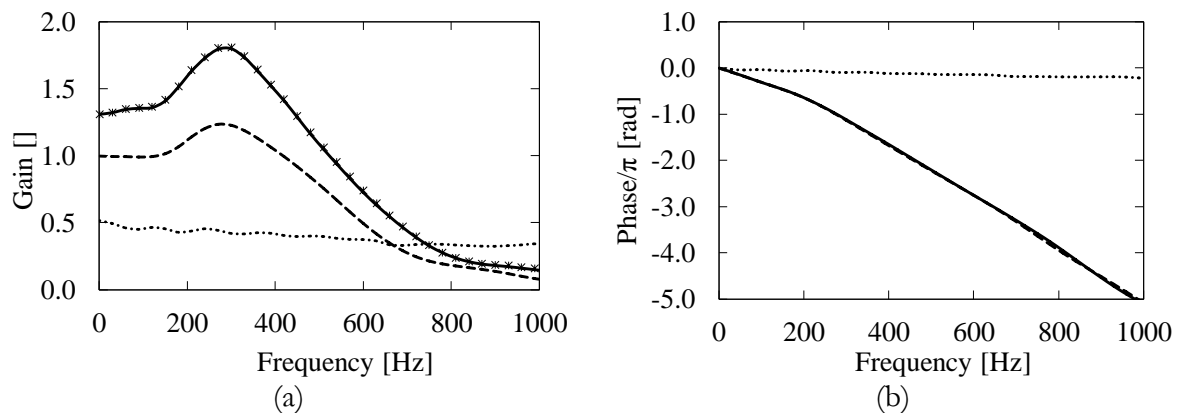
Figure 5.7: The gain (a) and phase (b) of the TF *of the total system via CFD (——), via Equation (5-7) (✳), burner (– – –) and heat exchanger (······) when it is placed at Y=50mm.*

Figure 5.8 shows the gain and phase of *TM* for the burner, heat exchanger and total system. Since *TM* is relating the velocities upstream and downstream of an element (dilatation rate), its gain is larger than one if the temperature increases (expansion) and smaller than one if it decreases (contraction). This is clearly visible in Figure 5.8. The *TM* and *TF* are related via Equation (5-3) and depending on the values of *TF* and *θ*, *TM* may fluctuate with frequency. This can be seen in the form of fluctuations in the gain of *TM* in Figure 5.8. These fluctuations are also physically important since they illustrate that the information obtained directly from the *TF* does not suffice for judging the system dilation rate, which is important when the system is exhibiting Helmholtz oscillations. While the dilatation rate is around six (the steady-state value due to the temperature jump) at *400Hz*, it reduces to one (transparent element) slightly above *600Hz*. The phase of *TM* of the total system follows that of the flame for the same reason mentioned for *TFs* (see the explanation of Figure 5.7).
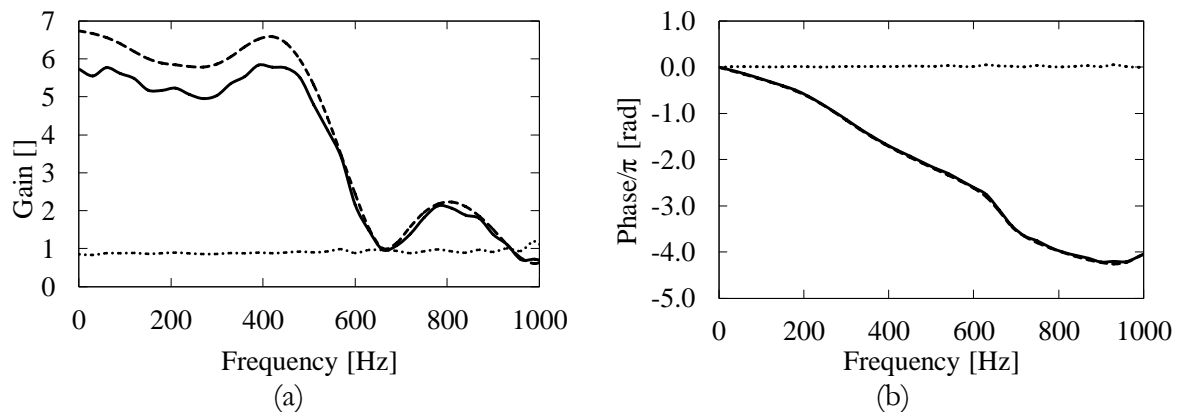
Figure 5.8: The gain (a) and phase (b) of the TM of the total system (———), burner (‑ ‑ ‑) and heat exchanger (······) when it is placed at Y=50mm.

5.5.2   Varying the location of the splitting section

The calculations for the case with the heat exchanger far downstream of the burner are straightforward, however they become more complicated when the heat exchanger is placed closer to the burner. A first step towards bringing the heat exchanger closer to the burner is to keep the heat exchanger location fixed, but vary the location of the splitting section. In order to study the response of the heat exchanger under these conditions, the splitting section is moved from its previous position (*Y=6L=10D=30mm*) to further upstream (*Y=1.4L=2.33D=7mm*) and downstream (*Y=9.2L=15.67D=47mm*) and its response is investigated. The flame height is *L=5mm* and the heat exchanger diameter is *D=3mm* and is placed at *Y=50mm*, therefore, *Y=7* and *47mm* correspond to *2mm* downstream of the flame tip and *1.5mm* upstream of the heat exchanger surface, respectively. This is the closest possible to the flame tip and heat exchanger surface, without interfering with the temperature boundary layers.

In Figure 5.9, the changes of velocity magnitude with time at these sections are shown. At each section, the transient velocity magnitude is plotted at the point where *X=0mm* (the left symmetry line) in dashed lines, at *X=2mm* (the right symmetry line) in dotted lines, and the average velocity

on the section in solid lines. The two points in x-direction are shown on the splitting section in Figure 5.6 and the values are normalized to their corresponding initial values before the 5% step excitation. At each section, if the velocity profile preserves its shape with time (stays self-similar), the normalized velocity at all the points in x-direction will plot on each other in Figure 5.9. This is the case for *Y=30* and *47mm*, however for *Y=7mm* there is a variation, which is explained later. Despite this variation, the average value on the splitting section (solid lines in Figure 5.9,) has almost identical transient behavior for all the sections. This means that the x-averaged value at any of these sections (even the ones extremely close to the flame tip or heat exchanger surface) or any other section between them may be used for splitting the system into the burner and heat exchanger sub elements.
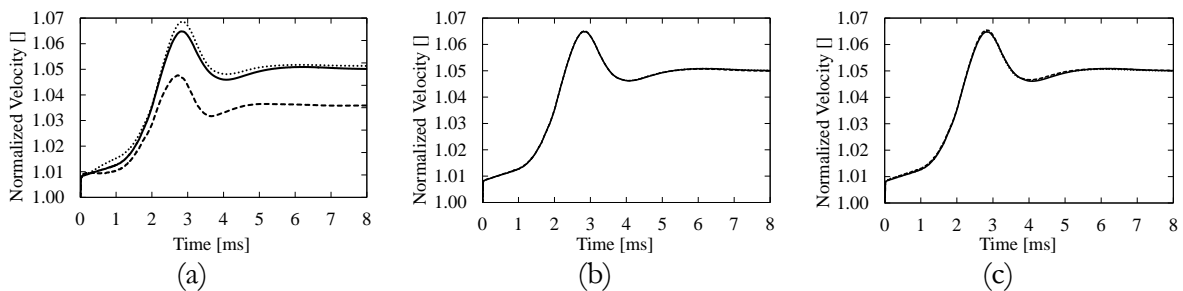
Figure 5.9: Time history of normalized velocity magnitudes at Y=7mm (a), Y=30mm (b) and Y=47mm (c); X=0mm (– – –), X=2mm (······) and average on the splitting section (——); the heat exchanger is placed at Y=50mm.

Figure 5.10 better illustrates the self-similarity of velocity profiles with time. The non-normalized velocity magnitudes along the x-direction are plotted for the first time step (just before applying the excitation) in dashed lines, for the last time step in solid lines and for 800 intermediate time steps (*8ms*) in semi-transparent gray lines, forming the gray shaded area. For *Y=7* (Figure 5.10a) and *47mm* (Figure 5.10c), it can be observed that the non-uniform velocity profiles are induced by the flow acceleration through the flame and contraction between the heat exchanger tubes, while the velocity profile at *Y=30mm* remains flat. The velocity profiles at *Y=30* and *47mm* stay self-similar with time, however, at *Y=7mm* the expansion caused by the flame grows in x-direction, i.e. the increase in velocity is smallest at *X=0mm* and largest at *X=2mm* (see Figure 5.10a). This was previously seen in Figure 5.9a as the difference between the dashed and dotted lines, and is because the flow expansion through the flame front is weaker at the flame tip (*X=0mm*).
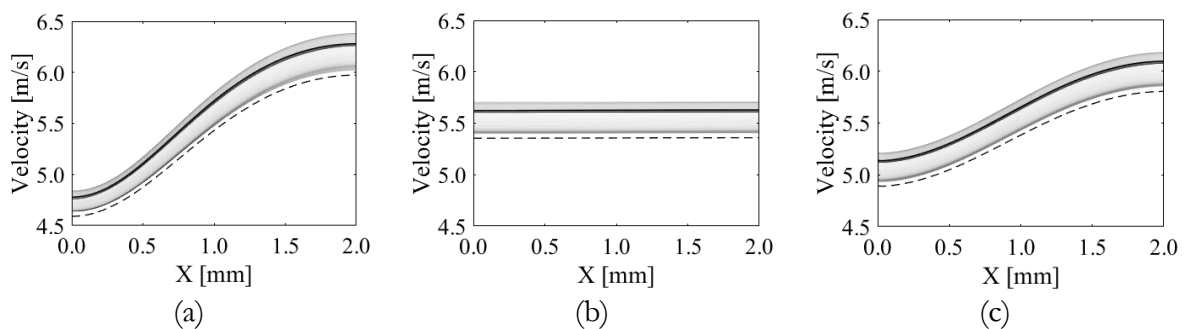
Figure 5.10: Velocity magnitude profiles at Y=7mm (a), Y=30mm (b) and Y=47mm (c); the first time step (– – –), last time step (——) and 800 intermediate time steps (gray shaded lines).

The gain and phase of the heat exchanger *TF* using the x-averaged velocities at the three sections are plotted in Figure 5.11. The markers show the results for the "NoFlame" case, i.e. the case where no flame is simulated and the heat exchanger is only exposed to a fluctuating flow with post-combustion properties (mean velocity, composition and temperature). It is evident that choosing different heights for calculating the heat exchanger transfer function leads to almost the same results, which are all in acceptable agreement with the NoFlame case. The observed fluctuations in the gain and phase are because in the NoFlame case, the excitation signal is a perfect step function, while for the other cases the measured velocity at the sections are used as excitation and this measured velocity is not a perfect step. This poses an imperfect excitation signal that may lead to numerical errors. In fact if a step function is not possible as excitation (for example in measurements), a separate study needs to be performed to find a proper excitation signal. Details of creating such signals can be found in the literature [139]. These results prove that the discussed decoupling method is valid even when the heat exchanger is exposed to a non-flat velocity profile.
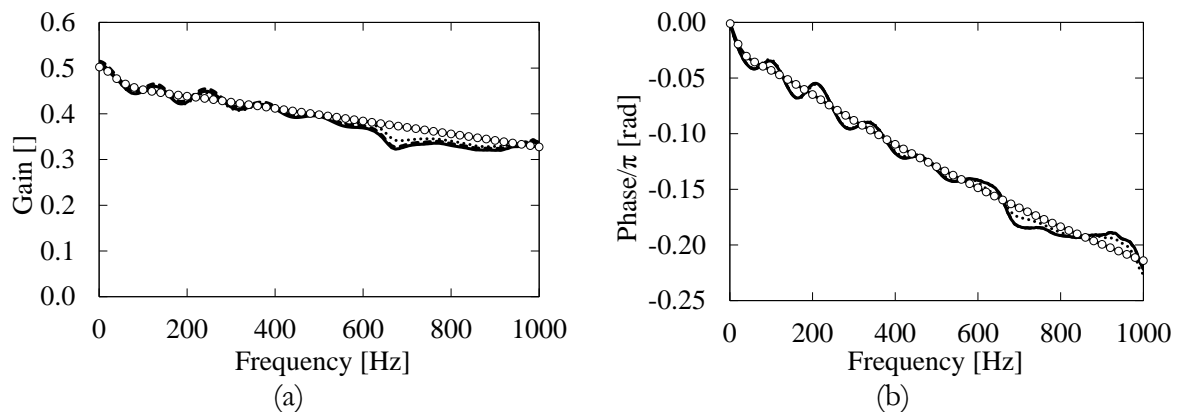
Figure 5.11: The gain (a) and phase (b) of the heat exchanger TF when it is placed at Y=50mm with respect to x-averaged velocity at Y=7 (……), 30 (− − −) and 47mm (——), and the NoFlame case (−O−).

5.5.3 Varying the distance between the burner and the heat exchanger

Decreasing the distance between the burner and heat exchanger initially exposes the heat exchanger to a non-flat velocity profile, then a non-flat temperature and/or concentration profile, and finally flame quenching and different impingement regimes occur. In order to find the physical limits of the validity of the described method, multiple simulations are performed with the heat exchanger at *Y=50, 25, 10, 8, 7* and *6mm*, which correspond to *10L, 5L, 2L, 1.4L* and *1.2L*. The network model approach is then taken and the time signals and Equation (5-3) are used to obtain the *TF* and *TM* for the burner, heat exchanger and total system. In Figure 5.12, some of the cases (*Y=10, 8, 7* and *6mm*) are shown as pairs of 2D plots of reaction heat (left side) and temperature (right side). Merging of the temperature fields of the flame and heat exchanger is visible for all except *Y=10mm*, and flame quenching and impingement occur for *Y=7* and *6mm*. It is important to note that depending on the mixing and/or diffusivity of velocity, concentration and temperature, the heat exchanger may first be exposed to a non-flat profile associated to any of them. However, in lean premixed combustion, where thermoacoustic instabilities are important, the time scales of

viscous dissipation is much larger than thermal and species diffusion and mixing. Therefore, the focus of the analysis is on the velocity profiles.
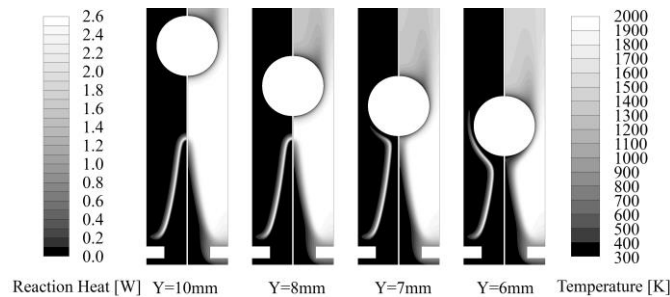
Figure 5.12: Contours of reaction heat (W) (left sides) and temperature (K) (right sides) for the cases with the heat exchanger at Y=10, 8, 7 and 6mm.

The gain and phase of the burner *TF* for different distances between the burner and the heat exchanger are plotted in Figure 5.13. As observed in section *"5.5.2 Varying the location of the splitting section"*, the burner *TF* in the non-impinging cases does not significantly change as the distance decreases. The reduction in the overshoot of the gain is due to carbon monoxide formation around the heat exchanger and the fact that all reaction source terms are integrated in the whole domain. Therefore, the carbon monoxide to carbon dioxide conversion is also included and slightly alters the integrated reaction source term. These differences were completely removed for an adiabatic heat exchanger. For *Y=7mm*, the flame stretches due to the flow distortion around the tube (see Figure 5.12), causing a longer flame front and a larger phase. However, for *Y=6mm* the flame front moves towards the high velocity region between the adjacent tubes. The higher velocity decreases the convective traveling time of perturbations along the flame front and results in a slightly smaller phase compared to when *Y=7mm*.
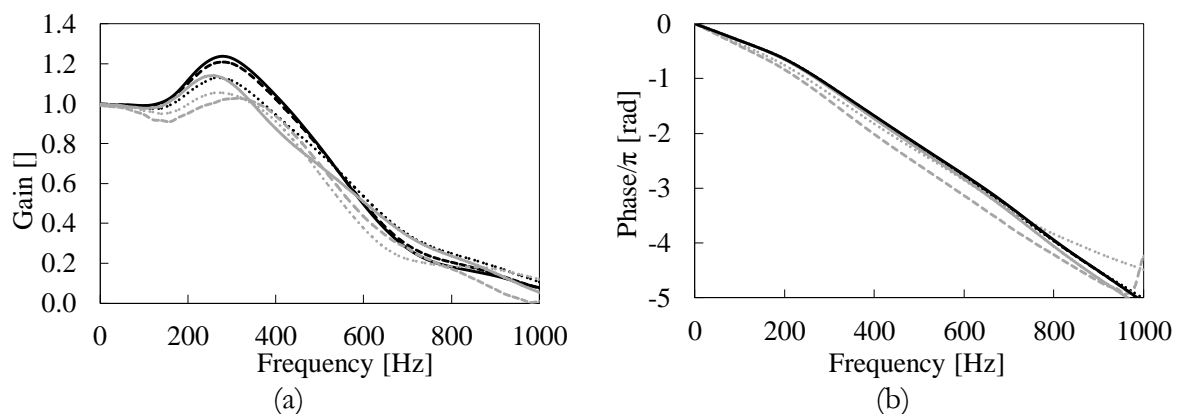
Figure 5.13: The gain (a) and phase (b) of the burner TF when the heat exchanger is at Y=50 (——), 25 (---), 10 (······), 8 (——), 7 (---) and 6mm (······).

In general, changing the distance between the burner and heat exchanger marginally changes the flame *TF*. However, for the impinging cases, the heat exchanger is additionally exposed to unburned mixture. This results in a different behavior, like a different phase shift of the heat exchanger *TF*. Therefore, it is crucial to investigate the response of the heat exchanger and total system as well.

Figure 5.14 shows the gain and phase of the heat exchanger *TF* when its excitation (u_{mid}) is calculated using the burner *TM* in Equation (5-3) and the inlet velocity (u_{in}). For all non-impinging cases (*Y=50, 25, 10* and *8mm*), the heat exchanger *TF* is close to that of the NoFlame case (see Figure 5.11). For the impinging cases (*Y=7* and *6mm*) however, a physical middle section between the burner and heat exchanger does not exist and u_{mid} in these cases is associated to a 'virtual' point. The extremely large gains for the impinging cases are therefore an artifact of calculating using this virtual point. In these cases, the heat exchanger is exposed to two streams of hot (burned) and cold (unburned) flow (see the white and black colors of the temperature contours in Figure 5.12). As the velocity increases, the tube is further exposed to the cold stream and its total heat flux decreases. This reflects in a phase shift of the order of π in the phase of the heat exchanger *TF* (see Figure 5.14b).
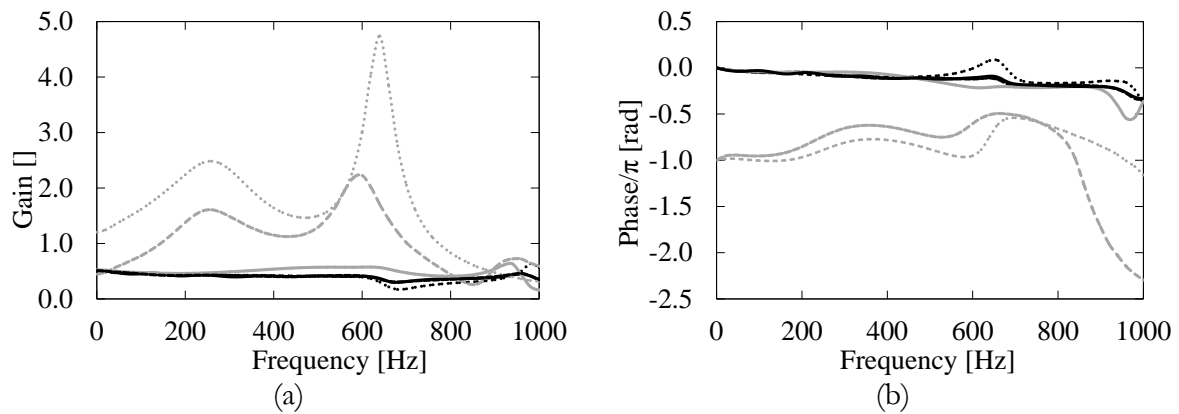
Figure 5.14: The gain (a) and phase (b) of the heat exchanger TF when it is placed at Y=50 (——), 25 (– – –), 10 (······), 8 (——), 7 (– – –) and 6mm (······), and its excitation (u_{mid}) is calculated using the burner TM in Equation (5-3) and the inlet velocity (u_{in}).

For all the investigated cases, the mean heat flux at every point on the circumference of the heat exchanger tube is negative, i.e. in the absence of fluctuations, the heat exchanger is constantly absorbing heat from the system. However, for the impinging cases this sink is acting with a phase shift of π (see Figure 5.14b) and may have adverse effects. These effects should reflect in the dilatation rate and therefore the *TM* of the total system. The gain and phase of the total *TM* are plotted in Figure 5.15. The baseline is considered for the case without a heat exchanger (NoHex) and is marked by symbols. As intuitively expected, adding a heat exchanger far downstream introduces an opposite temperature jump and decreases the gain of the total *TM* compared to the NoHex case. For the impinging cases on the other hand, the gain of the *TM* is larger than that of the NoHex case. This is a result of the counter-phase behavior of the heat exchanger, i.e. although the total temperature ratio in Equation (5-3) is smaller compared to the NoHex case, the gain of the total system *TF* is larger (see Figure 5.7a), resulting in a larger *TM* and therefore larger dilatation rate.
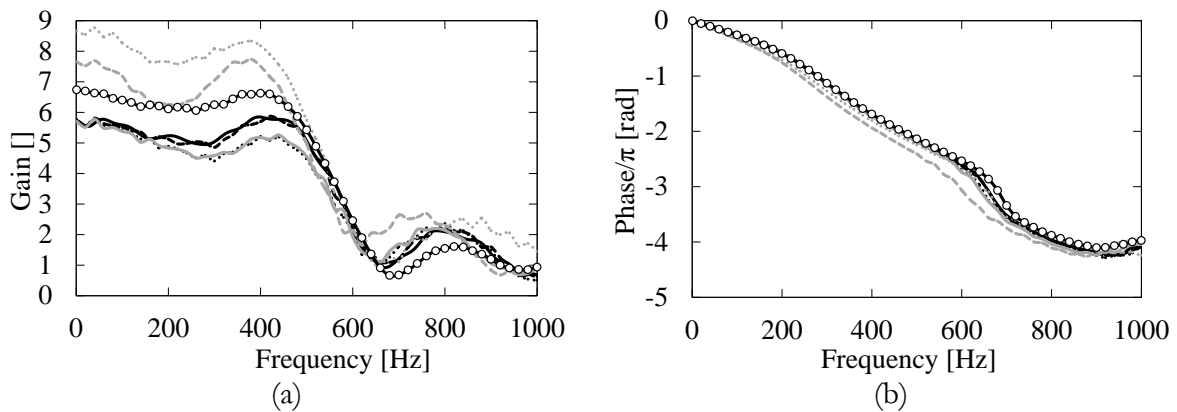
Figure 5.15: The gain (a) and phase (b) of the total TM in the NoHex case (—O—) and when the heat exchanger is placed at Y=50 (——), 25 (— — —), 10 (……), 8 (———), 7 (— — —) and 6mm (……).

Here a heat exchanger with only one tube row is considered and the results indicate that the phase of the heat exchanger has a negligible value compared to the burner. However, in other configurations such as multiple rows of heat exchanger tubes and the presence of von Kármán vortices, the heat exchanger may acquire larger phase values and adversely affect the instability of the system, even when placed far away from the burner [6]. In addition, the methods and processes discussed in this work are applicable to any other configuration of burners and heat exchangers. The general conclusions to be used for this purpose are formulated in the following section.

5.6 Conclusions

A method is introduced for predicting the thermoacoustic response of a simplified heating appliance using the behavior of its major constituting elements, i.e. the burner and the heat exchanger. To fulfill this purpose, the network model approach is used to decouple the effects of the elements, considering details of velocity profiles. The results of the conducted research allow formulating the following conclusions:

- For a wide range of conditions, the *TF/TM* of the combination of the burner and heat exchanger can be represented as a superposition of their independently measured or modeled *TF/TMs*. A mathematical approach that allows the proper superposition of the individual *TF/TMs* into a combined *TF/TM* is proposed and validated.
- In the case of large distance between the burner and heat exchanger, the interactions are purely acoustic by nature and can be described within, e.g. the acoustic network model approach. The corresponding composition method provides good predictions for all distances between the burner and heat exchanger that are larger than the flame height. It shows that a flat velocity profile, that promotes planar acoustic waves, is not a necessity for decoupling the system using this method.
- For distances comparable to flame length, the method requires registering average velocities on a physical plane between the flame tip and the heat exchanger surface. This is possible for all distances longer than the flame length if there are negligible intrusions in temperature and/or species concentration profiles. If not, the interaction intensifies and causes the phenomenon of flame impingement.

- In general, in all cases without flame impingement, one can treat the burner and the heat exchanger as two acoustic elements acting opposite each other, i.e. the oscillations of dilatation rate introduced by the burner are reduced due to the presence of the heat exchanger.

- When the distance between the burner and heat exchanger is so small that flame impingement occurs, modifications of both the flame shape, temperature and the profile of flow approaching the heat exchanger take place. In this case, the combination of the burner plus heat exchanger has to be considered as one coupled thermoacoustic element. Furthermore, the response of the coupled system in these cases changes drastically due to the heat exchanger acting as a counter-phase sink and increasing the cumulative oscillations of dilatation rate.

This investigation also implies that a correct modeling of the thermoacoustic response of a heating appliance requires including the effects of both the burner and the heat exchanger as active acoustic elements, especially when flame impingement occurs. A heat exchanger placed relatively far downstream of the burner results in a decrease in the gain of the combined *TM*, that may help abate possible instabilities. On the contrary, if flame impingement occurs the effects of the heat exchanger may enhance these instabilities.

Stability Analysis of Simplified and Realistic Heating Appliances

In this chapter, the obtained data about the thermoacoustic behavior of the burner and heat exchanger are combined using the lumped and distributed methods in order to construct an acoustic model of the heating appliances. The stability of this model is then analyzed for various configurations of burners and heat exchangers with varying thermoacoustic properties. In section 6.1 *"Intrinsic thermoacoustic modes and their interplay with acoustic modes in a Rijke burner"*, the results of a simplified Rijke burner model without any heat exchanger are presented and a large parametric study is performed using a network model and the lumped method in order to create a holistic picture of the system stability. In this section, special focus is given to the intrinsic thermoacoustic modes since the physics of pure acoustic modes in a Rijke burner are well-known. Then, the effects of including various configurations of the heat exchanger to the system is analyzed using a Helmholtz solver and distributed method in section 6.2 *"A Rijke tube model with various heating and cooling elements"*. Sections 6.1 and 6.2 have been published in *International Journal of Spray and Combustion Dynamics* [27] and *Proceedings of the European Combustion Meeting* [6], respectively. These sections are reprints of the published articles and consequently, some overlap may be expected between the introductory sections of this chapter and the first three chapters of this thesis.

6.1 Intrinsic thermoacoustic modes and their interplay with acoustic modes in a Rijke burner

Thermoacoustic instabilities constitute a major branch of combustion instabilities that are undesirable for combustion systems designed to work steadily. Such instabilities are a result of strong coupling between the system acoustics and fluctuating heat generation. The acoustic fluctuations modulate the heat release and this in turn produces acoustic waves. A thermoacoustically unstable system may exhibit pressure fluctuations with an amplitude in the order of audible sound (in e.g. heating appliances) up to operating pressure levels (in e.g. rocket engines). These pressure fluctuations limit the operating range of the system or even cause structural damage and thus should be avoided or controlled.

The common practice in studying thermoacoustic instabilities is to first identify the coupling between the active elements (such as burners and heaters) and the acoustic field. Then it is possible to calculate the complex eigenfrequencies of the system including the active and passive elements (such as ducts, area changes and terminations). This approach is used in the framework of the so-called network models and numerical Helmholtz solvers. In traditional thermoacoustics, it is understood that for a system to be thermoacoustically unstable, a coupling should exist between the active elements and the acoustic reflections from the rest of the system. However, it was established recently that a combustor may be unstable even in the absence of any acoustical reflections upstream or downstream of the burner. In practice, such conditions have been observed as instabilities that do not respond adequately to the changes in upstream and/or downstream acoustic properties[1]. This type of instabilities is thought to originate from an inherent coupling within the burner itself and are called Intrinsic Thermoacoustic (ITA) instabilities.

The modes of the coupled acoustic-flame system tend to be associated either to an "acoustic mode" or to an "ITA mode", with the acoustic modes being associated to cavity acoustic oscillations and the ITA modes being associated to the inherent coupling of the burner. In addition, the system modes can be evaluated in two limit cases that help investigating their properties. The first case is when all elements in the system are considered thermoacoustically passive, and the obtained modes are called "pure acoustic modes". The other case is when the system boundaries or the boundaries at the interfaces of a selected element are considered non-reflecting, and the obtained modes are called "pure ITA modes".

Bomberg et al.[133] have shown that when the flame scattering matrix is represented with respect to causality, a pole of the transfer matrix can be found at a specific frequency. The gains of the scattering matrix elements are maximum at this frequency, showing that some kind of resonance is expected. They used experimentally measured transfer functions (TF) of a stable and an unstable burner to demonstrate the difference in the thermal and acoustic responses of the flames. They identified the ITA feedback loop through the acoustics-flow-flame-acoustics coupling and were able to relate the experimentally observed instability to the intrinsic thermoacoustic instability. Hoeijmakers et al.[140] theoretically showed that the transfer matrix poles correspond to the frequencies at which the phase of the flame/burner transfer function crosses odd multiples of π. This means that, theoretically, any active acoustic element that has a transfer function phase

of at least π, has at least one ITA mode. They also performed measurements with nearly anechoic conditions upstream of the burner and showed that the trends of the observed instabilities are as can be expected from tracking the poles of the transfer matrix. Therefore, they concluded that the observed instability was an ITA mode. These two studies initiated a series of additional studies on the intrinsic thermoacoustic instabilities in the past few years. Emmert et al.[141] used a simplified network model, and Courtine et al.[142] and Silva et al.[100] used DNS to confirm and capture intrinsic thermoacoustic instabilities in confined laminar premixed Bunsen flames.

The initial investigations on ITA instabilities have created the motivation and momentum for the community to investigate ITA instabilities in more detail. Consequently, recent studies have focused on studying their behavior. Hoeijmakers et al.[143] have numerically shown that in practice a mode of the coupled acoustic-flame system (where reflections are not perfect) could be a combination of pure acoustic and ITA modes. In addition, Silva et al.[144] recently reported measurements showing acoustic modes and ITA modes occurring simultaneously in a swirl combustor. In order to make adequate mitigating choices it is very important to identify if an unstable mode is acoustic or ITA. In a recent study, Emmert et al.[26] used experimentally measured values of flame transfer function within a network model and introduced a matrix transformation method that allowed them to decouple acoustic and ITA modes from full system modes. By performing a sweep on a defined coupling parameter, they observed that some system modes originate from pure acoustic and others from pure ITA modes. Their procedure identifies the ITA modes, but the coupling parameter does not have a physical representation and reducing it to values below unity is unphysical. Albayrak et al.[145] have very recently introduced a convective scaling for ITA modes of a premixed swirl combustor. They have shown that the including flow inertia affects the frequencies of ITA modes and the frequencies found using the modified approach better match with the experimentally observed unstable frequencies. These effects are significant in burners with large flow inertia, thus area change. Their new criterion helps in associating the peaks observed in the sound pressure level spectra to either ITA or acoustic modes.

In a general scheme, the peculiarity of the problem we consider is that an element with internal feedback is placed inside a system with external feedback, and then some interplay between these two feedback loops may be expected. This situation is generic and may be encountered in different branches of science. One physically close situation was studied in another branch of acoustic research, which also may be interpreted in terms of intrinsic and external feedback interplay. The example is the edge-tone configuration, which consists of a planar jet from a thin slit that interacts with a thin sharp edge placed parallel to the slit further downstream. The jet oscillations observed in this configuration are essentially a hydrodynamic instability[146]. Moreover, it is well known that acoustical feedback from surroundings influences the oscillation frequency and amplitude. Some experiments have shown that the oscillation frequency of an edge-tone placed above a table was affected by the reflection of acoustic waves from the table[146]. It was also observed that surrounding geometries affect the unstable frequency of the system. When the system is placed in the opening of a pipe, the edge-tone becomes an organ pipe and forms strong acoustical feedback. In such configurations, the edge-tone is not dominant, however it plays a significant role in the

transients of the flue instruments[147, 148]. Additionally, Castellengo[149] has shown that the edge-tone modes depend strongly on the geometry of the mouth of the instrument. While for a recorder (where the jet length W is typically four times the jet thickness h) only one edge-tone mode is active, for typical organ pipes (where W/h can be as large as 12 or 20) many edge-tone modes are observed. Therefore the attack transient of an organ-pipe is often much more complex than that of a recorder.

Most of the research on ITA instabilities has been focused on establishing a fundamental base for confirming the existence and importance of intrinsic thermoacoustic instabilities. In addition, using available experimental data to confirm the findings has narrowed the window of investigation to specific case studies. However, a broader picture of ITA and acoustic modes in a system is required in order to unveil more of the independent and coupled behavior of these modes. In addition, it is not always obvious whether a given mode is acoustic or ITA, and whether any interplay exists between these modes.

This work aims to address these issues by identifying ITA modes using multiple parametric sweeps. A Rijke burner (a combustor with a flame and temperature change, but no area change) is investigated using a linear acoustic network model. All the system modes with frequency below the cut-on frequency for non-planar acoustic waves are studied. This frequency range is usually below *1kHz* which is the range of focus for most thermoacoustic instability studies. The system is examined for a range of values of flame time delays, temperature ratios and reflection coefficients. Therefore, this work provides a parametric study that governs a wide range of parameters, however not every combination of parameters is likely to have some corresponding realistic configuration. Nevertheless, these parameters and their corresponding values are chosen based on (but not limited to) the realistic conditions where thermoacoustic instabilities may occur.

The time delay and temperature ratio are directly related to the combustion properties of the burner. A leaner flame results in larger time delays and smaller temperature ratios. In addition, the use of non-conventional fuels can also result in various combinations of flame time delays and temperature ratios[6]. Moreover, a constant temperature ratio and varying time delay can mimic the cold start for perforated premixed burners, since the stabilization temperature has a large impact on the flame time delay[1]. On the other hand, the actual acoustic conditions at the boundaries are not ideal, due to the presence of other parts, and the reflection coefficients can vary. In addition, changing the downstream temperature is meant to reveal the effects of the shift in resonance frequencies and reducing the reflection coefficients towards zero to include the limits of anechoic environment. Therefore, the four mentioned parameters are chosen for the parametric studies.

The results show complicated, yet interesting, interplays between the acoustic and ITA modes in the system. They reveal how an acoustic mode is affected by a pure ITA mode and how these effects create large growth rates in multiple system modes. The movie submitted as supplementary material very well visualizes these effects and interplays. This investigation draws a larger picture of intrinsic thermoacoustic instabilities and demonstrates that such parametric investigations on multiple system modes are crucial to obtaining correct predictions and interpretations of the instabilities in the system.

6.1.1 Theory of intrinsic thermoacoustic instabilities

The approach in this chapter follows the one described in the work of Emmert et al.[64]. The pressure fluctuations (p') and velocity fluctuations (u') together with the Riemann invariants f and g, are used to describe the propagation of acoustic waves. The upstream (u) and downstream (d) waves for the flame are illustrated in Figure 6.1, where $u'=f\text{-}g$ and $p'/\rho c=f+g$.

$$
\begin{array}{cc}
p'_u & \longrightarrow f_u \longrightarrow \\
u'_u & \longleftarrow g_u \longleftarrow
\end{array}
\quad\quad
\begin{array}{cc}
\longrightarrow f_d \longrightarrow & p'_d \\
\longleftarrow g_d \longleftarrow & u'_d
\end{array}
$$

Figure 6.1: The upstream (u) and downstream (d) waves for the flame.

For an acoustically compact flame (when its length is negligible compared to acoustic wavelength) the Rankine-Hugoniot jump conditions[150] can be applied and the scattering matrix can be obtained. In low Mach number flows the upstream and downstream pressure and velocity perturbations are related as

$$
\begin{bmatrix} \dfrac{p'_d}{\rho_d c_c} \\[2mm] u'_d \end{bmatrix} = \begin{bmatrix} \varepsilon & 0 \\ 0 & 1 \end{bmatrix} \begin{bmatrix} \dfrac{p'_u}{\rho_u c_u} \\[2mm] u'_u \end{bmatrix} + \begin{bmatrix} 0 \\ \theta TF u'_u \end{bmatrix},
\tag{6-1}
$$

where TF is a velocity-sensitive transfer function as $q'/q=TF(u'/u)$ to describe the relation between velocity fluctuations (u') and heat release fluctuations (q'). $\theta=(T_d/T_u)\text{-}1$ denotes the dimensionless temperature ratio and $\varepsilon=(\rho_u c_u)/(\rho_d c_d)$ denotes the ratio of specific impedances. These two ratios can be related based on some assumptions. Since thermoacoustic instabilities usually occur in lean combustion of light hydrocarbons, such as methane, the number of moles remains almost constant in the reactions, so the average molecular weight does not considerably change. If the mixture is also assumed a perfect gas then $\theta=\varepsilon^2\text{-}1$ [6, 133].

The feedback loop is well described by Bomberg et al.[133] and Albayrak et al.[145] and shows that the intrinsic feedback does not involve the acoustic reflections at the combustor inlet and/or outlet. It is illustrated in Figure 6.2 with red colors showing that the upstream travelling wave (c_2) generated by flame heat release, influences the velocity fluctuations upstream of the burner.
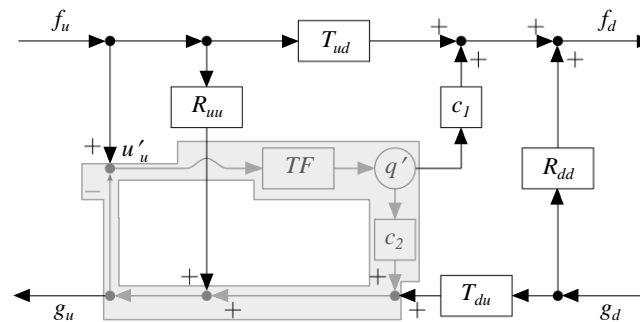
Figure 6.2: The internal intrinsic feedback loop in a combustor. R and T denote the reflection and transmission coefficients upstream and downstream of the burner (recreated from Albayrak et al.[145]).

Respecting causality in defining the input and output waves leads to the scattering matrix as

$$\begin{bmatrix} f_d \\ g_u \end{bmatrix} = SM \begin{bmatrix} f_u \\ g_d \end{bmatrix}$$

(6-2)

and using straightforward linear algebra we can obtain,

$$SM = \frac{1}{1 + TF(\varepsilon - 1)} \begin{bmatrix} \dfrac{2\varepsilon(1 + \theta TF)}{\varepsilon + 1} & -\dfrac{1 + \theta TF - \varepsilon}{\varepsilon + 1} \\ \dfrac{1 + \theta TF - \varepsilon}{\varepsilon + 1} & \dfrac{2}{\varepsilon + 1} \end{bmatrix}.$$

(6-3)

The poles of the scattering matrix are obtained when the denominator in Equation (6-3) equals zero, i.e. when *TF(ε-1)=-1*. These poles correspond to the pure ITA modes of the system[133, 143]. Since ε is real, this is only satisfied when TF is also real. Therefore, the TF phase φ of pure ITA frequencies should equal odd multiples of π and gain is *1/(ε-1)*.

In order to close the coupling between the heat release and velocity fluctuations, the *n-τ* model is used. This model is a "velocity-coupled" flame response model and assumes that the unsteady heat release is proportional to the unsteady flow velocity, multiplied by the interaction index *n*, and delayed in time by the time delay *τ* [22]. Therefore we have, $TF = n e^{j\omega\tau}$. The value of the time delay determines the change of TF phase with frequency. It is important to note that *n* shows the ratio of the magnitude of the "fluctuations" of the heat release to velocity, while θ shows the "mean" change of temperature, and thus, velocity. An acoustically passive flame has a zero *n*, but can have a nonzero θ. More detailed discussion of the role and definition of the passive/active properties of the elements of a network in application to the thermoacoustic instability analysis can be found in the work of Kornilov et al.[134].

If the time delay is assumed frequency-independent, the following expression can be realized for the pure ITA mode of order *m*

$$2\pi f_m = \frac{\varphi_m}{\tau} = \frac{(2m-1)\pi}{\tau} \Rightarrow f_m = \frac{2m-1}{2\tau}, \quad m = 1, 2, \ldots$$

(6-4)

where f_m and φ_m are the frequency and TF phase, respectively. Defining the Strouhal number as the non-dimensional frequency we have

$$St = f_m \tau = m - 0.5, \quad m = 1, 2, \ldots$$

(6-5)

The next section contains the description of the Rijke burner setup and its corresponding acoustic network model, which is chosen to investigate the behavior of the acoustic and ITA modes.

6.1.2 The Rijke burner and its equivalent acoustic network model

An illustration of the Rijke burner showing the dimensions, location of the flame, upstream and downstream temperatures, and assumed flow direction is presented in Figure 6.3. In this study, the flow is not modeled since its Mach number is small and its acoustic effects are negligible. In addition, the flame is compact and its thickness is negligible in comparison with the tube length.
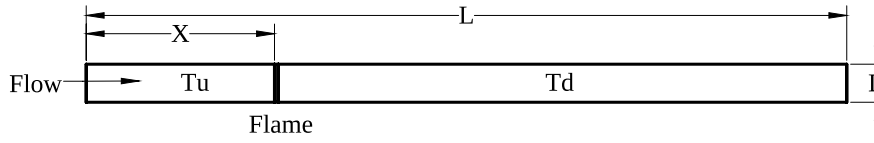
Figure 6.3: The Rijke burner model showing the combustor length L, diameter D, flame location X, upstream temperature T_u, downstream temperature T_d and assumed flow direction.

Figure 6.4 contains the equivalent acoustic network model of the Rijke burner. Here the only active element is the flame and the rest of the system are passive elements (ducts and terminations).
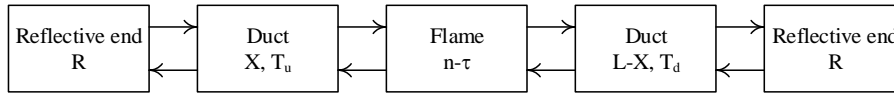
Figure 6.4: The equivalent acoustic network model of the Rijke burner.

The dimensions and values used in the current investigation are summarized as, *L=1m, X=0.25m, T_u=300K, $T_d \in [450:150:1800]K$, $\theta \in [0.5:0.5:5]$, n=1, $\tau \in [0:0.1:5]ms$ and $R \in [-1:0.2:0]$.* The tube diameter D needs to be small enough (in comparison with a cut-off diameter of the lowest frequency of propagation of transversal modes) to limit the system to only one-dimensional propagation of longitudinal acoustic waves. The fluid is considered air with temperature-dependent density and speed of sound. The flame time delay τ covers a large range of values encountered in academic cases, such as heated wires and laboratory Bunsen flames, as well as practical combustion systems, such as gas turbines and heating appliances. The dimensionless temperature ratio θ is calculated as $\theta = (T_d / T_u)-1$. Finally, the reflection coefficients at the upstream and downstream ends are varied from *-1* (fully reflecting open end) to *0* (non-reflecting), and are assumed equal, real and frequency-independent.

The constructed model is solved using taX[64], a state-space network modelling tool developed by Technical University of Munich. This network model is a low order simulation tool for the propagation of acoustic waves in acoustic network systems and is able to determine the stability, mode shapes, frequency responses, scattering matrices and stability potentiality of the acoustic networks of arbitrary topology. The parametric studies create 3060 cases, for which all the system modes within the frequency range of interest are investigated. This broad investigation is expected to reveal details of the behavior of the acoustic and ITA modes as well as their possible interplays. In the following sections, the results are presented predominantly in the form of pole-zero plots showing the eigenfrequencies and the corresponding growth rates of the system modes.

6.1.3 Results and discussion

The figures presented in this section show all the system modes in the frequency window of interest. The complete sweep on time delay is performed with steps of *0.1ms*. However, the data is presented only for a few selected values, i.e. with steps of *0.5ms*. For the complete version and better impression of the trends, the reader is encouraged to see the video file submitted as supplementary material, because the high-resolution animation shows the "motion" of the modes. Each frame of the animation is the showing the data for a specific time delay. Therefore, using the

Strouhal number would mean to multiply the frequency data by the value of time delay in every frame. In addition, the Strouhal number changes as the time delay increases and this makes interpretation of the graphs more complicated. This is why the data is presented in terms of absolute frequency for this set of graphs. The center of each circle shows the frequency and growth rate of a system mode, and the radius scales with respect to the temperature ratio. The colors show the change in the reflection coefficients according to the included color map. Therefore, the black circles represent the pure ITA modes of the system. In the next two subsections, the results are split in groups of small ($\tau<1ms$) and large ($\tau\geq1ms$) time delays. The reference for this categorization is the practical range encountered in academic and industrial burners. Since the time delay is related to the convective time of perturbations in the flame, small flames usually have smaller time delays than large ones. The time delay of small laminar premixed perforated burners are usually below 2ms, but for large turbulent swirl flames in gas turbines, it can be as large as 7ms.

6.1.3.1   Small time delays ($0\leq\tau<1ms$)

The data for $\tau=0$, 0.5 and $0.8ms$ are presented in Figure 6.5. When $\tau=0ms$ (Figure 6.5a), no instability is expected and all system modes are stable, i.e. the growth rate is negative. Here, decreasing the reflection coefficients (increasing acoustic losses) only further stabilizes the system modes. This is the well-known behavior of acoustic modes. In addition, it is easy to distinguish the first, second and third modes of the system around the frequencies of 250, 550 and $900Hz$, respectively, along with the fourth mode for the cases with small temperature ratios around the same frequencies as the third mode (the sweep on the temperature ratio causes overlaps in the frequency ranges of some modes). By increasing τ from 0 to $0.5ms$, the first and third mode start to destabilize, while the second mode further stabilizes. This result is expected based on the location of the flame and has been observed experimentally as well[151]. However, as τ approaches $0.5ms$ (see the supplementary video file), the growth rate of the third mode increases to one order of magnitude larger than that of the first mode. When $\tau=0.5ms$, the first pure ITA mode enters the window of investigation and it is revealed that the third mode is significantly affected by the proximity of this pure ITA mode. Therefore, the third mode which was an acoustic mode for smaller values of τ is now an ITA mode. Therefore, the system now has two acoustic and one ITA modes in the investigated frequency range. By slightly increasing the time delay to $\tau=0.8ms$ (Figure 6.5c), a new acoustic mode enters the window of investigation following the first pure ITA mode, so that the system always has its three acoustic modes. This reconfirms the conclusions of Emmert et al.[26] about the total number of system modes being equal to the summation of acoustic and pure ITA modes.

In addition, decreasing reflection coefficients when $\tau=0.5ms$, makes the first and second mode more stable, while the third mode converges to the first pure ITA mode, which is unstable for $\theta>3$. In practice, this means that in a Rijke burner that has a flame with a small time delay, increasing the mean heat release (by using higher powers, for example) can shift the instability from the first to the third mode. This depends also on the damping of these modes and the frequency dependence of the reflection coefficient, which in turn increases with combustor diameter.

Nevertheless, similar effects have been observed experimentally before, but are not taken into account in this study.

Figure 6.5:.The eigenfrequencies and growth rates of all system modes when τ=0 (a), 0.5 (b) and 0.8ms (c), θ∈[0.5:0.5:5] (scaled by marker size) and R∈[-1:0.2:0] (scaled by color).

In order to take a closer look at the "convergence" of system modes to pure ITA modes, a finer sweep is performed on the reflection coefficients between *-0.2* and *0*. The results for the third mode are plotted in Figure 6.6. Here it can be seen in more detail that the continuous convergence to pure ITA modes occurs only when θ≥3.5. It is important not to mistake this limit with the critical gain criterion in pure ITA modes. This criterion includes a critical value of the gain of the flame transfer function, above which the growth rate of the pure ITA mode is positive. It has been derived analytically in previous works[141–143]. For the investigated configuration, the critical gain of *n=1* occurs at θ=3, which is in agreement with the theory[142].

If the system is operating in θ≥3.5 conditions, increasing acoustic losses does not fully stabilize the system. These modes are known as ITA modes[26]. In addition, Figure 6.6 demonstrates that as the reflections decrease, the growth rates of the ITA modes can change non-monotonically (follow the line of reducing reflections for θ=3.5). It can also be deduced that in presence of very small reflections, increasing θ from 3 to 3.5 dramatically changes the growth rate and a splitting occurs in the trend due to the presence of a pure ITA mode close to this frequency.

Figure 6.6: The eigenfrequencies and growth rates of all system modes when τ=0.5ms, θ∈[0.5:0.5:5] (scaled by marker size) and R∈[-0.2:0.04:0] (scaled by color). **Large time delays (τ≥1ms)**

The eigenfrequencies and growth rates of all system modes for *τ=1* and *1.5ms* are plotted in Figure 6.7. As the time delay increases to *1ms* (Figure 6.7a), the frequency of the first pure ITA mode reduces to around *500Hz* and the distribution of the system modes becomes more complicated. As the pure ITA mode moves to lower frequencies, it "drags" the ITA mode with it and "pushes" the neighboring acoustic mode (the second mode) towards lower frequencies. In Figure 6.7a, the third mode has a frequency around *600Hz*, while it was around *800Hz* for *τ≤0.5ms*, and it is still an ITA mode (i.e. it converges to the first pure ITA mode as the reflections decrease). On the contrary, other modes are acoustic modes and stabilize as the reflections decrease.

When *τ=1.5ms* (Figure 6.7b), the third mode is switched back to an acoustic mode and the first pure ITA mode is now affecting the first mode. Here a "movement" convention is chosen to describe these interplays (the reader is encouraged to follow this process with the supplementary video file). As a pure ITA mode passes an acoustic mode, it attaches to the acoustic mode, turning it into an ITA mode (if the temperature ratio is large enough), and then drags it along towards lower frequencies. The pure ITA mode eventually detaches from the ITA mode (causing it to become acoustic again) only to immediately attach to another lower acoustic mode. This "attachment" and "detachment" occurs around the frequency of the third (*900Hz*) and second (*500Hz*) pure acoustic modes, respectively. This occurs in such a way that the total number of modes is equal to the summation of the number of pure acoustic and pure ITA modes. This has been observed for a specific set of system parameters in a previous study [26], but here it is shown that it holds for almost any combination of the governing parameters.

| (a) | (b) |
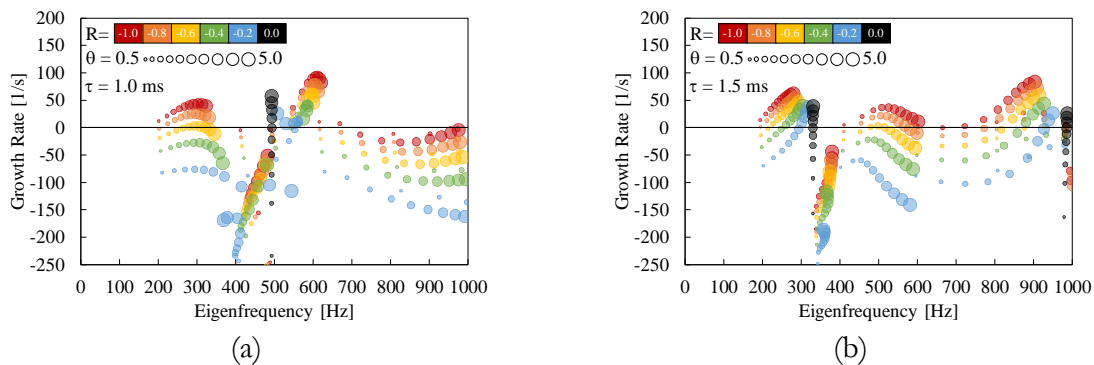
Figure 6.7: The eigenfrequencies and growth rates of all system modes when τ=1 (a) and 1.5ms (b), θ∈[0.5:0.5:5] (scaled by marker size) and R∈[-1:0.2:0] (scaled by color).

When τ=1.5ms (Figure 6.7b), the second pure ITA mode has the frequency of about *1kHz* and creates the same effect as the first pure ITA mode when the time delay was *0.5ms* (Figure 6.5b). This behavior repeats as new pure ITA modes enter the window of investigation and is very well illustrated in the supplementary video file and Figure 6.8. It is obvious that increasing the time delay results in more and more pure ITA modes to enter the window of investigation. However, it can be observed that new acoustic modes also enter the window of investigation, following the pure ITA modes. The interplay between the acoustic and pure ITA modes of the system is complicated, but repetitive. The pure ITA mode holds to the system ITA mode if there are no lower acoustic modes to which it can attach. Therefore, they remain stitched together as a pack of ITA modes. This is visible for the first mode in Figure 6.8.

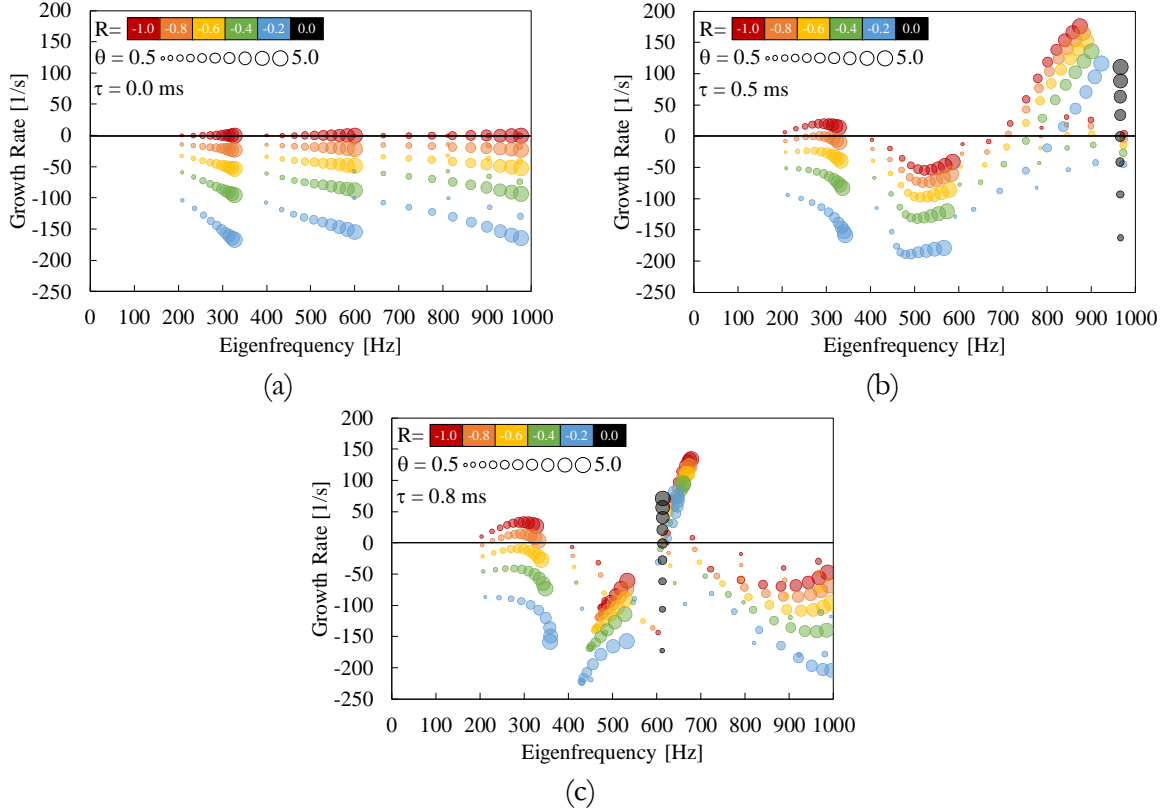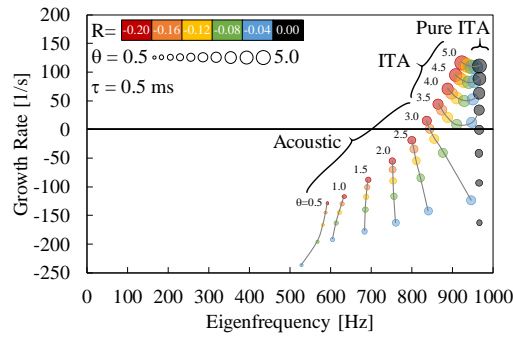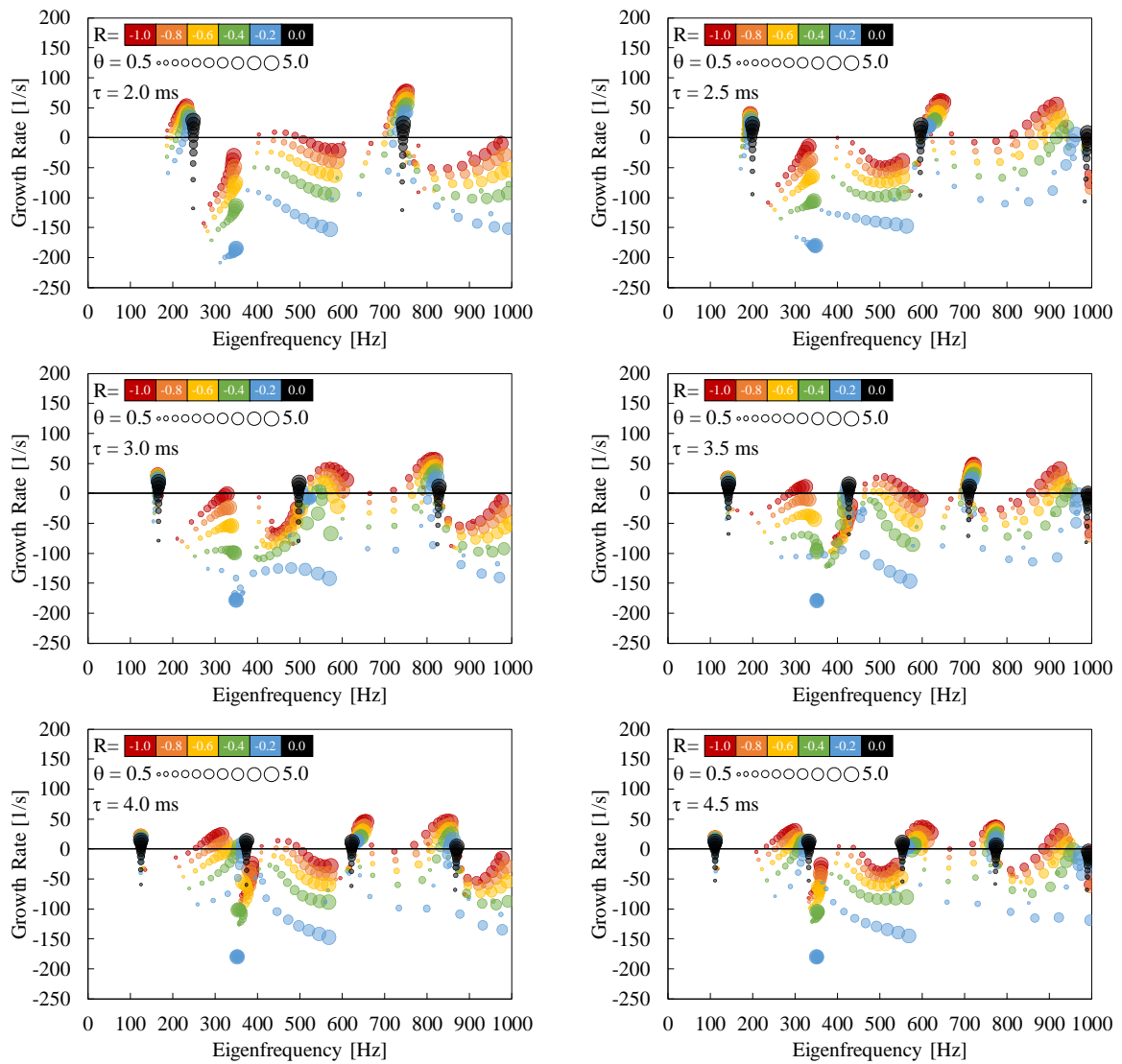*Figure 6.8: The eigenfrequencies and growth rates of all system modes when $\tau\in[2:0.5:4.5]ms$, $\theta\in[0.5:0.5:5]$ (scaled by marker size) and $R\in[-1:0.2:0]$ (scaled by color).*

The results are so far presented in the form of snapshots of the supplementary video file at specific time delays which includes the whole parameter range. In order to better study how acoustic modes are affected by pure ITA modes, it is efficient to choose a specific temperature ratio and reflection coefficient and investigate the trends in more detail. This analysis is presented in the next section.

6.1.4 The behavior of system modes near pure ITA modes

Here the temperature ratio $\theta=5$ and reflection coefficient $R=-1$ are chosen and the system modes are evaluated in terms of growth rate and Strouhal number $St=f\tau$. These values correspond to combustors with large temperature ratio and open inlet and outlet. Usually high growth rates are expected for these conditions, which is expected based on the absents of acoustic energy losses at the boundaries and the contribution of the temperature ratio to the acoustic energy gain. In addition, the time delay is further increased to $10ms$ in order to evaluate the system behavior for large Strouhal numbers.

Figure 6.9 illustrates how the Strouhal numbers of the first six system modes change with the time delay. The fixed Strouhal numbers of the pure ITA modes are illustrated with horizontal dotted lines with their values corresponding to Equation (6-5), and the convergence of the first, second and third system modes to their corresponding pure ITA modes is visible. If no pure ITA modes were present, one could expected that the Strouhal numbers uniformly increase with time delay along the dashed lines. However, Figure 6.9 clearly shows the attaching and detaching of the system modes to pure ITA modes in the form of limiting the increase of Strouhal number with time delay when the Strouhal number of the mode is close to that of a pure ITA mode.

The slope of the curve corresponding to a specific system mode in Figure 6.9 may be used as a criterion to define whether the mode is acoustic or ITA. One may define the system mode ITA, i.e. the mode is affected by the presence of the pure ITA mode, when this slope is smaller than a certain value (it is zero for pure ITA modes).
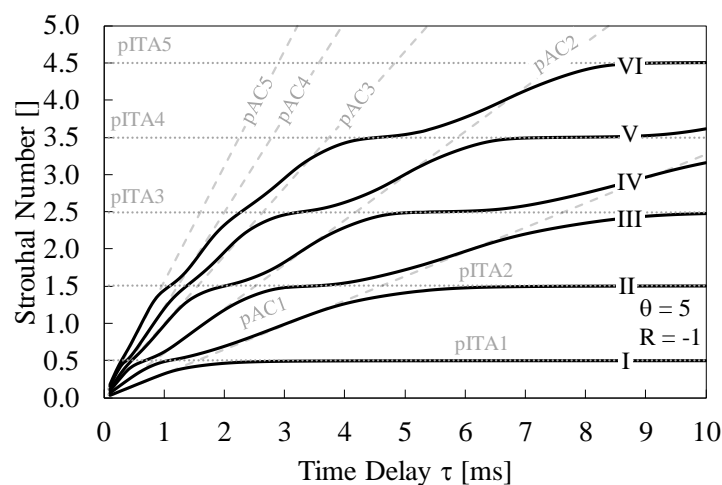
Figure 6.9: Changes in the Strouhal number of the first six system modes with time delay when $\theta=5$ and R=-1. Latin numbers denote the mode numbers and the dashed and dotted gray lines show the pure ITA and pure acoustic modes, respectively.

The complete picture of the mode behavior is obtained when the growth rates are also included. Figure 6.10 illustrates the Strouhal numbers and growth rates of the first six system modes (indicated with Latin numbers) for the investigated range of parameters (each marker indicates a system mode). Distinct fluctuations between stability and instability are visible for all the modes and these fluctuations have a counter behavior for the even and uneven modes. This behavior is expected based on the combination of τ and the location of the heat source. These fluctuations are also visible in the animated video file submitted as supplementary material. The maxima and minima occur very close to the Strouhal number of the pure ITA modes, however they deviate from it as the Strouhal number increases. Moreover, all system modes have zero growth rate for integer Strouhal numbers.

In addition, Figure 6.10 shows that higher order modes have, in general, larger growth rates and their maximum growth rate decreases as Strouhal number increases. If the growth rates of these modes are large enough, they may overcome their acoustic damping and take over the system instability from the usual first-mode instability in a Rijke burner. Therefore, it is important to investigate higher order modes to be able to see such differences.
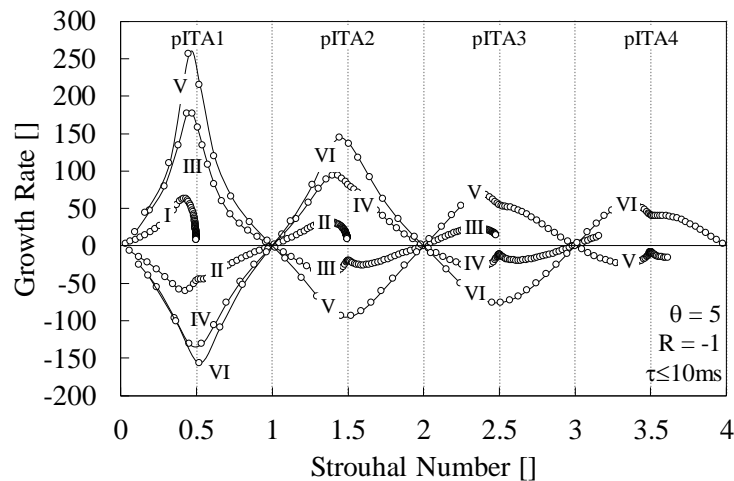
Figure 6.10: The first six system modes (indicated with Latin numbers) when θ=5, R=-1 and $\tau \in [0:0.1:10]$ms (each marker indicates a system mode for a specific value of τ).

Investigating the system modes for various ranges of parameters provides a large picture of the system modes and reveals the complex interplay between the acoustic and intrinsic modes. Although the investigation is performed on a Rijke burner, the revealed interplays are expected to be similar in more practical configurations when only longitudinal acoustic modes are considered. Therefore, the conclusions drawn in the next section are generic in nature and can be extended to other particular cases.

6.1.5 Conclusions

The thermoacoustic instabilities in a Rijke burner are investigated focusing on the intrinsic thermoacoustic modes and their interplay with the acoustic modes. A linear network model is used

and multiple parametric studies are performed with varying values of time delay, temperature ratio and reflection coefficients, covering a broad range corresponding to various (sometimes extreme) operating conditions of a combustor. This parametric study mimics practical situations, such as cold start (almost constant temperature and varying time delay) and changes in fuel composition (slowly varying temperature ratio and quickly varying time delay).

The results show that the pure ITA and acoustic modes constantly interplay with each other, even for small values of flame time delay. While the common belief for ITA modes to be effective is that the time delay needs to be relatively large, this investigation shows that ITA modes may be specifically responsible for the highest growth rates when time delay is relatively small (around *0.5ms*). In addition, the maximum growth rate occurs in different modes for different values of time delay. Therefore, the complete effects of intrinsic thermoacoustic instabilities are better captured if the investigation is not limited to specific values of time delay or the first acoustic mode.

When reflection coefficients are reduced, the presence of a pure ITA mode near an acoustic mode limits the reduction in the growth rate of the mode to that of the pure ITA mode. In certain conditions, the growth rate of this mode increases by decreasing reflections. This means that a system that has an unstable ITA mode might become even more unstable if acoustic damping is introduced at the reflective ends. Therefore, defining the characteristics of the instability by multiple parametric studies is useful before an abatement method is selected.

As the time delay increases, the number of pure ITA modes also increases and creates complicated mode overlapping. However, the observed behavior of the system modes with increasing time delay is periodic in nature, i.e. system modes couple to and subsequently decouple from pure ITA modes and become stable and unstable. This phenomenon is also seen in the form of an ITA mode attaching to a pure ITA mode for certain time delays, and then detaching from it and becoming an acoustic mode again. This motivates finer parametric investigations when thermoacoustic instabilities are investigated in a real setup in order to identify the details of the occurred mode. In addition, this observation may be a potential cause of mode switching in situations with varying time delay, such as cold start.

In this investigation, interplays are revealed between the acoustic and intrinsic modes in the system. The behaviors of these interplays are studied and it is demonstrated that for a correct prediction of thermoacoustic instabilities, it is crucial to create a broad picture of system behavior showing how various system modes react to the changes of effective parameters. Moreover, the observed effects have similarities with other systems in other branches of physics that motivates a future multidisciplinary holistic study on the systems with internal and external feedback in order to reveal the common underlying mathematics.

6.2 A Rijke tube model with various heating and cooling elements

Thermoacoustic instabilities are usually associated with lean (partially) premixed combustion systems and have been studied for more than a century [1, 76, 128, 129]. This type of combustion has various implications, such as in gas turbines, boilers and other heating systems. Many of these systems include heat sources (burners) and heat sinks (heat exchangers). Studying thermoacoustics in such systems is usually nontrivial due to the inherent coupling of hydrodynamics, chemical

reactions and acoustics. One common practice is to treat the burner as the active thermoacoustic element and the other elements as passive elements (such as ducts, vessels, terminations and heat exchangers) [3, 4]. One of the simplest and yet interesting configurations to study thermoacoustic instabilities in such systems is the Rijke tube, which shows the coupling of a heat source with the acoustics in a simple cavity (a tube with two open ends). This configuration is in many cases a good representation of unstable practical combustion systems [152, 153]. There are various studies available on the coupling of flames and acoustic waves. Consequently, many researchers have investigated various types of heat sources in combustion systems that actually include heat exchangers in reality [11, 154]. On the other hand, the transient heat transfer phenomenon in an acoustically forced flow is well studied in the past [9, 10, 155]. However, the possible role of the heat exchanger as an active acoustic element in combustion systems has mostly been ignored.

Recently, some researchers have investigated the simultaneous coupling between acoustics and both heat sources and sinks. However, these studies are limited to specific cases [7, 156] or calculation of transfer functions without discussing the stability limits of the system [35]. In addition, there are studies performed on Rijke tubes with multiple heating elements with the focus on active or passive control of the instabilities [157, 158]. This approach lacks practicality, because in practical combustion systems, the post combustion temperature is relatively high, and creating extra temperature jumps in the system requires larger powers. On the other hand, the heat exchanger is an existing element in many combustion systems and it is worthwhile to investigate if it can be used as an extra "turning knob" in the thermoacoustic design of such systems.

In this work, a Rijke tube model including both heating and cooling elements was investigated. This configuration helps revealing the combined effects of heating and cooling on the thermoacoustics in heating appliances. The ultimate goal is to answer questions such as, how can the design of the heat exchanger affect the thermoacoustic behavior of the system?

The investigation was performed in multiple steps of adding complexity in order to perform a detailed analysis of the nontrivial problem. First, the Rijke tube with only one acoustically active heat source and a positive temperature jump was considered. Then, a similar heat sink with a reverse temperature jump was added, and the magnitudes of the temperature jumps were varied as well as the time delays of the heat source and sink. This part of the investigation was motivated by the fact that the temperature jump and time delay of the heat source is immediately related to the combustion properties of the burner in heating appliances. A leaner flame results in larger burner time delays and smaller temperature jumps across the burner [18, 24, 96]. In addition, the use of non-conventional fuels may also result in various combinations of burner time delay and temperature jump.

The next step involved investigating a heat sink with distributed elements and changing its location and compactness in the tube. The distance between the heat source and sink is a key parameter in designing the emission properties of heating appliances through creating a compromise between NO_x and CO emissions. In addition, the heat sink with single (compact) and multiple (distributed) elements are representative of two major heat exchanger designs in such systems, i.e. compact tubes vs. distributed pins.

The results show that various stable and unstable situations may occur that simultaneously depend on the time delays of the heat source and sink. In conclusion, a correct prediction of the system stability requires taking into account the coupled thermoacoustic effects of the heat source and sink.

6.2.1 The Rijke tube model

An illustration of the geometry and related dimensions of the Rijke tube and their corresponding values are available in Figure 6.11 and Table 6.1, respectively. The tube is open at both ends and the flow direction implies the upstream and downstream parts. However, actual flow was not included in the model. The medium is air and its temperature increases from T_1 to T_2 across the heat source and back to T_1 across the heat sink.
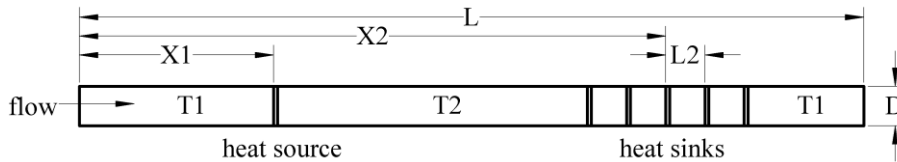
Figure 6.11: Geometry and dimensions of the Rijke tube (corresponding values are available in Table 6.1). The "flow" sign shows the assumed flow direction, but actual flow was not modeled.

The numerical Helmholtz solver, COMSOL Multiphysics® [42], was used to calculate the complex eigenfrequencies of the system in frequency domain. The model was developed by Hoeijmakers et al. [159] and describes the propagation of small perturbations in an inhomogeneous medium including heat release. As described in [159], the inhomogeneous Helmholtz equation takes the following form describing how the fluctuating heat source acts as an acoustic monopole source,

$$\frac{\omega^2}{\gamma p_0} p' + \nabla \cdot \left(\frac{1}{\bar{\rho}} \nabla p' \right) = \mathbb{F}\delta(x - X_1)\frac{\theta}{\bar{\rho}}\frac{\partial p'(X_1)}{\partial x}, \tag{6-6}$$

where p', p_0, $\bar{\rho}$ and γ are the fluctuating pressure (*Pa*), mean pressure (*Pa*), mean density (*kg/m³*) and the ratio of specific heats, respectively. $\delta(x - X_1)$ is the Dirac delta function, $\theta = (T_u - T_d)/T_u$ is the normalized temperature and $\mathbb{F}$ is a transfer function for coupling the fluctuating heat release/absorption (*Q*) to velocity (*u*) perturbations as

$$\mathbb{F} = \frac{Q'/\bar{Q}}{u'/\bar{u}}, \tag{6-7}$$

where the prime and overbar denote the fluctuating and mean values, respectively. The *n-τ* (interaction index and time delay) formulation in frequency domain was used to model the TF as

$$\mathbb{F} = ne^{-i\omega\tau}. \tag{6-8}$$

By numerically solving the constructed eigenvalue problem, one can obtain the complex eigenfrequency of the system showing the real eigenfrequency and its corresponding growth rate.

In this chapter, only the smallest eigenfrequency of the system is considered, i.e. the first acoustic mode, since it is close to the dominant resonant frequency in many thermoacoustic

systems. In addition, the heat source and sinks were assumed acoustically compact and *5mm* thick that is a few orders of magnitude smaller than the smallest acoustic wavelength in this configuration. Table 6.1 includes a list of the variables creating the parameter space. The results are presented for some selected values between the mentioned minima and maxima. These are close to the experimental data available in the literature [35, 43]. The subscripts 1 and 2 denote the properties of the heat source and sink, respectively.

Table 6.1: Geometrical and thermoacoustic parameters of the Rijke tube and the heat source (subscript 1) and sink (subscript 2).

Parameter	fixed value	minimum value	maximum value
D (m)	0.05	-	-
L (m)	1	-	-
X_1 (m)	0.25	-	-
X_2 (m)	-	0.4	0.9
L_2 (m)	-	0.01	0.06
T_1 (K)	300	-	-
T_2 (K)	-	350	1800
n_1	1	-	-
n_2	1	-	-
τ_1 (ms)	-	0.1	5
τ_2 (ms)	-	0.1	1

6.2.2   Results and discussion

The results are categorized in two sections, first the single-element heat exchanger is considered and the effects of temperature jump and time delay are studied. Then the multiple-element heat exchanger is scrutinized and the effects of heat exchange location and compactness are investigated.

6.2.2.1   Single-element heat exchanger – effects of temperature jumps and time delays

The eigenfrequencies and corresponding growth rates of the system for various time delays of the source (τ_1) and sink (τ_2) and flame downstream temperature (T_2) of *350*, *500* and *1800K* are plotted in Figure 6.12a, b and c, respectively. In each figure, the source and sink time delays vary from zero to *5* and *1ms*, respectively. This is depicted such that each pack of round markers connected with a black solid line, represents a specific source time delay (written next to it) and the sink time delay increases in the direction shown by the arrow. The gray filled triangles show the data for the cases with no heat sink, thus only one temperature jump and time delay in the system.

It is shown in Figure 6.12a that including the heat exchanger decreases the eigenfrequency (the shift from gray triangles towards the round markers) due to introducing a cold region with smaller speed of sound. The growth rate, however, remains almost the same. For the small temperature jump in Figure 6.12a, increasing the source time delay from zero destabilizes the system, but if the delay is large enough, the system is stable again. This happens at a source time delay of around

5.4ms irrespective of the sink time delay (the data at this time delay are not shown in the graph to avoid crowdedness). This period corresponds to the acoustic time scale at the frequency of *185Hz*. Therefore, if the source time delay is large enough, the system behavior repeats itself and creates the self-similar pattern in Figure 6.12a. It is worth noting that for these conditions, increasing the sink time delay monotonically destabilizes the system in the form of increasing the growth rate to multiple times its value without a sink. All the eigenfrequencies are in a small frequency span of *±7Hz* around *179Hz* and negligible frequency shift occurs by changing the time delays of the heat source and sink.

Figure 6.12b shows the complex eigenfrequencies for a larger temperature jump, i.e. $T_2=500K$. Here the shift to lower frequencies by adding the heat exchanger is more pronounced, but gets weaker as the source time delay increases. The influence of increasing τ_2 also weakens as τ_1 increases. By increasing τ_2, the system becomes unstable with its maximum growth rate around $\tau_1=1.5ms$, and stabilizes again after $\tau_1=3ms$. Compared to the case with small temperature jump (Figure 6.12a), the shift of eigenfrequency to lower frequencies by increasing τ_1 is more significant here. However, the system behavior does not repeat itself with further increase in τ_1 and the effects of τ_2 fade out. This can be seen as the circles get more and more packed together as τ_1 increases. In addition, the frequencies seem to converge to the intrinsic instability frequency of the system (this was not the case for the small temperature jump in Figure 6.12a). It is well known from previous studies [142, 143] that the intrinsic instability frequencies correspond to the frequencies at which the phase of the flame transfer function equals odd multiples of π. Therefore, for a constant time delay model

$$2\pi f = \frac{\phi}{\tau} = \frac{(2m+1)\pi}{\tau} \Rightarrow f = \frac{2m+1}{2\tau} \tag{6-9}$$

where f, ϕ and τ are the frequency, phase and time delay of the transfer function. For the first intrinsic frequency ($m=0$) we get $f=1/2\tau$, which yields values close to the frequencies plotted in Figure 6.12b, when $\tau_1 \geq 4ms$. As the system mode gets close to the intrinsic instability frequency, the existence and time delay of the sink become less effective. This is a known characteristic of intrinsic thermoacoustic instabilities. In Figure 6.12b and when $\tau_1 \leq 2ms$, increasing τ_2 first increases and then decreases the growth rate. If $\tau_1 > 2ms$, increasing τ_2 monotonically increases the growth rate, similar to small temperature jumps in Figure 6.12a. Depending on the value of τ_1, the effects of increasing τ_2 on the eigenfrequency can change from monotonic decrease ($\tau_1 \leq 2ms$) to decrease-increase ($2.5 \leq \tau_1 \leq 3.5ms$) and monotonic increase ($\tau_1 \geq 4$). In other words, the thermoacoustic behavior of the heat sink is not the same when placed downstream of different heat sources. This two-way interaction is important because it signifies the importance of simultaneously designing the thermoacoustic properties of the burner and heat exchanger in heating appliances.
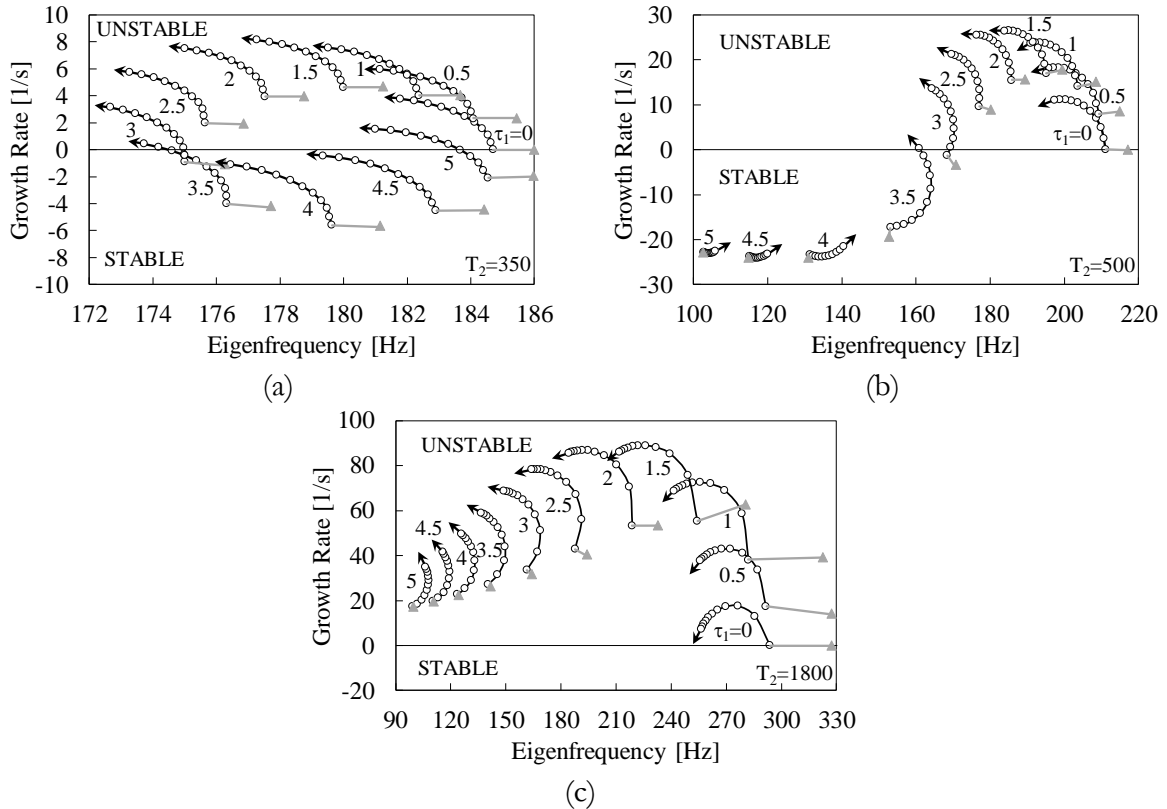
Figure 6.12: Complex eigenfrequencies of the system when $\tau_1=[0:0.5:5]ms$, $\tau_2=[0:0.1:1]ms$, T1=300K and $T_2=350$ (a), 500 (b) and 1800K (c). Each pack of round markers connected with a black solid line represent a specific τ_1 (written next to it) and τ_2 increases in the direction shown by the arrows. Triangles show cases with no heat sink, i.e. only one temperature jump and varying τ_1.

The complex eigenfrequencies for the largest temperature jump ($T_2=1800K$) are shown in Figure 6.12c. This case is mostly important because it is representative of idealized premixed combustion systems, which have been studied experimentally, theoretically and numerically. Here the system is so unstable that increasing the source time delay cannot fully stabilize it and the growth rate remains positive. This is because the effects of the burner transfer function is much larger for large temperature jumps, which greatly amplifies the system instability. The effects of increasing sink delay is similar to the case with $T_2=500K$ in Figure 6.12b. When $\tau_1 \leq 2ms$, the eigenfrequency reduces monotonically, but the growth rate changes non-monotonically. The situation is the reverse when $\tau_1 \geq 2.5ms$, with the growth rate increasing monotonically and eigenfrequency non-monotonically. We can observe the convergence to intrinsic instability frequency with increasing source delay for this case as well.

It is also important to note that the system instability is most sensitive to sink delay when this delay is the smallest. This is visible in the form of the large vertical distance between the first two points in each pack of points in Figure 6.12c. For example, when $\tau_1=1.5ms$, the growth rate increases by *37%* if τ_1 increases from zero to *0.1ms*, while it only increases around *13%* if τ_1 increases from *0.1* to *0.2ms*. Since the time delay of the heat exchanger is associated to the hydrodynamic boundary layers and is relatively small [9], this finding motivates a detailed sensitivity analysis for experimentally measured values in a practical system.

6.2.2.2   Multiple-element heat exchanger – effects of location and compactness

The presented results on the single-element heat exchanger revealed that including the effects of the heat exchanger as an active acoustic element considerably changes the behavior of the complete system. Until now, similar length scales for the heat source (burner) and heat sink (heat exchanger) were considered. However, the practical length scales of the heat exchangers can be much larger than the burners. This motivates the next step towards a more realistic system, i.e. a system with distributed and multiple heat sinks. Here the same heat source is considered, but *11* small heat sinks are also included that are placed $L_2=0.01m$ from each other to mimic a pinned heat exchanger. The location of the center of the pack of sinks changes from $X_2=0.4$ (close to the source) to *0.9m* (close to the outlet). In addition, at $X_2=0.65m$, the distance between the sink elements increases from $L_2=0.01$ to *0.06m,* in order to simulate the effects of more distributed heat absorption. For the case with $L_2=0.06m$, the heat exchanger almost fills up the space downstream of the heat source. The illustrations of these cases are presented in Figure 6.13. The shades show the temperature change between *300K* (white) and *1800K* (black). In practical systems, the heat absorption through the heat exchanger weakens as the fluid flows along the heat exchanger. However, here it is assumed that the temperature reduction occurs in multiple steps with equal temperature difference. This makes it easier to discover the effects of the distribution of the heat sinks. In addition, the outlet temperature and thus the overall efficiency of the heat exchanger is equal in all the cases.
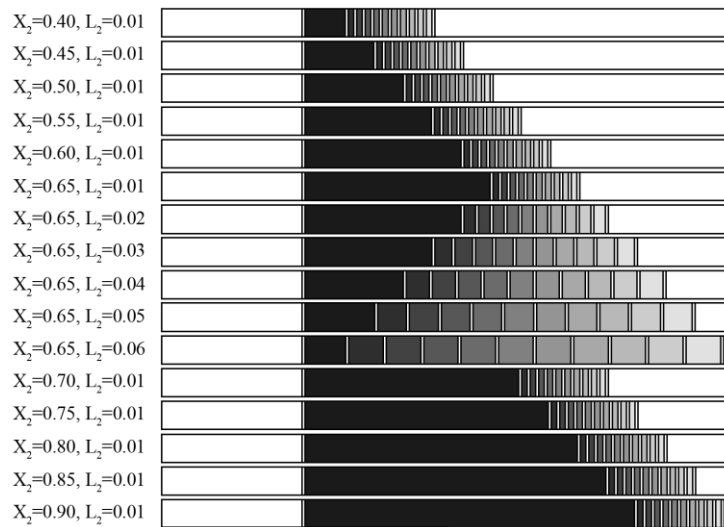
Figure 6.13: Test cases for multiple-element and distributed heat exchanger. The location of the center of the 11-element heat exchanger varies from 0.4 to 0.9m and the distance between the elements varies from 0.01 to 0.06m. The shades show the temperature change between 300K (white) and 1800K (black).

The interaction index of the source and sinks are set to unity and the sink time delay is fixed at *1ms*, while the source time delay varies from *1* to *5ms*. As discussed in the single-element section, the source time delay is important since it can alter the stability trends when the sink delay changes. The corresponding complex eigenfrequencies of the system are plotted in Figure 6.14. The black

and gray arrows show the direction of increasing X_2 (distance between the source and sinks) and L_2 (distance between the sink elements), respectively.
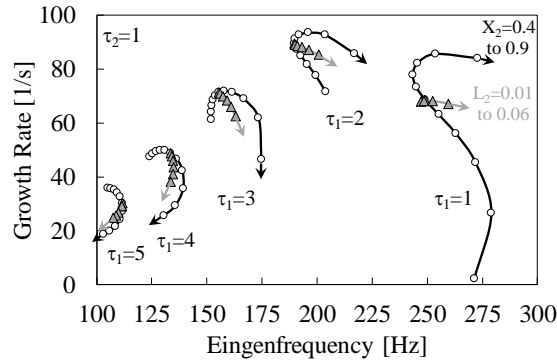
Figure 6.14: The complex eigenfrequencies of the system for $T_1=300K$, $T_2=1800K$, $n_1=n_2=1$, $\tau_1=[1:1:5]ms$, $\tau_2=1ms$, $X_2=[0.4:0.05:0.9]m$ and $L_2=[0.01:0.01:0.06]m$. Each pack of round markers connected with a black solid line represent a specific τ_1 (written next to it) and the black arrow shows the direction of increasing X_2. At $X_2=0.65m$, L_2 increases in the direction of the gray arrows, connecting the gray triangles.

The trend of increasing and decreasing growth rate with increasing source time delay is also present here, similar to the single-element sink. The values of growth rates are also in the same order of magnitude (see Figure 6.12c). However, the location of the sink has significant effects on the system stability, especially for small source time delays. This is intuitive, since a heat sink with the same temperature jump and time delay as a heat source can be the most effective. Increasing the distance between the source and sink results in the growth rate reaching a maximum and then decreasing. The location at which this maximum growth occurs, changes from very close to the outlet when $\tau_1=1ms$ to very close to the heat source when $\tau_1=5ms$. A source time delay close to practical premixed perforated burners is around *3ms*. The $\tau_1=3ms$ curve in Figure 6.14 shows that increasing the distance between the heat source and a pack of heat sinks with *1ms* time delay can increase the growth rate of the system by *17%* or decrease it by *24%*. These values are significantly important in predicting the stability of the system and need to be taken into account in the design process. Therefore, the distance between the burner and the heat exchanger is not only affecting the emissions, but also the thermoacoustics and system stability.

Finally, Figure 6.14 also shows that spreading the heat sink elements has negligible effects on stability when the source delay is small ($\tau_1=1ms$), but it decreases the growth rates towards more stable conditions if the source time delay is larger ($\tau_1 \geq 2ms$). This means that in specific conditions, a distributed heat exchanger design is more favorable for preventing thermoacoustic instabilities.

6.2.3 Conclusions

A Rijke tube is studied containing a heat source and multiple heat sinks as a simplified, but representative, model to investigate the thermoacoustic instabilities in heating appliances. Studying the effects of several parameters helped understanding the thermoacoustic behavior of such systems in various operating conditions. Among the most important parameters are the

temperature jump and time delay of the heat source and sink, which are affected by the choice of the combustion properties of the burner and heat exchanger. In addition, the distance between the heat source and sink is a key parameter in designing the emission properties of heating appliances.

The results showed that various situations of stability and instability can occur, which depend on the properties of both the heat source and sink. The effects showed a large shift in the eigenfrequency and growth rate as well. When the source and sink are placed at the first and third quarter of the tube, respectively, and the source delay is small, increasing the sink delay first increases and then decreases the growth rate of the system. However, for larger values of source delay close to practical systems, increasing the time delay of the heat exchanger almost monotonically increases the growth rates. This finding is not trivial and means that the source time delay can alter the stability trends when the sink time delay changes. It was also observed that if the temperature jumps are large enough, increasing the source time delay converges the first system mode to its intrinsic instability mode. When the system mode is near an intrinsic mode, the effects of most parameters fade out due to the nature of the intrinsic modes. Studying the effects of distributed heat sinks revealed that a critical heat sink location exists for which the maximum growth rate occurs. In addition, spreading the sink elements throughout the system reduces the growth rate.

The effects observed in this study are in some configurations to the extent that the system is predicted unstable or stable, depending on whether or not the heat exchanger is included as an active thermoacoustic element. Therefore, it is crucial to include the active thermoacoustic effects of the heat exchanger for correct predictions of system stability. An extension of the model used in this work can be developed to predict instabilities in complex full-scale heating appliances.

CHAPTER 7

Conclusions and Recommendations

One of the main motivations for the conducted research is the fact that the heating industry is suffering from thermoacoustic instabilities, mainly in the form of noise and pollutant emissions. Manufacturers have already tried to tackle this issue by tuning the burners after the system is designed and prototyped. However, this process is known to be case-dependent, inefficient, and hampering time to market, since it is based on trial and error. Therefore, we aim to conclude this work by providing a first step towards bringing the thermoacoustic properties of the complete heating system into the design process. This is achieved in section 7.1 *"Conclusions"* by summarizing the most important findings of this work emphasizing on how they can serve as a means to produce heating systems that are less prone to thermoacoustic instabilities. Note that the thermoacoustic instabilities in actual heating systems involve complicated and coupled phenomena that make it non-trivial to derive global conclusions that would work for every single design. Therefore, these recommendations are meant to provide a starting point to build on by other researchers interested in systematically solving the thermoacoustic problems in the heating industry. Therefore, the parts of this work that need more investigation are presented in section 7.2 *"Recommendations"*.

7.1 Conclusions

The most important conclusions of this work are as follows.

7.1.1 Both burner and heat exchanger are thermoacoustically active

In heating appliances containing premixed burners and heat exchangers, both of these elements are thermoacoustically active. Therefore, their acoustic responses need to be accurately assessed in order to predict the thermoacoustic properties of the complete system. Predicting the thermoacoustics of the burner using CFD simulations needs to include the details of the flame surface geometry before making geometrical simplifications. Combining multiple 2D simulations is a promising tool to mimic the full 3D effects of the flame surface in burners with slit perforations.

The heat exchanger usually shows a faster (smaller TF phase and time delay) than the burner. The gain, however, could be larger or smaller depending on the frequency range. Specifically, the low-pass behavior of the heat exchanger in generally less intense than the burner. Therefore, ignoring the active thermoacoustic properties of the heat exchanger may lead to completely wrong predictions of the heating appliance stability, especially when the distance between the burner and heat exchanger is comparable to flame length.

7.1.2 Combined thermoacoustic behavior of the burner and heat exchanger is crucial to system stability

In cases where the flame does not impinge on the heat exchanger surface, one can treat the burner and the heat exchanger as active and independent thermoacoustic elements. They may work either constructively or destructively, i.e. providing acoustic energy to or extracting it from the system. A mathematical approach that allows the proper superposition of their individual TF/TMs into a combined system TF/TM was proposed and validated. When the distance between the burner and heat exchanger is so small that flame impingement occurs, the system becomes very complex and a combination of the burner plus heat exchanger has to be considered as one coupled thermoacoustic element. The response of the coupled system in impinging cases sometimes shows considerably larger dilatation rates that makes it a stronger acoustic element and usually not desirable for a stable heating appliance.

The stability analysis of a Rijke tube including burner and heat exchanger as a model to investigate the longitudinal acoustic modes in heating appliances also showed that the combined design of the burner and heat exchanger is a determining factor in the stability of the system. Various combinations of the burner and heat exchanger time delay, temperature jump, and location can create different patterns of stability and instability. When the burner and heat exchanger are placed at the first and third quarter of the tube, respectively, and for practical values of burner time delay (*>1ms*), increasing the time delay of the heat exchanger almost monotonically increases the growth rates. This means that in such configurations an acoustically "fast" heat exchanger is desirable. However, this behavior is not monotonic for burner time delays smaller than *1ms*, which makes this finding non-universal.

7.1.3 The design of the heat exchanger considerably affects the system stability

Studying the effects of distributed heat exchanger elements revealed that there is a critical location for the heat exchanger, where the maximum growth rate of the first system mode occurs. This critical location moves from outlet towards inlet as the burner time delay increases. In addition, spreading the heat exchanger elements throughout the system reduces the growth rate. This finding directly relates to the heat exchanger design, i.e., compactly packed tubes vs. distributed pinned heat exchangers.

7.1.4 The full picture of system stability also requires considering the interplays between acoustic and ITA modes

The broad and detailed parametric analysis of the intrinsic thermoacoustic modes revealed that the pure ITA and acoustic modes constantly interplay with each other, even for small values of burner time delay. The common belief for ITA modes to be effective is that the burner time delay needs to be large enough so that the frequency of the ITA mode falls inside the frequency range of interest. However, this investigation shows that ITA modes may be specifically responsible for the highest growth rates when the burner time delay is relatively small and the frequency of the first ITA mode is outside the investigation range. When reflection coefficients are reduced, the presence of a pure ITA mode near an acoustic mode limits the reduction in the growth rate of the mode to that of the pure ITA mode. In certain conditions, the growth rate of this mode increases by decreasing reflections. This means that a system that has an unstable ITA mode might become even more unstable if acoustic damping is introduced at the reflective ends. Therefore, defining the characteristics of the instability by, e.g. multiple parametric studies, is useful before an abatement method is selected.

By increasing burner time delay, multiple pure ITA modes interact with acoustic modes and create complicated mode overlapping. However, a periodic behavior is observed in the form of ITA modes attaching to pure ITA modes for certain time delays, and then detaching from it and becoming acoustic modes again. This motivates finer parametric studies when thermoacoustic instabilities are investigated in a real setup in order to identify the details of the occurred mode. In addition, this observation may be a potential cause of mode switching in situations with varying burner time delay, such as cold start.

In this thesis, the thermoacoustic instabilities were investigated in heating appliances with premixed burner and heat exchanger. Specific attention was given to treating both the burner and heat exchanger as active thermoacoustic elements and their separate and coupled thermoacoustic properties were investigated. The possible interaction scenarios were scrutinized and the governing physical parameters responsible for these interactions were defined. The possibility and methods for decoupling their effects and reconstructing the thermoacoustic behavior of the complete system was also addressed. It was demonstrated that to correctly predict thermoacoustic instabilities, it is crucial to create a broad picture of system behavior showing how various system modes react to the changes of effective parameters. The findings presented in this thesis are meant to provide a

means to bring thermoacoustic properties into the design process of more stable heating appliances and reduce the time to market. Nevertheless, there is still a lot that can be done to build on this goal and help the industry and future researchers to go further in this field. Some of these points are addressed in the following section.

7.2   Recommendations

This section includes the suggestions for future work. Some of them have been briefly "touched" throughout the course of this work, so they are accompanied with preliminary prognosis. Others are fresh ideas to improve this branch of science and they come with suggestions to start the investigation.

7.2.1   Transfer function measurements in full-scale heating systems

While investigating simplified systems is useful in gaining understanding of the governing phenomena and important physical parameters, from industrial perspective it is always desirable to study specific products for purposes such as benchmarking. TF measurements of full-scale burners can be done in a so-called open setup, but their behavior is expected to change when enclosed inside the combustion chamber due to the differences in the flow and pressure fields. Optical routing using glass fibers may be used to route the chemiluminescence signal of various parts of a burner towards the detector.

Measuring the TF of the heat exchanger can be challenging due to the difficulty of measuring fluctuating heat flux through its walls. Efforts have been made to directly measure heat flux, but they are not yet fully reliable for various types of heat exchangers [121]. Nevertheless, it is possible to measure the TF of the heat exchanger indirectly via its TM by measuring velocity fluctuations upstream and downstream of the heat exchanger. The challenge here is that the flow temperature upstream of the heat exchanger is usually very high and conventional equipment such as hot wire anemometry cannot be used. However, other concepts of velocimetry benefiting from lasers and optical methods may be possible.

7.2.2   Thermoacoustic FEM simulations of full-scale heating systems

The same methodology as described in section 3.4.2.2 *"FEM acoustic simulations using Comsol"* can be used in full-scale 3D models of heating appliances. However, multiple challenges are also expected, such as large burners and heat exchangers, which may not be considered acoustically compact. One way of solving this issue is using distributed thermoacoustic elements (similar to as used in section 6.2 *"A Rijke tube model with various heating and cooling elements"* or in the literature [160, 161]). This concept is also used for large flames in, e.g. gas turbines, under the name of "distributed time lags" [162]. On the other hand, large burners sometimes feature varying surface perforation patterns that also motivates the possible need for locally defined TFs. Moreover, non-flat (mainly cylindrical) burners also pose geometrical challenges in the mathematical definitions of the acoustic sources.

With the help of other researchers, an effort was made during the course of this work to extend the discussed methods to full-scale heating systems in Comsol. Due to the inherent solution strategy of this Helmholtz solver, a series of iterations and a sweep of a "linearization frequency" are required to find the physical modes among the many spurious modes that occur. This process was not easy to automate since some prior knowledge of the system was also required to pinpoint the correctly predicted modes. In addition, the complex flow pattern in the heat exchanger made it difficult to create a proper network of acoustically compact elements. Nevertheless, the first results are already published [68] and it is a work in progress which can be very interesting for other researchers as well.

7.2.3 System describing function for heating systems

The operating range of the heating systems are usually well-defined by the manufacturers. If the thermoacoustic responses of the burner and heat exchanger are obtained using parametric sweeps (similar to in section 6.1 *"Intrinsic thermoacoustic modes and their interplay with acoustic modes in a Rijke burner"*), then combinations of the burner and heat exchanger may be found that are thermoacoustically preferred. The parametric sweeps can be on the most important defining parameters such as burner deck pattern, heat exchanger pin pattern, equivalence ratio (or CO_2 emission level) and mixture velocity (or burner thermal load). This idea is similar to the concept of flame describing function (FDF), where the FTF is evaluated for various excitation amplitudes and combined into one function that describes the flame in various conditions. This method requires numerous simulations and/or measurements. However, it also has a high potential in reducing the time for future analyses by creating some kind of a look-up table for the possible configurations of the products.

7.2.4 Common underlying mathematics of ITA instabilities with other branches of physics

The topic of ITA instabilities is currently a popular (and sometime controversial) topic in thermoacoustic research. As discussed in section 6.1 *"Intrinsic thermoacoustic modes and their interplay with acoustic modes in a Rijke burner"*, there seems to be similarities between this phenomenon and other phenomena in other branches of physics, e.g. edge tones in organ pipes, where a sub system with internal feedback is placed inside another system with external feedback. The details of the governing mathematics of the ITA instabilities are not yet well known, while they can provide a broad understanding of how ITA modes behave in the system. The eventual results of the parametric study in this work pose open questions, such as, why do the maximum growth rates of almost all system modes occur around the frequency of some pure ITA mode, or why do these maxima shift slightly away from pure ITA frequencies for higher Strouhal numbers? Giving answers to such questions requires a more sophisticated theoretical investigation, for which a good foundation of case studies is available now.

Bibliography

[1]   Poinsot, T.: Prediction and control of combustion instabilities in real engines. Proc. Combust. Inst. 36, 1–28 (2017).

[2]   Poole, C., Darwazeh, I.: Immittance parameters. In: Microwave Active Circuit Analysis and Design. pp. 143–166. Elsevier (2016).

[3]   Herrin, D.W., Zhou, L., Li, T.: Validation of a Low-Order Acoustic Model of Boilers and its Application for Diagnosing Combustion Driven Oscillations. (2013).

[4]   Jaensch, S., Merk, M., Gopalakrishnan, E.A., Bomberg, S., Emmert, T., Sujith, R.I., Polifke, W.: Hybrid CFD/low-order modeling of nonlinear thermoacoustic oscillations. Proc. Combust. Inst. 36, 3827–3834 (2017).

[5]   Hosseini, N., Kornilov, V.N., Teerling, O.J., Lopez Arteaga, I., de Goey, L.P.H.: Investigating the effects of a heat exchanger on the thermoacoustics in a Rijke tube. In: COMBURA16. , Soesterberg, the Netherlands (2016).

[6]   Hosseini, N., Teerling, O.J., Kornilov, V.N., Lopez Arteaga, I., de Goey, L.P.H.: Thermoacoustic instabilities in a Rijke tube with heating and cooling elements. In: Proceedings of the European Combustion Meeting (2017).

[7]   Surendran, A., Heckl, M.A., Hosseini, N., Teerling, O.J.: Use of heat exchanger for passive control of combustion instabilities. In: ICSV 2016 - 23rd International Congress on Sound and Vibration: From Ancient to Modern Acoustics. pp. 1–8. , Athens, Greece, Greece (2016).

[8]   Strobio Chen, L., Hosseini, N., Polifke, W., Teerling, O.J., Lopez Arteaga, I., de Goey, L.P.H.: Acoustic scattering behavior of a 2D flame with heat exchanger in cross-flow. In: ICSV 2016 - 23rd International Congress on Sound and Vibration: From Ancient to Modern Acoustics. pp. 1–8. , Athens, Greece (2016).

[9]   Lighthill, M.J.: The Response of Laminar Skin Friction and Heat Transfer to Fluctuations in the Stream Velocity. Proc. R. Soc. A Math. Phys. Eng. Sci. 224, 1–23 (1954).

[10]   Witte, A., Polifke, W.: Modeling Heat Transfer and Skin Friction Frequency Response of a Cylinder in Pulsating Cross-Flow - a Unifying Perspective. In: 12th International Conference on Heat Transfer, Fluid Mechanics and Thermodynamics (2016).

[11]   Durox, D., Schuller, T., Candel, S.: Self-induced Instability of a Premixed Jet Flame Impinging on a Plate. Proc. Combust. Inst. 29, 69–75 (2002).

[12]   Schuller, T., Durox, D., Candel, S.: Dynamics of and Noise Radiated by a Perturbed Impinging Premixed Jet Flame. Combust. Flame. 128, 88–110 (2002).

[13]   Fernandes, E.C., Leandro, R.E.: Modeling and Experimental Validation of Unsteady Impinging Flames. Combust. Flame. 146, 674–686 (2006).

[14]   Li, Y.: Thermoacoustic Refrigerators: Experiments and Scaling Analysis, (2011).

[15]   Shahi, M., Kok, J.B.W., Roman Casado, J.C., Pozarlik, A.K.: Study of Unsteady Heat Transfer as a Key Parameter to Characterize Limit Cycle of High Amplitude Pressure Oscillations. In: Volume 5C: Heat Transfer. p. V05CT18A011. ASME (2014).

[16]   Namdar, A., Kianifar, A., Roohi, E.: Numerical Investigation of Thermoacoustic Refrigerator at Weak and Large Amplitudes Considering Cooling Effect. Cryogenics (Guildf). 67, 36–44 (2015).

[17]   Witte, A., Polifke, W.: Dynamics of unsteady heat transfer in pulsating flow across a cylinder. Int. J. Heat Mass Transf. 109, 1111–1131 (2017).

[18]   Kedia, K.S., Ghoniem, A.F.: An analytical model for the prediction of the dynamic response of premixed flames stabilized on a heat-conducting perforated plate. Proc. Combust. Inst. 34, 921–928 (2013).

[19]   Schlimpert, S., Meinke, M., Schröder, W.: Nonlinear analysis of an acoustically excited laminar premixed flame. Combust. Flame. 163, 337–357 (2016).

[20]   Albayrak, A., Blumenthal, R.S., Ulhaq, A., Polifke, W.: An analytical model for the impulse response of laminar premixed flames to equivalence ratio perturbations. Proc. Combust. Inst. 36, 3725–3732 (2017).

[21]   Barrère, M., Williams, F.A.: Comparison of combustion instabilities found in various types of combustion chambers. Symp. Combust. 12, 169–181 (1969).

[22]   Lieuwen, T.C.: Unsteady Combustor Physics. Cambridge University Press, Cambridge (2012).

[23]   Kornilov, V.N., Manohar, M., de Goey, L.P.H.: Thermo-acoustic behaviour of multiple flame burner decks: Transfer Function (de)composition. Proc. Combust. Inst. 32, 1383–1390 (2009).

[24]   Kornilov, V.N., Rook, R., ten Thije Boonkkamp, J., de Goey, L.P.H.: Experimental and Numerical Investigation of the Acoustic Response of Multi-slit Bunsen Burners. Combust. Flame. 156, 1957–1970 (2009).

[25]   Feldman, K.T.: Review of the literature on Rijke thermoacoustic phenomena. J. Sound Vib. 7, 83–89 (1968).

[26]   Emmert, T., Bomberg, S., Jaensch, S., Polifke, W.: Acoustic and intrinsic thermoacoustic modes of a premixed combustor. Proc. Combust. Inst. 36, 3835–3842 (2017).

[27]   Hosseini, N., Kornilov, V.N., Lopez Arteaga, I., Polifke, W., Teerling, O.J., de Goey, L.P.H.: Intrinsic thermoacoustic modes and their interplay with acoustic modes in a Rijke burner. Int. J. Spray Combust. Dyn. 0, (2018).

[28]   Higgins, B.: On the sound produced by a current of hydrogen gas passing through a tube. J. Nat. Philos. Chem. Arts. 1, 129 (1802).

[29]   Strutt, J.W., Rayleigh, B.: The theory of sound - volume 2. Macmillan and Co. Ltd. (1896).

[30]   Putnam, A.A., Dennis, W.R.: A study of burner oscillations of the organ-pipe type. Trans. ASME. 75, 15–28 (1953).

[31]   Dowling, A.P.: The calculation of thermoacoustic oscillations. J. Sound Vib. 180, 557–581 (1995).

[32]   Noiray, N., Durox, D., Schuller, T., Candel, S.: Self-Induced Instabilities of Laminar Premixed Flames Anchored on Perforated Plates. In: Proceedings of the European Combustion Meeting (2005).

[33]   Li, J., Morgans, A.S.: Simplified models for the thermodynamic properties along a combustor and their effect on thermoacoustic instability prediction. Fuel. 184, 735–748 (2016).

[34]   Sattelmayer, T., Polifke, W.: Assessment of methods for the computation of the linear stability of combustors. Combust. Sci. Technol. 175, 453–476 (2003).

[35]   Hosseini, N., Kornilov, V.N., Teerling, O.J., Lopez Arteaga, I., De Goey, L.P.H.: Transfer function calculations of segregated elements in a simplified slit burner with heat exchanger. In: 22nd International Congress on Sound and Vibration, ICSV 2015 (2015).

[36]   Jaensch, S., Emmert, T., Silva, C.F., Polifke, W.: A Grey-Box Identification Approach for Thermoacoustic Network Models. In: Volume 4B: Combustion, Fuels and Emissions. p. V04BT04A051. ASME (2014).

[37]   Munjal, M.L.: Acoustics of Ducts and Mufflers. John Wiley & Sons (1987).

[38]   Hirschberg, A., Rienstra, S.W.: An Introduction to Aeroacoustics. Eindhoven University of Technology (2004).

[39]   Rienstra, S.W., Hirschberg, A.: An Introduction to Acoustics. Eindhoven University of Technology (2015).

[40]   Polifke, W., van der Hoek, J., Verhaar, B.: Everything you always wanted to know about f and g . (1997).

[41]   Hoeijmakers, P.G.M.: Flame-acoustic coupling in combustion instabilities, (2014).

[42]   COMSOL Multiphysics® v. 5.2. www.comsol.com. COMSOL AB, Stockholm, Sweden.

[43]   Kornilov, V.N.: Experimental Research of Acoustically Perturbed Bunsen Flames, (2006).

[44]   Kashinath, K., Hemchandra, S., Juniper, M.P.: Nonlinear Thermoacoustics of Ducted Premixed Flames: The Influence of Perturbation Convection Speed. Combust. Flame. 160, 2856–2865 (2013).

[45]   Li, J., Morgans, A.S.: Time domain simulations of nonlinear thermoacoustic behaviour in a simple combustor using a wave-based approach. J. Sound Vib. 346, 345–360 (2015).

[46]   Walsh, K.T., Long, M.B., Tanoff, M.A., Smooke, M.D.: Experimental and computational study of CH, CH*, and OH* in an axisymmetric laminar diffusion flame. Symp. Combust. 27, 615–623 (1998).

[47]   Panoutsos, C.S., Hardalupas, Y., Taylor, A.M.K.P.: Numerical evaluation of equivalence ratio measurement using OH* and CH* chemiluminescence in premixed and non-premixed methane-air flames. Combust. Flame. 156, 273–291 (2009).

[48]   Henriques, A.M.: Chemiluminescense for flame control. (2011).

[49]   Jebali Jerbi, F., Huelsz, G., Kouidri, S.: Acoustic velocity measurements in resonators of thermoacoustic systems using hot-wire anemometry. Flow Meas. Instrum. 32, 41–50 (2013).

[50]   Mejia, D., Selle, L., Bazile, R., Poinsot, T.: Wall-temperature effects on flame response to acoustic oscillations. Proc. Combust. Inst. 35, 3201–3208 (2015).

[51]   Kedia, K.S., Ghoniem, A.F.: The response of a harmonically forced premixed flame stabilized on a heat-conducting bluff-body. Proc. Combust. Inst. 35, 1065–1072 (2015).

[52]   Miguel-Brebion, M., Mejia, D., Xavier, P., Duchaine, F., Bedat, B., Selle, L., Poinsot, T.: Joint experimental and numerical study of the influence of flame holder temperature on the stabilization of a laminar methane flame on a cylinder. Combust. Flame. 172, 153–161 (2016).

[53]   ANSYS Inc.: ANSYS Fluent Theory Guide. ANSYS Inc. (2013).

[54]   Duchaine, F., Boudy, F., Durox, D., Poinsot, T.: Sensitivity analysis of transfer functions of laminar flames. Combust. Flame. 158, 2384–2394 (2011).

[55]   Huber, A., Polifke, W.: Dynamics of practical premixed flames, part II: identification and interpretation of CFD data. Int. J. Spray Combust. Dyn. 1, 229–249 (2009).

[56] de Lange, R.: Modelling of Premixed Laminar Flames, (1992).

[57] Dyakov, I. V., Konnov, A.A., de Ruyck, J., Bosschaart, K.J., Brock, E.C.M., de Goey, L.P.H.: Measurement of Adiabatic Burning Velocity in Methane-Oxygen-Nitrogen Mixtures. Combust. Sci. Technol. 172, 81–96 (2001).

[58] Ratna Kishore, V., Duhan, N., Ravi, M.R., Ray, A.: Measurement of Adiabatic Burning Velocity in Natural Gas-like Mixtures. Exp. Therm. Fluid Sci. 33, 10–16 (2008).

[59] Sharma, S.P., Agrawal, D.D., Gupta, C.P.: The pressure and temperature dependence of burning velocity in a spherical combustion bomb. Symp. Combust. 18, 493–501 (1981).

[60] Brown, M.J., Lawn, C.J.: Dependence of the Laminar Burning Velocity of Methane , Propane and Ethylene on Initial Temperature and Inert Diluent Concentration. In: Proceedings of the European Combustion Meeting. pp. 1–6 (2003).

[61] Smith, G.P., Golden, D.M., Frenklach, M., Moriarty, N.W., Eiteneer, B., Goldenberg, M., Bowman, C.T., Hanson, R.K., Song, S., Gardiner, William C., J., Lissianski, V. V., Qin, Z.: GRI3, http://www.me.berkeley.edu/gri_mech.

[62] Kazakov, A., Frenklach, M.: DRM19, http://www.me.berkeley.edu/drm.

[63] Kornilov, V.N., Schreel, K.R.A.M., de Goey, L.P.H.: Experimental Transfer Function of Acoustically Perturbed Bunsen-type Flame. In: Proceedings of the European Combustion Meeting (2005).

[64] Emmert, T., Meindl, M., Jaensch, S., Polifke, W.: Linear State Space Interconnect Modeling of Acoustic Systems. Acta Acust. united with Acust. 102, 824–833 (2016).

[65] Technical University of Munich: taX - ThermoAcoustic Network Code, https://tax.wiki.tum.de.

[66] Campa, G., Camporeale, S.M.: Influence of Flame and Burner Transfer Matrix on Thermoacoustic Combustion Instability Modes and Frequencies. In: Volume 2: Combustion, Fuels and Emissions, Parts A and B. pp. 907–918. ASME (2010).

[67] Nicoud, F., Benoit, L., Sensiau, C., Poinsot, T.: Acoustic Modes in Combustors with Complex Impedances and Multidimensional Active Flames. AIAA J. 45, 426–441 (2007).

[68] Teerling, O.J., Hoeijmakers, P.G.M.: Thermo-acoustic modelling in a boiler using FEM. In: COMBURA15 (2015).

[69] Hoeijmakers, P.G.M.: Thermoacoustic modelling using COMSOL. (2010).

[70] Blackshear, P.L.: Driving standing waves by heat addition. Symp. Combust. 4, 553–566 (1953).

[71] Crocco, L.: Aspects of Combustion Stability in Liquid Propellant Rocket Motors Part I: Fundamentals. Low Frequency Instability With Monopropellants. J. Am. Rocket Soc. 21, 163–178 (1951).

[72] Merk, H.J.: An analysis of unstable combustion of premixed gases. Symp. Combust. 6, 500–512 (1957).

[73] Boyer, L., Quinard, J.: On the Dynamics of Anchored Flames. Combust. Flame. 82, 51–65 (1990).

[74] Baillot, F., Durox, D., Prud'homme, R.: Experimental and theoretical study of a premixed vibrating flame. Combust. Flame. 88, 149–168 (1992).

[75] Baillot, F., Bourehla, A., Durox, D.: The characteristics method and cusped flame fronts. Combust. Sci. Technol. 112, 327–350 (1996).

[76] Fleifil, M., Annaswamy, A.M., Ghoneim, Z.A., Ghoniem, A.F.: Response of a Laminar Premixed Flame to Flow Oscillations : A Kinematic Model and Thermoacoustic Instability Results. Combust. Flame. 106, 487–510 (1996).

[77] Ducruix, S., Durox, D., Candel, S.: Theoretical and experimental determinations of the transfer function of a laminar premixed flame. Proc. Combust. Inst. 28, 765–773 (2000).

[78] Schuller, T., Durox, D., Candel, S.: A unified model for the prediction of laminar flame transfer functions. Combust. Flame. 134, 21–34 (2003).

[79] Karimi, N., Brear, M.J., Jin, S.H., Monty, J.P.: Linear and non-linear forced response of a conical, ducted, laminar premixed flame. Combust. Flame. 156, 2201–2212 (2009).

[80] Hong, S., Shanbhogue, S.J., Kedia, K.S., Ghoniem, A.F.: Impact of the Flame-Holder Heat-Transfer Characteristics on the Onset of Combustion Instability. Combust. Sci. Technol. 185, 1541–1567 (2013).

[81] Mehta, P., Soteriou, M., Banaszuk, A.: Impact of exothermicity on steady and linearized response of a premixed ducted flame. Combust. Flame. 141, 392–405 (2005).

[82] Gaudron, R., Gatti, M., Mirat, C., Schuller, T.: Impact of the injector size on the transfer functions of premixed laminar conical flames. Combust. Flame. 179, 138–153 (2017).

[83] Schlimpert, S., Hemchandra, S., Meinke, M., Schröder, W.: Hydrodynamic instability and shear layer effect on the response of an acoustically excited laminar premixed flame. Combust. Flame. 162, 345–367 (2015).

[84] Matsui, Y.: An experimental study on pyro-acoustic amplification of premixed laminar flames. Combust. Flame. 43, 199–209 (1981).

[85]   Sugimoto, T., Matsui, Y.: An experimental study on the dynamic behavior of premixed laminar flames. Symp. Combust. 19, 245–250 (1982).

[86]   Preetham, Santosh, H., Lieuwen, T.C.: Dynamics of Laminar Premixed Flames Forced by Harmonic Velocity Disturbances. J. Propuls. Power. 24, 1390–1402 (2008).

[87]   Schreel, K.R.A.M., Rook, R., de Goey, L.P.H.: The acoustic response of burner-stabilized premixed flat flames. Proc. Combust. Inst. 29, 115–122 (2002).

[88]   Rook, R., de Goey, L.P.H., Somers, L.M.T., Schreel, K.R.A.M., Parchen, R.: Response of burner-stabilized flat flames to acoustic perturbations. Combust. Theory Model. 6, 223–242 (2002).

[89]   Rook, R., de Goey, L.P.H.: The acoustic response of burner-stabilized flat flames: a two-dimensional numerical analysis. Combust. Flame. 133, 119–132 (2003).

[90]   Schreel, K.R.A.M., van den Tillaart, E.L., de Goey, L.P.H.: The influence of burner material properties on the acoustical transfer function of radiant surface burners. Proc. Combust. Inst. 30 II, 1741–1748 (2005).

[91]   Volkov, E.N., Kornilov, V.N., de Goey, L.P.H.: Experimental evaluation of DC electric field effect on the thermoacoustic behaviour of flat premixed flames. Proc. Combust. Inst. 34, 955–962 (2013).

[92]   Vroemen, W.F.C., Kornilov, V.N., de Goey, L.P.H.: Thermo-acoustic Transfer Function of Flames Embedded in Porous Media. In: Proceedings of the European Combustion Meeting (2013).

[93]   van den Tillaart, E.L., Schreel, K.R.A.M., de Goey, L.P.H.: Observables for the Response of Laminar Flames to Acoustic Disturbances. In: Proceedings of the European Combustion Meeting (2005).

[94]   Schreel, K.R.A.M., van den Tillaart, E.L., Janssen, R.W.M., de Goey, L.P.H.: The effect of heat transfer on acoustics in burner stabilized flat flames. In: Proceedings of the European Combustion Meeting (2003).

[95]   de Goey, L.P.H., van Oijen, J.A., Kornilov, V.N., ten Thije Boonkkamp, J.: Propagation, dynamics and control of laminar premixed flames. Proc. Combust. Inst. 33, 863–886 (2011).

[96]   Altay, H.M., Park, S., Wu, D., Wee, D., Annaswamy, A.M., Ghoniem, A.F.: Modeling the dynamic response of a laminar perforated-plate stabilized flame. Proc. Combust. Inst. 32 I, 1359–1366 (2009).

[97]   Kedia, K.S., Altay, H.M., Ghoniem, A.F.: Impact of flame-wall interaction on premixed flame dynamics and transfer function characteristics. Proc. Combust. Inst. 33, 1113–1120 (2011).

[98]   Gaudron, R., Gatti, M., Mirat, C., Schuller, T.: Analysis of the Transfer Function of Large and Small Premixed Laminar Conical Flames. In: Proceedings of ASME Turbo Expo (2017).

[99]   Yu, J.F., Yu, R., Bai, X.S., Bastiaans, R.J.M., van Oijen, J.A., de Goey, L.P.H.: Numerical study of heat transfer and flame stabilization of laminar premixed flames anchored to a heat-flux burner. In: Proceedings of the European Combustion Meeting (2013).

[100]   Silva, C.F., Emmert, T., Jaensch, S., Polifke, W.: Numerical study on intrinsic thermoacoustic instability of a laminar premixed flame. Combust. Flame. 162, 3370–3378 (2015).

[101]   Lieuwen, T.C.: Modeling Premixed Combustion-Acoustic Wave Interactions: A Review. J. Propuls. Power. 19, 765–781 (2003).

[102]   Kedia, K.S., Ghoniem, A.F.: Mechanisms of stabilization and blowoff of a premixed flame downstream of a heat-conducting perforated plate. Combust. Flame. 159, 1055–1069 (2012).

[103]   Sogaro, F., Schmid, P., Morgans, A.S.: Sensitivity analysis of thermoacoustic instabilties. In: 24th International Congress on Sound and Vibration (2017).

[104]   Hoeijmakers, P.G.M., Kornilov, V.N., Lopez Arteaga, I., de Goey, L.P.H., Nijmeijer, H.: Flame dominated thermoacoustic instabilities in a system with high acoustic losses. Combust. Flame. 169, 209–215 (2016).

[105]   Kabiraj, L., Saurabh, A., Steinart, R., Paschereit, C.O.: Instabilities in a Confined Flat-flame System. In: Proceedings of the European Combustion Meeting (2013).

[106]   Wikipedia: Tempering, https://en.wikipedia.org/wiki/Tempering_(metallurgy).

[107]   Bergman, T.L., Lavine, A.S., Incropera, F.P., DeWitt, D.P.: Fundamentals of Heat and Mass Transfer. John Wiley & Sons (2011).

[108]   Baehr, H.D., Stephan, K.: Heat and Mass Transfer. Springer (2011).

[109]   Föller, S., Selimefendigil, F., Polifke, W.: The dynamic response of heat transfer of a cylinder in cross flow to velocity fluctuations. J. Fluid Mech. (2013).

[110]   Russo, G.P.: Hot Wire Anemometer. In: Aerodynamic Measurements: From Physical Principles to Turnkey Instrumentation. pp. 67–98 (2011).

[111]   Davis, M.R.: Hot Wire Anemometer Response in a Flow with Acoustic Disturbances. J. Sound Vib. 56, 565–570 (1978).

[112]   Davies, T.W.: Modelling the Response of a Hot-wire anemometer. Appl. Math. Model. 10, 256–261 (1986).

[113]   Zink, F., Vipperman, J., Schaefer, L.: CFD simulation of a thermoacoustic engine with coiled resonator. Int. Commun. Heat Mass Transf. 37, 226–229 (2010).

[114]   Holzinger, T., Emmert, T., Polifke, W.: Optimizing thermoacoustic regenerators for maximum amplification

of acoustic power. J. Acoust. Soc. Am. 136, 2432–2440 (2014).

[115] Swift, G.W.: Thermoacoustic engines and refrigerators: a short course. In: Joint 137th Meeting of Acoustical Societies of America and Europe (1999).

[116] Li, S., Li, Q., Tang, L., Yang, B., Fu, J., Clarke, C.A., Jin, X., Ji, C.Z., Zhao, H.: Theoretical and experimental demonstration of minimizing self-excited thermoacoustic oscillations by applying anti-sound technique. Appl. Energy. 181, 399–407 (2016).

[117] Matveev, K.I.: Thermoacoustic Instabilities in the Rijke Tube: Experiments and Modeling. Thesis. 2003, (2003).

[118] Heckl, M.A.: Active control of the noise from a rijke tube. J. Sound Vib. 124, 117–133 (1988).

[119] Sayadi, T., Le Chenadec, V., Schmid, P., Richecœur, F., Massot, M.: Time-domain analysis of thermo-acoustic instabilities in a ducted flame. Proc. Combust. Inst. 35, 1079–1086 (2014).

[120] Xu, J., Li, W., Zhao, D., Liu, Y.: Numerical Simulation for Thermoacoustic Phenomena in Rijke Tube - Analysis for Self-oscillation and the Limit Period. In: International Conference on Future Electrical Power and Energy Systems. pp. 7–12 (2012).

[121] Kamsanam, W., Mao, X., Jaworski, A.J.: Development of Experimental Techniques for Measurement of Heat Transfer Rates in Heat Exchangers in Oscillatory Flows. Exp. Therm. Fluid Sci. 62, 202–215 (2015).

[122] Konstantinidis, E., Castiglia, D., Balabani, S.: An Experimental Study of Steady and Pulsating Cross-flow Over a Semi-staggered Tube Bundle. J. Mech. Eng. Sci. 219, 283–298 (2005).

[123] Costa, S.C., Barreno, I., Tutar, M., Esnaola, J. a., Barrutia, H.: The Thermal Non-equilibrium Porous Media Modelling for CFD Study of Woven Wire Matrix of a Stirling Regenerator. Energy Convers. Manag. 89, 473–483 (2015).

[124] Skaria, M., Abdul Rasheed, K.K., Shafi, K. a., Kasthurirengan, S., Behera, U.: Simulation Studies on the Performance of Thermoacoustic Prime Movers and Refrigerator. Comput. Fluids. 111, 127–136 (2015).

[125] Hosseini, N., Kornilov, V.N., Teerling, O.J., Lopez Arteaga, I., de Goey, L.P.H.: Evaluating thermoacoustic properties of heating appliances considering the burner and heat exchanger as acoustically active elements. Combust. Flame. 191, (2018).

[126] Surendran, A., Heckl, M.A., Hosseini, N., Teerling, O.J.: Passive control of instabilities in combustion systems with heat exchanger. Int. J. Spray Combust. Dyn. 0, 1756827717773148 (2017).

[127] Strobio Chen, L., Armin, W., Wolfgang, P.: Thermo-Acoustic Characterization of a Heat Ex- Changer in Cross Flow Using Compressible and Weakly Compressible Numerical Simulation. In: International Congress on Sound and Vibration. pp. 12–16 (2015).

[128] Rayleigh, L.: The Explanation of Certain Acoustical Phenomena. Nature. 18, 319–321 (1878).

[129] Mugridge, B.D.: Combustion Driven Oscillations. J. Sound Vib. 70, 437–452 (1980).

[130] Polifke, W., Poncet, A., Paschereit, C.O., Döbbeling, K.: Reconstruction of Acoustic Transfer Matrices By Instationary Computational Fluid Dynamics. J. Sound Vib. 245, 483–510 (2001).

[131] Rook, R.: Acoustics in Burner-Stabilised Flames, (2001).

[132] Freitag, E.: On the Measurement and Modelling of Flame Transfer Functions at Elevated Pressure, (2009).

[133] Bomberg, S., Emmert, T., Polifke, W.: Thermal versus acoustic response of velocity sensitive premixed flames. Proc. Combust. Inst. 35, 3185–3192 (2015).

[134] Kornilov, V.N., de Goey, L.P.H.: Combustion thermo-acoustics in context of activity and stability criteria for linear two-ports. In: Proceedings of the European Combustion Meeting (2017).

[135] Hosseini, N., Kornilov, V.N., Teerling, O.J., Lopez Arteaga, I., de Goey, L.P.H.: Development of a numerical model for obtaining flame transfer function in a simplified slit burner with heat exchanger. In: The 21st International Congress on Sound and Vibration (2014).

[136] Polifke, W., Paschereit, C.O., Klaus, D.: Constructive and Destructive Interference of Acoustic and Entropy Waves in a Premixed Combustor with a Choked Exit. Int. J. Acoust. Vib. 6, 135–146 (2001).

[137] Heravi, H.M., Azarinfar, A., Kwon, S.I., Bowen, P.J., Syred, N.: Determination of Laminar Flame thickness and Burning Velocity of Methane-air Mixtures. In: Proceedings of the European Combustion Meeting (2007).

[138] de Goey, L.P.H., Somers, L.M.T., Bosch, W.M.M.L., Mallens, R.M.M.: Modeling of the Small Scale Structure of Flat Burner-Stabilized Flames. Combust. Sci. Technol. 104, 387–400 (1995).

[139] Polifke, W., Gentemann, A.: Order and realisability of impulse response filters for accurate identification of acoustical multi-ports from transient CFD. Int. J. Acoust. Vib. 9, 139–148 (2004).

[140] Hoeijmakers, P.G.M., Lopez Arteaga, I., Kornilov, V.N., Nijmeijer, H., de Goey, L.P.H.: Experimental investigation of intrinsic flame stability. In: Proceedings of the European Combustion Meeting (2013).

[141] Emmert, T., Bomberg, S., Polifke, W.: Intrinsic thermoacoustic instability of premixed flames. Combust. Flame. 162, 75–85 (2015).

[142] Courtine, E., Selle, L., Poinsot, T.: DNS of Intrinsic Thermoacoustic modes in laminar premixed flames. Combust. Flame. 162, 1–11 (2015).

[143] Hoeijmakers, P.G.M., Kornilov, V.N., Lopez Arteaga, I., de Goey, L.P.H., Nijmeijer, H.: Intrinsic instability of flame-acoustic coupling. Combust. Flame. 161, 2860–2867 (2014).

[144] Silva, C.F., Merk, M., Komarek, T., Polifke, W.: The contribution of intrinsic thermoacoustic feedback to combustion noise and resonances of a confined turbulent premixed flame. Combust. Flame. 182, 269–278 (2017).

[145] Albayrak, A., Steinbacher, T., Komarek, T., Polifke, W.: Convective Scaling of Intrinsic Thermo-Acoustic Eigenfrequencies of a Premixed Swirl Combustor. J. Eng. Gas Turbines Power. 140, 041510 (2017).

[146] Powell, A.: On the Edgetone. J. Acoust. Soc. Am. 33, 395–409 (1961).

[147] Ségoufin, C., Fabre, B., de Lacombe, L.: Experimental investigation of the flue channel geometry influence on edge-tone oscillations. Acta Acust. united with Acust. 90, 966–975 (2004).

[148] Fabre, B., Hirschberg, a.: Physical Modeling of Flue Instruments: A Review of Lumped Models. Acta Acust. united with Acust. 86, 12 (2000).

[149] Castellengo, M.: Acoustical analysis of initial transients in flute like instruments. Acta Acust. united with Acust. 85, 387–400 (1999).

[150] Chu, B.-T.: On the generation of pressure waves at a plane flame front. Symp. Combust. 4, 603–612 (1953).

[151] Raun, R.L., Beckstead, M.W., Finlinson, J.C., Brooks, K.P.: A review of Rijke tubes, Rijke burners and related devices. Prog. Energy Combust. Sci. 19, 313–364 (1993).

[152] Laera, D., Campa, G., Camporeale, S.M.: A finite element method for a weakly nonlinear dynamic analysis and bifurcation tracking of thermo-acoustic instability in longitudinal and annular combustors. Appl. Energy. 187, 216–227 (2017).

[153] Weng, F., Zhu, M., Jing, L.: Beat: a nonlinear thermoacoustic instability in Rijke burners. Int. J. Spray Combust. Dyn. 6, 247–266 (2014).

[154] Cintra, B.F.C., Fernandes, E.C.: Thermoacoustic instabilities of lean disc flames. Fuel. 184, 973–986 (2016).

[155] Selimefendigil, F., Föller, S., Polifke, W.: Nonlinear Identification of Unsteady Heat Transfer of a Cylinder in Pulsating Cross Flow. Comput. Fluids. 53, 1–14 (2012).

[156] Chen, S., Zhao, D., Li, H.K.H., Ng, T.Y., Jin, X.: Numerical study of dynamic response of a jet diffusion flame to standing waves in a longitudinal tube. Appl. Therm. Eng. 112, 1070–1082 (2017).

[157] Zalluhoglu, U., Olgac, N.: Passive suppression of thermoacoustic instability in a Rijke tube. IFAC-PapersOnLine. 49, 59–64 (2016).

[158] Zhao, D., Ji, C.Z., Li, X., Li, S.H.: Mitigation of premixed flame-sustained thermoacoustic oscillations using an electrical heater. Int. J. Heat Mass Transf. 86, 309–318 (2015).

[159] Hoeijmakers, P.G.M., Kornilov, V.N., Lopez Arteaga, I., Nijmeijer, H., de Goey, L.P.H.: Effect of Burner Partitioning on System Thermo-acoustics. In: 18th International Congress on Sound and Vibration (2011).

[160] Yang, X., Turan, A., Lei, S.: Thermoacoustic Instability in a Rijke Tube with a Distributed Heat Source. J. Thermodyn. 2015, (2015).

[161] Li, L., Zhao, D., de Goey, L.P.H.: Transient energy growth analysis of a thermoacoustic system with distributed mean heat input. Int. J. Heat Mass Transf. 102, 287–301 (2016).

[162] Kim, K.T., Lee, J.G., Quay, B.D., Santavicca, D.A.: Spatially distributed flame transfer functions for predicting combustion dynamics in lean premixed gas turbine combustors. Combust. Flame. 157, 1718–1730 (2010).

Summary

Thermoacoustic Instabilities in Heating Appliances with Premixed Burner and Heat Exchanger

Thermoacoustic instabilities are frequently present in lean (partially) premixed combustion systems and have been studied for more than a century. They may occur in various systems, such as gas turbines, boilers and other heating systems. Mitigating or preventing these instabilities is currently a challenge in the heating industry, specifically for systems with lean premixed burners. Many of such systems include not only burners, but also heat exchangers. The heat exchanger is designed to create a reverse temperature jump of the same order of magnitude as the burner. Acoustic waves alter the heat absorption of the heat exchanger, thus the heat exchanger is an additional acoustic element next to the burner in the acoustic network. In addition, the practical need to make compact heating appliances and reduce nitrogen oxides, leads to small distances between the burner and heat exchanger. Consequently, mutual interactions between them may occur that alter their individual and combined thermoacoustic properties. This motivates a detailed investigation about the combined thermoacoustic behavior of the burner and heat exchanger in heating appliances.

In this thesis, the thermoacoustic instabilities are investigated in heating appliances with both premixed burner and heat exchanger as active acoustic elements. Particularly, the aim is to answer the following questions:

- What are the separate thermoacoustic responses of practical laminar premixed burners and heat exchangers in heating appliances?
- How do the burner and heat exchanger come together to define the thermoacoustic characteristics of a heating appliance?
- What kind of interactions are envisioned between the burner and heat exchanger that may affect the thermoacoustic behavior of the complete system?
- What are the physical phenomena and governing parameters responsible for these interactions?
- Is it possible to decouple the effects of the burner and heat exchanger? If so, how can one decouple these effects and use them to design more stable heating appliances?

To approach the formulated problems and questions, various configurations of the burner and heat exchanger are studied. Measurements of the velocity-sensitive flame transfer function are performed on burner decks featuring multiple Bunsen-type laminar flames, in order to setup a reliable base for flame transfer function validations. Then separate 2D CFD simulations of simplified, but representative, burners and heat exchangers are performed and the transfer function and transfer matrix approaches are used to identify the thermoacoustic behavior of the elements.

Detailed 3D CFD simulations are also performed for better understanding of the in-depth flame processes. Then, by changing the distance between the burner and heat exchanger, their mutual interactions are studied from hydrodynamic and thermoacoustic point of view and solutions are proposed to decouple their thermoacoustic effects. An acoustic network model is used to study the stability of the system as a 1D linear acoustic network, and a Helmholtz solver is used for cases that are more realistic, such as distributed heat exchanger configurations.

The results of the measurements and CFD simulations reveal details about how the laminar flame transfer function can be affected by the flame shape and stabilization, and the heat exchanger transfer function by the geometry and flow velocity. It is also shown that the presence of the heat exchanger considerably affects the thermoacoustic properties of the total system. However, it is possible to decouple the heat exchanger from the burner when the distance between them is large enough such that the flame does not impinge on the heat exchanger surface. This can be done by registering the flow velocity on an interface plane between the two elements. If flame impingement occurs, the response of the system changes drastically and may enhance the thermoacoustic instabilities. A large parameter sweep provides a broad picture of the system modes and reveals new information on the intrinsic thermoacoustic modes of the system. Moreover, the interactions of the intrinsic and acoustic modes are investigated in detail.

The results for the realistic configurations demonstrate how thermoacoustic instabilities may occur in domestic heating appliances and how the design of the heat exchanger can affect these instabilities. By studying the simplified and realistic configurations, the following general conclusions are formulated regarding the thermoacoustic behavior of the burner and heat exchanger, as well as their interactions:

- Both the burner and heat exchanger are thermoacoustically active
- Combined thermoacoustic behavior of the burner and heat exchanger is crucial to system stability
- Next to the burner, the design of the heat exchanger also considerably affects the system stability
- The full picture of system stability also requires considering the interplays between acoustic and ITA modes.

Acknowledgments

I need to thank many people who have helped me throughout my journey. First, I would like to thank my advisors at TU/e, *Philip de Goey*, *Ines Lopez Arteaga* and *Viktor Kornilov*. I have been extremely lucky to have your guidance along the way. *Philip*, you have always been there to help me in every aspect despite that you were the busiest person I have ever met! *Ines*, you were always positive and so encouraging that I am sure I could not have finished this thesis without your support. *Viktor*, your critical thinking and immense overview of our research subject paved the way for me and I was blessed to have your support all the way until the end. Thank you all very much.

Next, I want to thank my advisor at Bekaert Combustion Technology, *Joán Teerling*. *Joán*, I am honored to spend most of my PhD time next to you and in your team. You were my first manager in the Netherlands and I have learned so much from you that has partly shaped my career. Thank you for believing in me and being my mentor.

I would also like to thank all my former colleagues at Bekaert Combustion Technology who supported me in every way they could and made me feel completely at home in the Netherlands. I will miss our discussions that helped me see my work from various angles, our lunch talks about movies, R&D day activities and much more. There are so many names that I cannot count, but I am grateful to all of you for making the beginning of my career in the Netherlands so memorable. A special thank you to my former colleague and now friend, *Camillo Hogenbirk* for generously offering your help in every way you could. Specifically for teaching me how to cut down trees and illustrating how (not) to cut myself…! I will keep counting on your friendship *Camillo*.

I have been specifically lucky because I was part of a large team of peers and scientists, the *TANGO* project network. The unique opportunity of working with you towards a common goal has been so enjoyable and fruitful that I will never forget. The quality time that we have spent together during our gatherings, workshops and conferences has created a network of friendship that will last long. I hope to meet you every now and then to catch up. A special thank you to *Maria Heckl* for coordinating TANGO project and dedicating yourself to every single one of us. Thank you for handling everything professionally and providing the most positive and calm atmosphere for your researchers to do their job. I wish you even more success in your next project. I am also grateful to *Wolfgang Polifke* and *Lin Strobio Chen* for being my amazing hosts during my secondment at TU München. You not only helped me learn many new things and insights in our field of research, but also made my time in Munich a very memorable one. Thank you.

When I look back to my educational past, I see that I have never been alone. The dedication and support of my teachers and professors has been crucial in my success. Your faces and names are carved in every small and big turn in my journey towards where I am now. I thank every single one of you for selflessly providing me with your knowledge in many aspects.

As far as looking to the past goes, there has always been the love and dedication of my guardian angels, my parents *Parviz* and *Tooba*. I literally owe my life to you two. I do not, and guess never

will, find the words to describe how grateful I am to have you always by my side. I just hope I get the chance to prove to you that I was worth it. I love you both internally. I am also thankful to my parents-in-law, *Mahnaz* and *Iraj*, who were as supportive as my own parents. *Mahnaz*, although you are not among us anymore, but I have felt and do feel your presence with us.

Last but by no means least, is someone who caused the biggest and most amazing turning point of my life, the love of my life, *Mana. Mana*, you are the reason I believe that true love exists. You know, better than anyone else does, that you constitute a large part of who I am today. You also know that my whole PhD was never possible without your motivation and support before, during and after in every single step. I do not know what I have done to deserve you, but I do look forward to stepping further in life with you and I know that I won't be lost when you are with me. Thank

you *Mana* for being you… دوستت دارم مانا، عشق من

List of Publications

Journal articles

2018 *Thermoacoustic properties of heating appliances with the flame and heat exchanger as acoustically active elements*
N. Hosseini, V. Kornilov, O.J. Teerling, I. Lopez Arteaga, L.P.H. de Goey
Combustion and Flame, Vol. 191, pp. 486-495 (2018)

Intrinsic thermoacoustic modes and their interplay with acoustic modes in a Rijke burner
N. Hosseini, V. Kornilov, I. Lopez Arteaga, W. Polifke, O.J. Teerling, L.P.H. de Goey
International Journal of Spray and Combustion Dynamics, doi.org/10.1177/1756827718782884 (2018)

2017 *Passive control of instabilities in combustion systems with heat exchanger*
A. Surendran, M.A. Heckl, N. Hosseini, O.J. Teerling
International Journal of Spray and Combustion Dynamics, doi.org/10.1177/1756827717731486 (2017)

Conference proceedings peer-reviewed

2017 *Thermoacoustic instabilities in a Rijke tube with heating and cooling elements*
N. Hosseini, O.J. Teerling, V. Kornilov, I. Lopez Arteaga, L.P.H. de Goey
8th European Combustion Meeting 2017, 18-21 April 2017, Dubrovnik, Croatia

2016 *Acoustic scattering behavior of a 2D flame with heat exchanger in cross-flow*
L. Strobio Chen, N. Hosseini, W. Polifke, O.J. Teerling, V. Kornilov, I. Lopez Arteaga, L.P.H. de Goey
23rd International Congress on Sound and Vibration, 10-14 July 2016, Athens, Greece

2015 *Transfer function calculations of segregated elements in a simplified slit burner with heat exchanger*
N. Hosseini, V. Kornilov, O.J. Teerling, I. Lopez Arteaga, L.P.H. de Goey
22nd International Congress on Sound and Vibration, 12-16 July 2015, Florence, Italy

Development of a numerical model for obtaining flame transfer function in a simplified slit burner with heat exchanger
N. Hosseini, V. Kornilov, O.J. Teerling, I. Lopez Arteaga, L.P.H. de Goey
21st International Congress on Sound and Vibration, 13-17 July 2015, Beijing, China

Curriculum Vitae

Naseh Hosseini was born on April 11, 1986 in Mashhad, Iran.

Sep. 2004 – Sep. 2009   **BSc**
Ferdowsi University of Mashhad, Mashhad, Iran
Mechanical Engineering, Solid Mechanics Design
Simulation and performance evaluation of air-cooled condenser axial-flow fans using computational fluid dynamics

Sep. 2009 – Feb. 2012   **MSc**
Azad University of Mashhad, Mashhad, Iran
Mechanical Engineering, Energy Conversion
NO_x reduction using SNCR in a liquid fuel burner

Sep. 2010 – Jul. 2012   **Consultant CFD Engineer**
Saman Sanat Sepehr, Mashhad, Iran
CFD simulations of complex fluid flow in various turbomachinery

Aug. 2013 – Jan. 2019   **PhD**
Eindhoven University of Technology, Eindhoven, the Netherlands
Mechanical Engineering, Multiphase and Reactive Flows
This dissertation

Nov. 2013 – Sep. 2017   **R&D Researcher Thermoacoustics**
Bekaert Combustion Technology B.V., Assen, the Netherlands
Partner in TANGO project

Sep. 2017 – present   **Thermal Analyst**
ASML, Veldhoven, the Netherlands
In charge of thermal architecture and performance of modules in semiconductor manufacturing machines

The installation and photo used for the cover is created by Daniel Palacios at an exhibition organized at the National Art Museum of China as part of the cultural program of the 2008 Olympic Games in Beijing.

The installation reacts to those who watch it. When the audience moves around it, they influence the movements of the rope, generating visual and acoustic sound waves from harmonic to more complex patterns. According to the number of observers and their movements, it passes from a steady line with no sound to chaotic shapes of irregular sounds through different phases of harmonic waves; examining the action-reaction principle applied to sound and space, thus a perfect example of a live feedback loop.

For more info visit
https://danielpalacios.info/waves

9 789038 646473